Summer 8-1-2023

Combining Semi-Continuous and Discrete Water Quality Data to Characterize Solute Transport, Biogeochemical Processes, and Wildfire Disturbances in Fluvial Systems

Justin Rae Nichols
University of New Mexico

Justin Rae Nichols

Candidate

Department of Civil, Construction & Environmental Engineering

Department

This thesis is approved, and it is acceptable in quality and form for publication:

Approved by the Thesis Committee:

Dr. Ricardo González-Pinzón, Chairperson

Dr. David Van Horn

Dr. José M. Cerrato

Dr. Laura J. Crossey

COMBINING SEMI-CONTINUOUS AND DISCRETE WATER QUALITY DATA TO CHARACTERIZE SOLUTE TRANSPORT, BIOGEOCHEMICAL PROCESSES, AND WILDFIRE DISTURBANCES IN FLUVIAL SYSTEMS

by

JUSTIN RAE NICHOLS

B.S. Civil Engineering, University of New Mexico, 2018
M.S Civil Engineering, University of New Mexico, 2020

DISSERTATION

Submitted in Partial Fulfillment of the
Requirements for the Degree of

Doctor of Philosophy
Engineering

University of New Mexico
Albuquerque, New Mexico

August, 2023

Acknowledgements

I want to thank my parents, Kathy and Gary Nichols, who are my foundation, and their support has been instrumental to my past and future success. I would also like to thank both of my granddads, Richard Nichols and James Field, who, through their tireless work, dedication, and guidance, have inspired me to question the unknown and work to unravel the mysteries of the universe. Of course, I would not be writing my dissertation if it was not for the professors and staff at the University of New Mexico, especially for the exceptional faculty at the Department of Civil, Construction, and Environmental Engineering. Also, my team members at the Center of Water and Environment have played a critical role toward my degree completion. They have spent countless hours helping me with field research and were my support network.

There have been countless professors who have contributed considerably to my success, but some that I would like to recognize by name are Steve Peralta, who was my guide into Civil Engineering, Dr. Bruce Thompson, and Dr. Mark Stone, who guided me in my early years of my undergraduate program, Dr. Jose Cerrato who was my guide into environmental research, and Dr. Dave Van Horne, who I credit to my knowledge in field research. Lastly, I want to thank Dr. Ricardo Gonzalez-Pinzon, my advisor and a knowledgeable mentor I respect immensely. Dr. Ricardo Gonzalez-Pinzon saw my potential, believed in me, and pushed me beyond what I thought I was capable of, and in times of uncertainty, he was always there to assure me that while the path to novel insight may be difficult, it is well worth the endeavor as new discovery pushes us beyond the status quo.

“Often, the wisest person in the room is the quietest person in the room. The key to knowledge and understanding is to listen.” - Richard Nichols

Combining Semi-Continuous and Discrete Water Quality Data to Characterize Solute Transport, Biogeochemical Processes, and Wildfire Disturbances in Fluvial Systems

By

Justin Nichols

B.S. Civil Engineering, 2018

M.S. Civil Engineering, 2020

Ph.D. Civil Engineering, 2023

ABSTRACT

In the past decade, high-frequency water quality sondes have become more abundant in watersheds across North America and Europe and are gaining a foothold in Asia and South America. In this dissertation, three relevant topics associated with high-frequency data are investigated, i.e., the impact of winter's precipitation on surface water quality and stream metabolism, the longitudinal propagation of wildfire disturbances through a fluvial network, and the use of machine learning with high-frequency data to estimate fluvial nutrient processing. First, we found that significant snow precipitation can cause surface water anoxia and declines in stream metabolism. Second, our data illustrate that fluvial water quality and metabolic activity degradation can propagate hundreds of kilometers downstream from a wildfire. Lastly, our work demonstrates that recurrent neural networks can outperform traditional regression methods when using atmospheric parameters to estimate nitrate uptake.

Table of Contents

List of Figures

Chapter 2:

List of Tables

Chapter 2

Chapter 3

Chapter 4

Chapter 1: General Introduction

1.1 Context

In the "hydrological renaissance", a term coined in Eos 100 (Gabrielle, 2019), there is an unprecedented access to high-frequency water quality data from semi-continuous sensors, making hydrological research, watershed management, and risk assessments much more data-based than ever before (Kirchner et al., 2004; Pellerin et al., 2016; Rode et al., 2016; Rundel et al., 2009). For example, the implementation of water quality sondes in fluvial systems has led to advances in our understanding of ecosystem control points, i.e., moments or areas within a system that experience elevated and disproportional biochemical processing (Bernhardt et al., 2018; Krause et al., 2017; McClain et al., 2003; Zhao et al., 2021). Similarly, sondes have been recently used for the quantification of nutrient, organic matter, and suspended sediment dynamics in response to atmospheric forcing, land-use change, or anthropogenic disturbances. Sondes are instrumental due to their ability to capture multiple temporal scales, from diel cycles to seasonal trends, while observing non-linear and cascading interactions by sampling an array of parameters. Due to their inherent benefit to hydrologists, the United States Geological Survey (USGS) has rapidly expanded its high-frequency water quality network with 2430 water quality sonde sites in operation across CONUS as of 2023.

One relatively unexplored application of high-frequency sensors is the linkage of atmospheric forcing, terrestrial processes, and the response of aquatic ecosystems to their dynamics (Perdrial et al., 2014; Turcotte et al., 2017). By disproportionality performing research during summer months and focusing on in-stream functioning alone, stream restoration, watershed management, and contaminant remediation has unintentionally

overemphasized the physical restoration of streams and disincentivized restoration efforts that focus on terrestrial ecosystems and nonstationary atmospheric forcing (Palmer, et al., 2014). The urgency for high-frequency multivariate water quality studies during the winter months is further exacerbated by the projected reduction of snowpack within the alpine watersheds of the American Southwest and other parts of the world, which will lead to alterations to terrestrial ecosystems, stream biota, water budgets, and environmental services (Elias et al., 2021).

The increase in air temperatures from anthropogenically driven climate change is not only changing the snowpack within alpine watersheds, but it is leading to an increase in wildfire frequency and severity (Reidmiller et al., 2017; Running, 2006). It is widely known that wildfires have direct impacts on hydrological processes and fluvial water quality. Wildfires cause reductions in infiltration and transpiration, resulting in an increase in surface runoff, erosion and elevated organic loads, changes in biological and chemical oxygen demand that may cause anoxic conditions, and an increase in suspended sediments along entire fluvial systems (Carr et al., 2012; Robinne et al., 2020; Sherson et al., 2015). Water quality sondes have been a vital method for quantifying wildfire disturbances at the watershed (Ball et al., 2021; Sherson et al., 2015). However, most wildfire research involving water quality sondes has been opportunistic. Therefore, there are gaps in our understanding of the spatial extent of the propagation of wildfire disturbances along fluvial networks. With wildfire frequency and burn areas forecasted to increase, it is imperative to further our understanding and predictive capabilities to better constrain models and help decrease their uncertainty. An improved understanding of how

aquatic processes are affected by wildfire disturbances can help decision makers determine best practices to mitigate impacts to their water sources.

While water quality sondes and multi-parameter datasets are becoming more ubiquitous in some countries (Rode et al., 2016), there are still a vast array of parameters and metrics that cannot be measured at high-frequency in-situ due to epistemic, logistical, or technological constraints. Quantities such as the concentrations of emerging contaminants, heavy metal, solute transport processes, reaction rates, and stable isotope ratios often require discrete sampling methods and laboratory analysis, which culminates into temporally limited sampling frequency. Machine learning algorithms (MLA) present a novel opportunity to utilize high-frequency data from in-situ sensors as non-linear proxies to lower frequency discrete sample data, enabling higher frequency estimates of the latter and opening new ways to explore the coupling of atmospheric, terrestrial, aquatic, and human systems at scales relevant to watershed managing (Fan et al., 2020; Kirchner et al., 2004; Raghavendra & Deka, 2014; Shen, 2018; Xu & Liang, 2021). However, with the vast array of high-frequency parameters and MLA architectures available, there remains significant uncertainty on which architectures and parameters are needed to generate a robust methodology that relates high to low-frequency datasets while limiting information loss or requiring extensive domain knowledge. By minimizing uncertainty on parameter and architecture selection, we could then start to make inferences about subsampled parameters or relevant metrics, using datasets with higher observational frequencies.

1.2 Objectives

This dissertation aims to address three research objectives using high-frequency data from water quality sondes and meteorological stations:

Objective 1: Analyze how changes to winter precipitation patterns alters water quality and stream metabolism within an alpine watershed.

Objective 2: Quantify longitudinal water quality and stream functioning degradation from catastrophic wildfires.

Objective 3: Develop a machine learning framework to estimate the dynamics of nutrient uptake rates from high-frequency atmospheric and water quality parameters.

1.3 Summary of Findings

This dissertation is the result of the compilation of three manuscripts that are (or will be) published in peer-reviewed journals.

Chapter 2, *The Understudied Winter: Evidence of how precipitation differences affect stream metabolism in a headwater* investigates how changes in winter precipitation affects water quality and stream metabolism in an alpine watershed in New Mexico. The research was conducted during a snow-abundant El Niño winter and snow-drought La Niña winter, and utilized high-frequency water quality sondes in conjunction with collocated meteorological stations that enabled the quantification of atmospheric forcing. We found that besides snow precipitation, atmospheric forcing was not significantly different between winters; however, during the El Niño winter, dissolved oxygen experienced prolonged anoxia and a sudden halt in diel cycling. Also, during the El Niño winter, there were increases in fluorescent dissolved organic matter, pH, and specific

conductivity, while stream metabolism became metabolically inactive. In contrast, during the La Niña year, dissolved oxygen never reached anoxia, and its diel cycling increased in magnitude during the winter months. Also, stream metabolism remained relatively steady with slight, short-lived changes to its metabolic rate. Our research demonstrates the significant role of winter precipitation on fluvial water quality and stream metabolism, and reinforces the need for further research in winter hydrology as winter precipitation is projected to decline.

Chapter 3, *Longitudinal propagation of aquatic disturbances from the largest wildfire recorded in New Mexico* studies water quality impact and degradation to stream metabolism across multiple stream orders in the Gallinas Creek-Pecos River-Santa Rosa Lake fluvial network during and after the Hermit's Peak-Calf Canyon fire. Our results show that monitoring sites upstream of Santa Rosa Lake experienced significant increases in fluorescent dissolved organic matter and turbidity, concurrently with the high precipitation monsoon season. Our findings suggest that stream reaches within the burn scar experienced substantial scouring of the benthic zone, while reaches further from the burn scar experience reduced scouring of the benthic zone but elevated organic, nutrient, and suspended sediment fluxes. Lastly, our results demonstrate that Santa Rosa Lake buffered wildfire disturbances by attenuating water quality degradations and mitigating metabolic alterations experienced for up to180 km upstream of it.

Lastly, Chapter 4, *Bridging the gap in the data revolution: Leveraging artificial intelligence to estimate nitrate uptake in fluvial systems*, explores the use of high-frequency water quality and meteorological data with machine learning to estimate nitrate

uptake rate dynamics within a fluvial system. Over two years, nutrient addition experiments were performed at two stream reaches of contrasting biotic and abiotic factors to quantify nitrate uptake rate at a three-week interval. Water quality sondes and meteorological stations were collocated at the nutrient addition sites, which quantified ambient water quality conditions and atmospheric forcing. Due to the high logistical and financial burden of performing a nutrient addition experiments, this research aimed at using machine learning algorithms of varying complexity to estimate nitrate uptake rates from high-frequency datasets, potentially reducing the costs and logistics of characterizing quantities that are not available at high-resolution. Our results show that a recurrent neural network with the highest model variance outperformed all other algorithms when utilizing meteorological data as model predictors. However, it performed the worst when water quality data was incorporated as predictors. When utilizing water quality predictors, algorithms with lower variance and higher bias had the best predictive performance. With the increase in spatial resolution of high-frequency meteorological data, our research demonstrates that recurrent neural networks can be used in conjunction with meteorological data to estimate nitrate uptake rate in fluvial systems across CONUS. However, while high-frequency meteorological data is becoming more ubiquitous, a national database of nutrient experiments that encompasses a wide array of varying stream reach heterogeneity is needed to scale effectively.

References:

Ball, G., Regier, P., González-Pinzón, R., Reale, J., & Van Horn, D. (2021). Wildfires increasingly impact western US fluvial networks. Nature Communications, 12(1), Article 1. https://doi.org/10.1038/s41467-021-22747-3

Bernhardt, E. S., Heffernan, J. B., Grimm, N. B., Stanley, E. H., Harvey, J. W., Arroita, M., Appling, A. P., Cohen, M. J., McDowell, W. H., Hall, R. O., Read, J. S., Roberts, B. J., Stets, E. G., & Yackulic, C. B. (2018). The metabolic regimes of flowing waters. Limnology and Oceanography, 63(S1), Article S1. https://doi.org/10.1002/lno.10726

Carr, J., White, A. B., & Thomson, B. (2012). Large-Scale Forest Fires and Resulting Alterations to the Hydrologic Cycle in the Western U.S. AGU Fall Meeting Abstracts, 2012, EP51E-06.

Elias, E., James, D., Heimel, S., Steele, C., Steltzer, H., & Dott, C. (2021). Implications of observed changes in high mountain snow water storage, snowmelt timing and melt window. Journal of Hydrology: Regional Studies, 35, 100799. https://doi.org/10.1016/j.ejrh.2021.100799

Fan, H., Jiang, M., Xu, L., Zhu, H., Cheng, J., & Jiang, J. (2020). Comparison of long short term memory networks and the hydrological model in runoff simulation. Water, 12(1), 175.

Kirchner, J. W., Feng, X., Neal, C., & Robson, A. J. (2004). The fine structure of water-quality dynamics: The(high-frequency) wave of the future. Hydrological Processes, 18(7), 1353–1359. https://doi.org/10.1002/hyp.5537

Krause, S., Lewandowski, J., Grimm, N., Hannah, D., Pinas., G., (2017). Ecohydrological interface as hot spots of ecosystem processes. Water Resources Research, 53, 8

McClain, M. E., Boyer, E. W., Dent, C. L., Gergel, S. E., Grimm, N. B., Groffman, P. M., Hart, S. C., Harvey, J. W., Johnston, C. A., Mayorga, E., McDowell, W. H., & Pinay, G. (2003). Biogeochemical Hot Spots and Hot Moments at the Interface of Terrestrial and Aquatic Ecosystems. Ecosystems, 6(4), 301–312. https://doi.org/10.1007/s10021-003-0161-9

Palmer, M. A., Hondula, K. L., & Koch, B. J. (2014). Ecological Restoration of Streams and Rivers: Shifting Strategies and Shifting Goals. Annual Review of Ecology, Evolution, and Systematics, 45(1), 247–269. https://doi.org/10.1146/annurev-ecolsys-120213-091935

Perdrial, J. N., McIntosh, J., Harpold, A., Brooks, P. D., Zapata-Rios, X., Ray, J., Meixner, T., Kanduc, T., Litvak, M., Troch, P. A., & Chorover, J. (2014). Stream water carbon controls in seasonally snow-covered mountain catchments: Impact of inter-annual variability of water fluxes, catchment aspect and seasonal processes. Biogeochemistry, 118(1–3), 273–290. https://doi.org/10.1007/s10533-013-9929-y

Pellerin, B. A., Stauffer, B. A., Young, D. A., Sullivan, D. J., Bricker, S. B., Walbridge, M. R., Clyde Jr, G. A., & Shaw, D. M. (2016). Emerging tools for continuous nutrient monitoring networks: Sensors advancing science and water resources protection. JAWRA Journal of the American Water Resources Association, 52(4), 993–1008.

Raghavendra. N, S., & Deka, P. C. (2014). Support vector machine applications in the field of hydrology: A review. Applied Soft Computing, 19, 372–386. https://doi.org/10.1016/j.asoc.2014.02.002

Reidmiller, D. R., Avery, C. W., Easterling, D. R., Kunkel, K. E., Lewis, K. L. M., Maycock, T. K., & Stewart, B. C. (2018). Impacts, Risks, and Adaptation in the United States: The Fourth National Climate Assessment, Volume II. U.S. Global Change Research Program. https://doi.org/10.7930/NCA4.2018

Robinne, F.-N., Hallema, D. W., Bladon, K. D., & Buttle, J. M. (2020). Wildfire impacts on hydrologic ecosystem services in North American high-latitude forests: A scoping review. Journal of Hydrology, 581, 124360. https://doi.org/10.1016/j.jhydrol.2019.124360

Rode, M., Wade, A. J., Cohen, M. J., Hensley, R. T., Bowes, M. J., Kirchner, J. W., Arhonditsis, G. B., Jordan, P., Kronvang, B., Halliday, S. J., Skeffington, R. A., Rozemeijer, J. C., Aubert, A. H., Rinke, K., & Jomaa, S. (2016). Sensors in the Stream: The High-Frequency Wave of the Present. Environmental Science & Technology, 50(19), 10297–10307. https://doi.org/10.1021/acs.est.6b02155

Rundel, P., Graham, E., Allen, M., Fisher, J., Harmon, T., (2009). Environmental sensor networks in ecological research. New Phyotogist, 182, 3, 589-607

Running, S. W. (2006). Is Global Warming Causing More, Larger Wildfires? Science, 313(5789), 927–928. https://doi.org/10.1126/science.1130370

Shen, C. (2018). A transdisciplinary review of deep learning research and its relevance for water resources scientists. Water Resources Research, 54(11), 8558–8593.

Sherson, L. R., Van Horn, D. J., Gomez-Velez, J. D., Crossey, L. J., & Dahm, C. N. (2015). Nutrient dynamics in an alpine headwater stream: Use of continuous water quality sensors to examine responses to wildfire and precipitation events: CONTINUOUS RESPONSES TO WILDFIRE AND PRECIPITATION

EVENTS. Hydrological Processes, 29(14), 3193–3207. https://doi.org/10.1002/hyp.10426

Turcotte, B., Alfredsen, K., Beltaos, S., & Burrell, B. C. (2017). Ice-Related Floods and Flood Delineation along Streams and Small Rivers. 26.

Vincent Gabrielle. (2019). The Renaissance of Hydrology. Eos, 100.

Xu, T., & Liang, F. (2021). Machine learning for hydrologic sciences: An introductory overview. WIREs Water. https://doi.org/10.1002/wat2.1533

Zhao, S., Zhang, B., Sun, X., & Yang, L. (2021). Hot spots and hot moments of nitrogen removal from hyporheic and riparian zones: A review. Science of The Total Environment, 762, 144168. https://doi.org/10.1016/j.scitotenv.2020.144168

Chapter 2: The Understudied Winter: Evidence of How Precipitation Differences Affect Stream Metabolism in a Headwater

Justin Nichols[1], Aashish Sanjay Khandelwal[1], Peter Regier[1,2], Betsy Summers[1], David J. Van Horn[3], Ricardo González-Pinzón[1]

[1]Department of Civil, Construction and Environmental Engineering, University of New Mexico, Albuquerque, New Mexico, USA, [2]Marine and Coastal Research Laboratory, Pacific Northwest National Laboratory, Sequim, Washington, USA, [3]Department of Biology, University of New Mexico, Albuquerque, New Mexico, USA

Corresponding authors: Justin Nichols justin67@unm.edu and Ricardo González-Pinzón gonzaric@unm.edu

Published in: Frontiers in Water

DOI: 10.3389/frwa.2022.1003159

2.1. Introduction

Climate warming in the US has been most pronounced during the winter, resulting in shortening of the snow season, a reduction in snow pack, and shifts in the timing and volume of snowmelt related runoff (Climate Central, 2022; Elias et al., 2021; Godsey et al., 2014; Grimm et al., 2013). The reduction in snowpack volume has been linked to increasing winter temperatures resulting in more frequent winter melt events (Musselman et al., 2021), shifts in precipitation from snow to rain (Berghuijs et al., 2014), and lower total precipitation trends interwoven with climate patterns including El Niño and La Niña (Cortés & Margulis, 2017; Goddard & Gershunov, 2020). These changes in winter precipitation patterns affect in-stream freeze–thaw cycles, including ice and snow cover, and have the potential to trigger direct and indirect effects on in-stream physical, chemical, and biological processes (Prowse, 2001; Prowse et al., 2006) in ~60% of river basins in the Northern Hemisphere (Allard et al., 2011).

While winter freeze-thaw cycles can trigger changes in pH, conductivity, dissolved oxygen and redox conditions, nutrient inputs, groundwater and surface-water interactions, and flood plain connectivity (Schreier, 1980; Prowse, 2001), a recent review by Tolonen et al. (2019) noted that since winter is the most understudied season in ecohydrology, we do not currently understand the short-to-long term ecological effects of ice and snow formation in streams. Considering stream metabolism as a proxy for ecological functioning (Bernhardt et al., 2018; Summers et al., 2020), based on fundamental principles we can expect that in-stream ice and snow cover during the winter could block the light that phototrophic communities need to grow, affecting primary production and autotrophy (Frenette et al., 2008), and triggering cascading effects on

local food webs. Similarly, ice and snow cover can disrupt atmosphere-water interactions, halting in-stream reaeration (Fang & Stefan, 2009; Price et al., 1995; Woods, 1992). When combined, in-stream aerobic respiration and the lack of oxygen availability from primary production and reaeration should gradually result in increasingly anoxic conditions, similar to what has been documented in lentic systems (Davis et al., 2020; Jansen et al., 2021). These seasonal changes, thus, could alter redox conditions and the overall ecological functioning of the stream by switching the main electron acceptor (i.e., from oxygen to nitrate to manganese, etc.) and the species that could thrive under such transient conditions.

While fundamental principles suggest ice and snow cover likely shift stream metabolism and ecological functioning, little field data exists to verify these hypotheses and to determine when, for how long, and how frequently ice and snow cover control metabolism in streams that experience freeze-thaw cycles. Addressing these unknowns offers an opportunity to better understand and quantify the ecological relevance of freezing streams and winters, which are intuitively associated with ecological "cold-spots" and "cold-moments", i.e., lower than average ecological activity in space and time, but may regulate the timing and availability of key resources needed for metabolism and nutrient cycling. Thus, tackling the lack of research on winter metabolism in streams is timely because warming trends in high latitudes and altitudes indicate that freezing streams may become less abundant and frequent.

The specific objectives of this study were to 1) determine interannual variability in physical, geochemical, and biological signals in a montane stream during contrasting winters, and 2) explore the implications of these findings in the context of climate change

on stream function. To meet these objectives, we used high-resolution, multi-parameter data collected in a headwater stream in New Mexico and its local environment (climate and soil) to link changes in winter precipitation regimes to changes in aerobic stream metabolism, a key indicator of stream functioning. We found that sustained winter anoxia and dormant aerobic stream metabolism were driven by ice and snow cover during the El Niño year (higher precipitation), and that even though freezing occurred at the top of the stream during the La Niña year (reduced precipitation), it did not cause winter anoxia and instead elevated winter aerobic metabolism. We also found that spring metabolism is highly dependent on winter precipitation. Our results suggest that a progressive decrease in winter snowpacks and the reduction of ice and snow cover on freezing streams may result in the loss of hot moments for anaerobic metabolism, which has the potential to alter food webs and ecological functioning, not only during the winter but before and after fully anoxic conditions are established.

2.2 Methods

2.2.1 Site Description

Our study site is in the East Fork Jemez River (EFJR), within the Valles Caldera National Preserve, New Mexico (Figure 2.1). The EFJR watershed is small, high-altitude catchment, with a drainage area of 107 km^2 at an elevation range between 2,580 to 3,432 m. The EFJR is a 3rd order stream with a mean annual discharge of 0.06-0.09 m^3/s, featuring large flow fluctuations during spring snowmelt and summer monsoon storms of up to 3 m^3/s. The average channel slope at the study site is 0.057 m/m and the sinuosity is 2.04, making it a low gradient meandering stream. The sediments in the streambed are

mostly organic matter, silt, and pebbles, and the average stream bank height is 0.8 m. The riparian vegetation of the EFJR consists of non-woody grass with limited canopy cover with an average growing season between March and November, and the stream fluctuates between autotrophic and heterotrophic conditions, but is net autotrophic, averaging 0.3 $gO_2\ m^{-2}\ d^{-1}$ (Summers et al., 2020). The EFJR watershed is contained within a volcanic caldera and the vegetation is composed of extensive grasslands in the valley floors and evergreen forest biomes at higher elevations (48 and 52% of the land cover, respectively). The EFJR watershed experiences large seasonal climate variability with average monthly precipitation and air temperatures ranging between 3.1-10.6 cm and 4.1-15.9 ºC, as reported in Model my Watershed (Stroud Water Research Center, 2021).

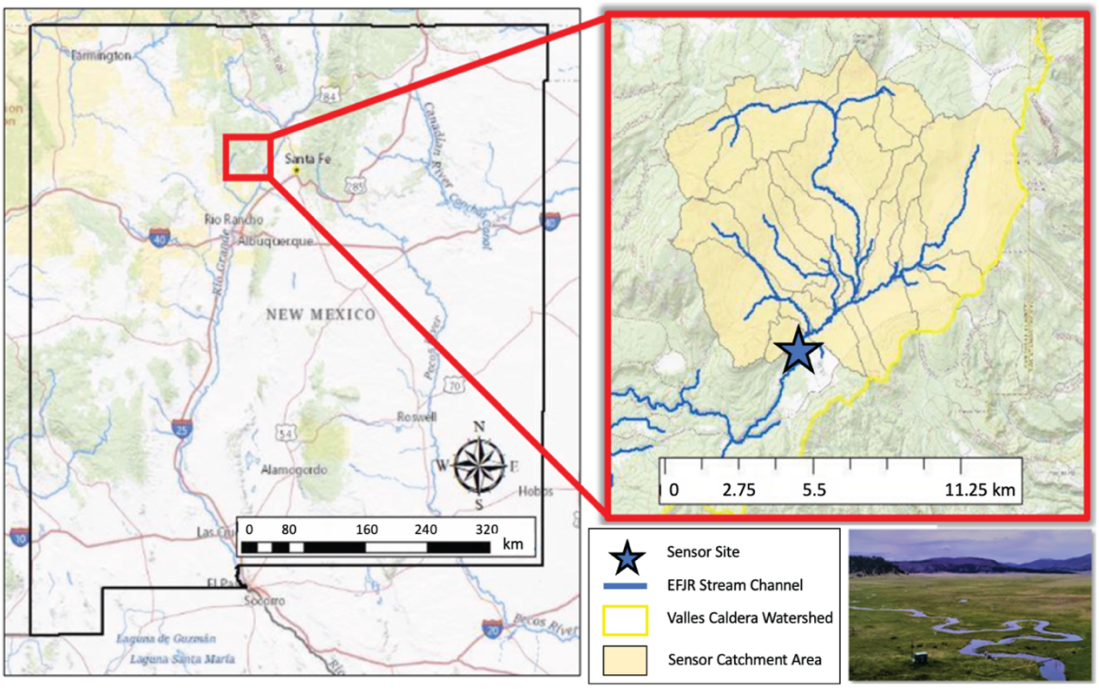

Figure 2.1: Map and picture of the East Fork Jemez River watershed, located in the Valles Caldera National Preserve in north central New Mexico (USA).

2.2.2 Sensor Deployment and Processing of Raw Data

We collected sensor and meteorological data in the EFJR during the winter of 2018-2019, a weak to moderate El Niño year, and 2020-2021, a moderate La Niña year.

Sensors used: We deployed a YSI EXO2 multiparameter water quality sonde and a HOBO U20 pressure logger ~10 cm above the streambed of the EFJR (Yellow Springs Instruments, n.d.). The EXO2 measured water temperature, specific conductivity, DO, fluorescent dissolved organic matter (fDOM), turbidity, and pH at 15-min intervals. The HOBO was set to log synchronously with the YSI EXO2 (Yellow Springs Instruments, n.d.). Meteorological data were collected 30 m away from the in-stream sensors at a climate station maintained by the Western Regional Climate Center (Western Regional Climate Center, 2021), which monitored air temperature, solar radiation, snow depth, barometric pressure, and soil temperature (20 cm depth) at 10-min intervals. All in-stream sensors were cleaned and recalibrated every three weeks in accordance with USGS guidelines (Wagner et al., 2006). We equipped the study site with a solar panel, batteries, and a Campbell Scientific CR1000 datalogger to power the semi-continuous water quality sensors. During field visits, we also collected secondary DO measurements during ice- and snow-cover conditions using a YSI ProODO to validate the YSI EXO2 records. Table 2.1 summarizes continuous parameters collected.

Table 2.1: Parameters and corresponding sensors and sampling frequencies available in our study.

Instrument	Parameter	Abbreviation	Units	Sampling Frequency (min)
HOBO U20	Stage	Stage	m	15
YSI EXO2	Dissolved oxygen	DO	ppm	15
	Specific conductivity	Sp Cond	uS cm^{-1}	15
	Water temperature	Water Temp	ºC	15
	Turbidity	Turbidity	FNU	15
	pH	pH	-	15
	Fluorescent dissolved organic matter	fDOM	RFU	15
WRCC metrological station	Air temperature	Air Temp	ºC	10
	Soil temperature	Soil Temp	ºC	10
	Barometric pressure	Baro Press	mmHg	10
	Snow depth	Snow depth	mm	10
	Photosynthetically Active Radiation	PAR	µmol m^{-2} s^{-1}	10
	Precipitation	Precip	mm	10

Raw data analysis: fDOM was corrected by water temperature changes following (Watras et al., 2011):

$$\mathrm{fDOM_{temp}} = \frac{\mathrm{fDOM}}{1 + \rho(\mathrm{W_T} - \mathrm{T_l})} \quad (1),$$

where $\mathrm{fDOM_{temp}}$ is the temperature corrected fDOM concentration (RFU), where fDOM is the uncorrected fDOM concentration (RFU), ρ is temperature-specific fluorescence coefficient of $-7.545 \times 10^{-3}\ °\mathrm{C}^{-1}$ determined experimentally using EFJR water, $\mathrm{W_T}$ is the water temperature (°C), and $\mathrm{T_l}$ is the lab temperature of 22 °C when fDOM was calibrated. We present fDOM in RFU instead of quinine sulfate units (QSU) because QSU measurements exceeded the maximum detection limit from March 22nd to April 30th, 2019.

Total solar radiation was multiplied by a factor of 2.04 to estimate photosynthetically active radiation (PAR, Meek et al., 1984). To replicate conditions within the stream water column during periods of ice- and snow-cover, PAR was set to zero if snow depth was greater than 200 mm and if diel water temperature cycling ceased (Petrov et al., 2005).

Discharge was derived from a rating curve that was developed by relating data collected during field visits with a Sontek FlowTracker and stage data (Equation 1). Due to logistical constraints, discharge measurements were not taken during periods of prolonged ice- and snow-cover. Therefore, we used stage data from a downstream USGS river gage (USGS Gage: 08324000, Jemez River near Jemez, NM) to establish a time-lagged relationship between the two sites and estimate missing discharges (Summers et al., 2020) (Equation 2 and 3):

$$Q = 0.0343 * \exp^{2.683*\text{Stage}} \quad (2),$$

$$Q = 0.0343 * \exp^{2.683*(1.385*JR_{\text{stage}_{(t-8h)}} - 1.164)} \quad (3),$$

where Q ($m^3\ s^{-1}$) is the discharge at our study site; Stage (m) is the stage data derived from the HOBO pressure transducers within periods when flow could be measured in the field; and JR_{stage} (m) is the stage data from the Jemez River USGS gage used to estimate Q when flow could not be measured at the study site.

Data processing: Raw and converted data were processed for outliers and sensor drift with Aquarius Workstation 3.3 (Aquatic Informatics, Vancouver, British Columbia). Suspected outliers were eliminated by using a moving average filter targeting points deviating more than 20% from an hourly window (Wagner et al., 2006). We corrected for sensor drift and biofouling by comparing pre- and post-cleaning calibration values and applying a linear correction from the date of the previous maintenance. Linear interpolation was applied to data gaps that were less than 12 hours and an hourly resampling was performed to ensure consistent timestamps for all parameters. A final visual inspection of data quality was performed prior to any statistical analysis.

2.2.3 Stream Metabolism

The cumulative photosynthetic and heterotrophic activity of algal and bacterial communities can be estimated as stream metabolism, an indicator of ecological functioning. We estimated daily averages of stream metabolism using the USGS StreamMetabolizer model, which uses a one-station model based on the open-channel metabolism approach (Equations 4-6), combined with inverse Bayesian modeling of diel DO, to estimate gross primary production (GPP), ecosystem respiration (ER), and

reaeration coefficients (K_{600}) (Appling et al., 2018; Odum, 1956). GPP quantifies DO production from phototrophic communities, ER quantifies DO losses due to autotrophic and heterotrophic respiration, and K_{600} is a standardized oxygen gas exchange rate coefficient between the water column and the atmosphere. The modeling equations used in Stream Metabolizer are:

$$\frac{dDO_t}{dt} = \frac{1}{Z_t}\left(\frac{GPP(t_1 - t_0) * PPFD_t}{\int_{u=t_0}^{t_1} PPFD_u du} + ER\right) + \frac{K_{600}(DO_{sat,t} - DO_{mod,t})}{\sqrt{\frac{S_A - S_B T_t + S_C T_t^2 + S_D T_t^3}{600}}} \quad (4),$$

$$DO_{mod,t} = DO_{mod,t-\Delta t} + \int_{u=t-\Delta t}^{t} \left(\frac{dDO_{mod,u}}{du} + \varepsilon_{proc,u}\right) du \quad (5),$$

$$DO_{obs,t} = DO_{mod,t} + \varepsilon_{obs,t} \quad (6),$$

where DO_t is the observed dissolved oxygen (mg L^{-1}) at time t; $DO_{sat,t}$ is the hypothetical saturated dissolved oxygen concentration (mg L^{-1}); $DO_{mod,t}$ is the modeled dissolved oxygen concentration (mg L^{-1}); ε_{obs} and ε_{proc} are the observation and processes errors; t_0 and t_1 are the beginning and end of the day (d); Z_t is stage (m); $PPFD_t$ is solar radiation as PAR (µmol m^{-2} d^{-1}); T_t is the water temperature (°C); $S_{A,B,C,D}$ are dimensionless Schmidt coefficients (-); GPP is the daily average areal rate of gross primary production ($gO_2\ m^{-2}\ d^{-1}$); ER is the daily average areal rate of ecosystem respiration ($gO_2\ m^{-2}\ d^{-1}$); and K_{600} is the standardized gas exchange rate coefficient (d^{-1}).

Using results from one of our previous studies at the EFJR (Summers et al., 2020), we set the prior probability distribution's mean and standard deviations for GPP (3.9 and 1.5 $gO_2\ m^{-2}\ d^{-1}$, respectively) and ER (3.6 and 1.7 $gO_2\ m^{-2}\ d^{-1}$, respectively). We ran the model for 3000 iterations and 1500 burn-ins with a binned K_{600} bounded by the minimum and maximum discharge. During periods when we observed ice and snow cover over the water column and daily maximum water temperature did not exceed 0.2°C, we constrained $K_{600} = 0$, since reaeration cannot occur under such conditions. We verified the model's fit by validating that it converged to stable solutions and by ensuring that each parameter's Gelman-Rubin R^2 value was less than 1.1. We also checked for possible equifinality between ER and K_{600} by checking any potential covariances between the two parameters (Appling et al., 2018). The covariance between ER and K_{600} estimates was low with a linear correlation coefficient of -0.028 (Figure S2.1).

2.2.4 Statistical Methods and Data Organization

Templates and periods of analysis: We organized the results and discussion into three relevant templates: physical and atmospheric, geochemical, and DO and metabolism. The physical and atmospheric template includes time series of discharge, snow depth, temperatures (air, soil, and water), turbidity and PAR. The geochemical template includes time series of fDOM, specific conductivity, pH and DO. The DO and stream metabolism template includes time series of DO, GPP, ER, and reaeration fluxes. All datasets are also classified by season to further organize the results and discussions. To test statistical differences between seasons, we used two-sample Student's t-test

taking into account autocorrelation, thus reducing type-1 error, by using the equivalent sample size method on data that was aggregated daily mean values to remove seasonality in timeseries and meet autoregressive assumption (O'Shaughnessy & Cavanaugh, 2015). Prior to performing t-test, parameter's seasonal daily mean values were visually inspected for normality using Q-Q plots, and if normality was not met, log transformations were performed for both the El Niño and La Niña season.

Frequency analysis: We generated spectrograms using the *pspectrum* function in Matlab (The Mathworks Inc., Natick, Massachusetts) for all sensor-generated time series. Spectrograms use discrete, short-time Fourier transforms to quantify the significance of sinusoidal signals at multiple frequencies or periodicities within a time series (Kirchner et al., 2000). Since diel cycling often exhibits strong seasonality in water quality data, we extracted the spectral power of our time series at a periodicity of 24-h and categorized them as strong diel cycling (>0 dB), weak diel cycling (0 to -100 dB), and no discernable diel cycling (<-100 dB). Threshold limits for diel cycling classification were determined by using water temperature, a parameter with known shifts in diel cycling, as a benchmark enabling us to relate periods with varying diel cycling with their respective spectral power. We did not include stream metabolism estimates in the spectral analysis because they were comprised of daily averaged measurements and do not hold relevant information regarding diel cycling.

Principal component analysis: We examined the relationships between parameters using a principal component analysis (PCA) conducted in Matlab. The first two principal components were determined sufficient for analysis based on the inflection point of variance percent explained (Figure S2.2). Since the correlation coefficient

between two parameters is equivalent to the cosine angle between their eigenvectors, parameters plotting in the same direction are positively correlated, those in opposite directions are negatively correlated, and those that are orthogonal are uncorrelated (Jolliffe & Cadima, 2016). We calculated 24 h averages for aquatic and meteorological parameters to be able to include daily estimates of stream metabolism, and standardized each parameter's daily average by centering the mean at zero and scaling by a standard deviation of one to make parameters with varying magnitudes and units comparable:

$$S_X = \frac{X - \mu_X}{\sigma_X} \quad (7),$$

where S_X is the standardized parameter X (-), and μ_X and σ_X are the mean and standard deviation of parameter X.

2.3. Results

2.3.1 Physical and Atmospheric Template:

Clear differences in snow accumulation occurred between the 2018-2019 El Niño and 2020-2021 La Niña years, with greater snow accumulation taking place during the former. During the El Niño year, a large winter precipitation event increased snow depth to ~800 mm during early January 2019, and, due to numerous precipitation events, a depth of ~500 mm persisted through the end of the winter (Figures 2.2 and S2.3). In contrast, during the La Niña year, snow depth remained low (~100 mm) throughout the January to March period, with very few precipitation events and several weeks both of ~0 mm and ~200 mm snow depth (Figure 2.2). This between-year difference in winter snow depth was significant and represents an ~77% decrease in mean snow depth from the El Niño to La Niña year (Figure 2.3). Stream discharge (fall and spring), soil temperature

(winter), and turbidity (fall and winter) were also significantly higher during the El Niño year, while PAR (winter) was the only physical parameter that was significantly higher during La Niña year.

2.3.2 Geochemical Template:

Water chemistry parameters varied widely across seasons and between years. fDOM gradually increased during the spring of the El Niño year from winter values of ~20 RFU, reaching sustained peak values of ~50 RFU during mid to late spring (Figure 2.2). In contrast, during the La Niña year, fDOM values remained at ~20 RFU, except for a few short-lived increases to ~40 RFU (Figure 2.2). This between-year difference in spring fDOM was significant (Figure 2.3). Additionally, an absence of a diel fDOM signal was observed during the El Niño year, while a moderate to strong daily cycling signal was present in the La Niña year (Figure 2.4). Specific conductivity was significantly higher in the La Niña year during the spring (Figures 2.2 and 2.3), and during the winter of the El Niño year its diurnal cycling was suppressed (Figure 2.4). Lastly, during the El Niño year, pH initially decreased from fall values of ~7 to early winter values of ~6, before increasing to ~8 by the end of the winter season (Figure 2.2). Minimal diel cycling for pH was observed during the winter season (Figure 2.4). During the La Niña year, pH values remained between 7 and 7.5 for all seasons (Figure 2.2) and moderate diel cycling occurred (Figure 2.4).

2.3.3 DO and Stream Metabolism Template:

DO and stream metabolism values varied significantly among seasons within the El Niño year and between the El Niño and La Niña years. Dissolved oxygen concentrations fell from daily mean values of ~9 mg/L to ~4 mg/L in early January 2019, declining to anoxia (~0 mg/L) in late January 2019, which persisted through the end of February 2019 (Figure 2.2 and S2.3). While declines in DO were also observed during February 2021 in the La Niña year, concentrations rarely decreased below 4 mg/L (Figure 2.2). These between-year differences in winter DO were significant (Figure 2.3). Additionally, diel cycling of DO differed greatly between years during the winter period, with moderate to no cycling occurring during the El Niño year, and moderate to strong cycling occurring during the La Niña year (Figure 2.4).

Both GPP and ER were below 5 g O_2 $m^{-2}d^{-1}$ during the fall of the El Niño year, however, during the winter these values decreased to ~ 0 g O_2 $m^{-2}d^{-1}$from early January to mid-March, before increasing considerably during spring (Figure 2.2). During the La Niña year, GPP was lowest (~3-4 g O_2 $m^{-2}d^{-1}$) during mid-fall, and highest (~5-10 g O_2 $m^{-2}d^{-1}$) during the winter (Figure 2.2). ER followed the same general pattern as GPP during the La Niña year, except for low ER values at the end of December 2020. Both ER and GPP were significantly higher during the spring in the El Niño year, and higher in the fall and winter in the La Niña year (Figure 2.3).

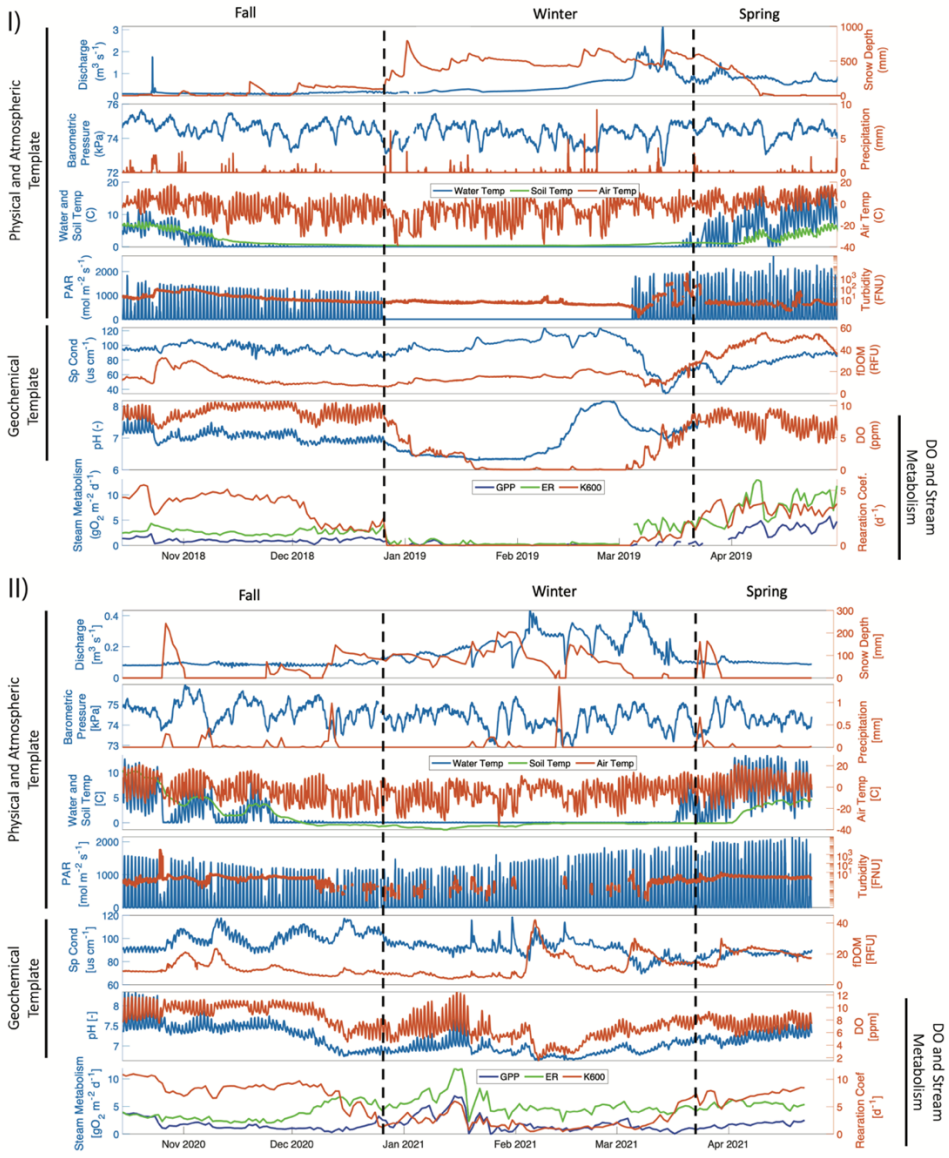

Figure 2.2: Post QA/QC time series from the I) El Niño 2018-2019 and II) La Niña 2020-2021 data organized in three templates: physical and atmospheric, geochemical and DO and stream metabolism. Dashed vertical lines delineate fall, winter, and spring.

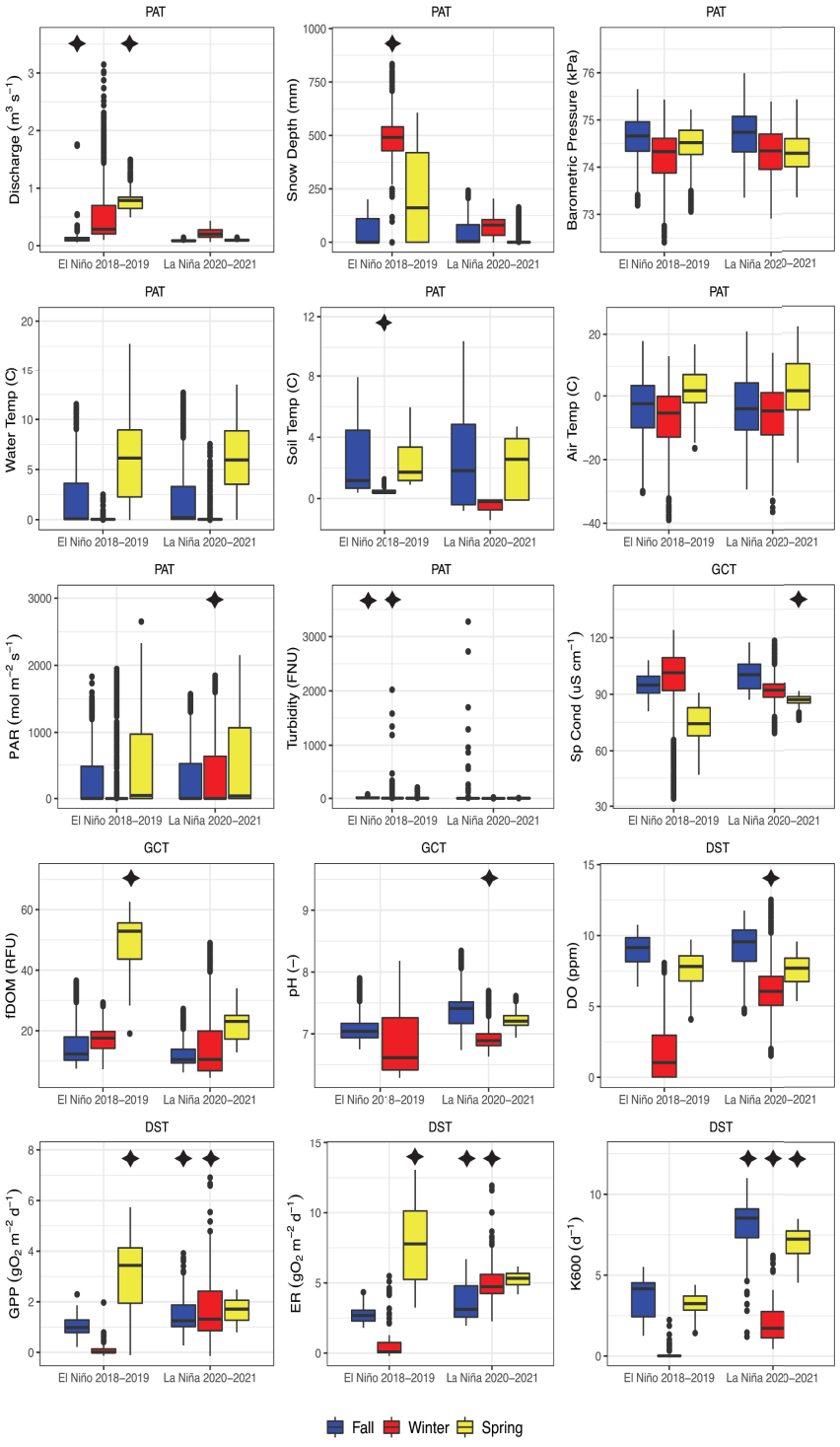

Figure 2.3: Boxplots comparing seasonal trends between the 2018-2019 El Niño and the 2020-2021 La Niña years. Asterisks represent quantities with statistically different means for the same season between years, and their location indicate which of the two years had a greater mean magnitude. Labels represent the physical and atmospheric (PAT), geochemical (GCT), and DO and stream metabolism (DST) templates.

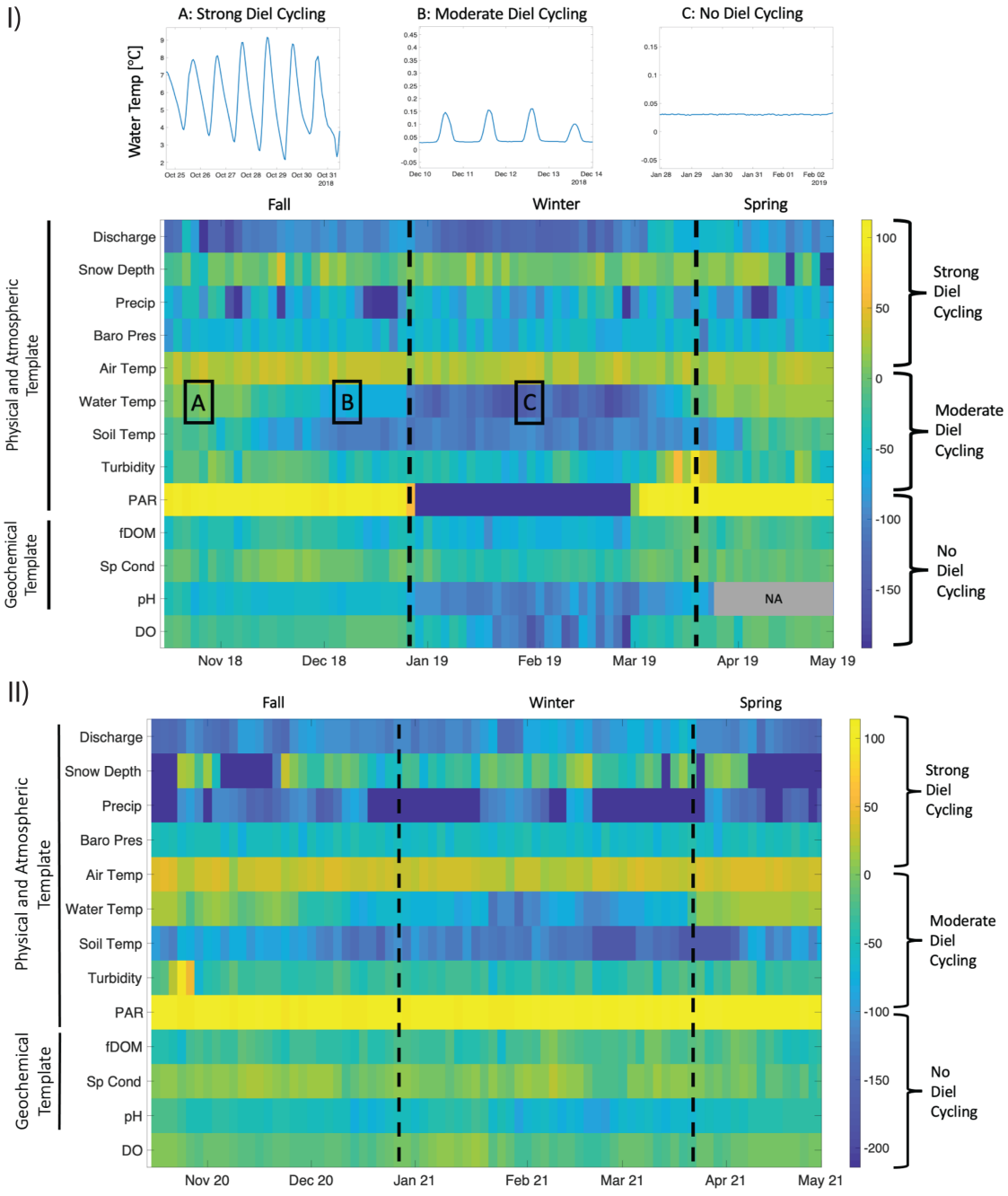

Figure 2.4: Heatmap of spectral power at 24-hour periodicity for I) El Niño 2018-2019 and II) La Niña 2020-2021 years organized by physical and atmospheric, and geochemical templates. For reference, we highlight examples of A: strong, B: moderate and C: no diel cycling for water temperature. Dashed vertical lines delineate fall, winter, and spring seasons. Missing pH values are shown as NA.

2.3.4 Interactions Between Templates:

Based on the PCA for the El Niño year (Figure 2.5A), PC1 separated winter points (negative PC1) from fall and spring (positive PC1). Positive PC1 values were primarily associated with higher temperatures (air, soil, and water), higher metabolic activity (GPP and ER), and weaker loadings for DO and fDOM. Negative PC1 values were most strongly related to snow depth and specific conductivity. PC2 separated spring days (positive PC2) from fall days (negative PC2), with winter days spanning positive and negative PC2 values. Positive PC2 was most strongly associated with discharge and snow depth, while negative PC2 was most strongly associated with DO coupled with K600.

Consistent with the El Niño year, PC1 for the La Niña year (Figure 2.5B) separated winter points (negative PC1) from fall and spring days (positive PC1). Also consistent with the El Niño year, positive La Niña PC1 values were primarily associated with higher temperatures and DO. However, in contrast to the El Niño year, neither metabolic activity (GPP or ER) or fDOM were strongly loaded on PC1.
Negative PC1 values for the La Niña year were most strongly related to discharge and snow depth. PC2 again separated spring days (positive PC2) from fall days (negative PC2), but positive PC2 was most strongly related to fDOM which coupled with PAR, while negative PC2 was most strongly related to specific conductivity.

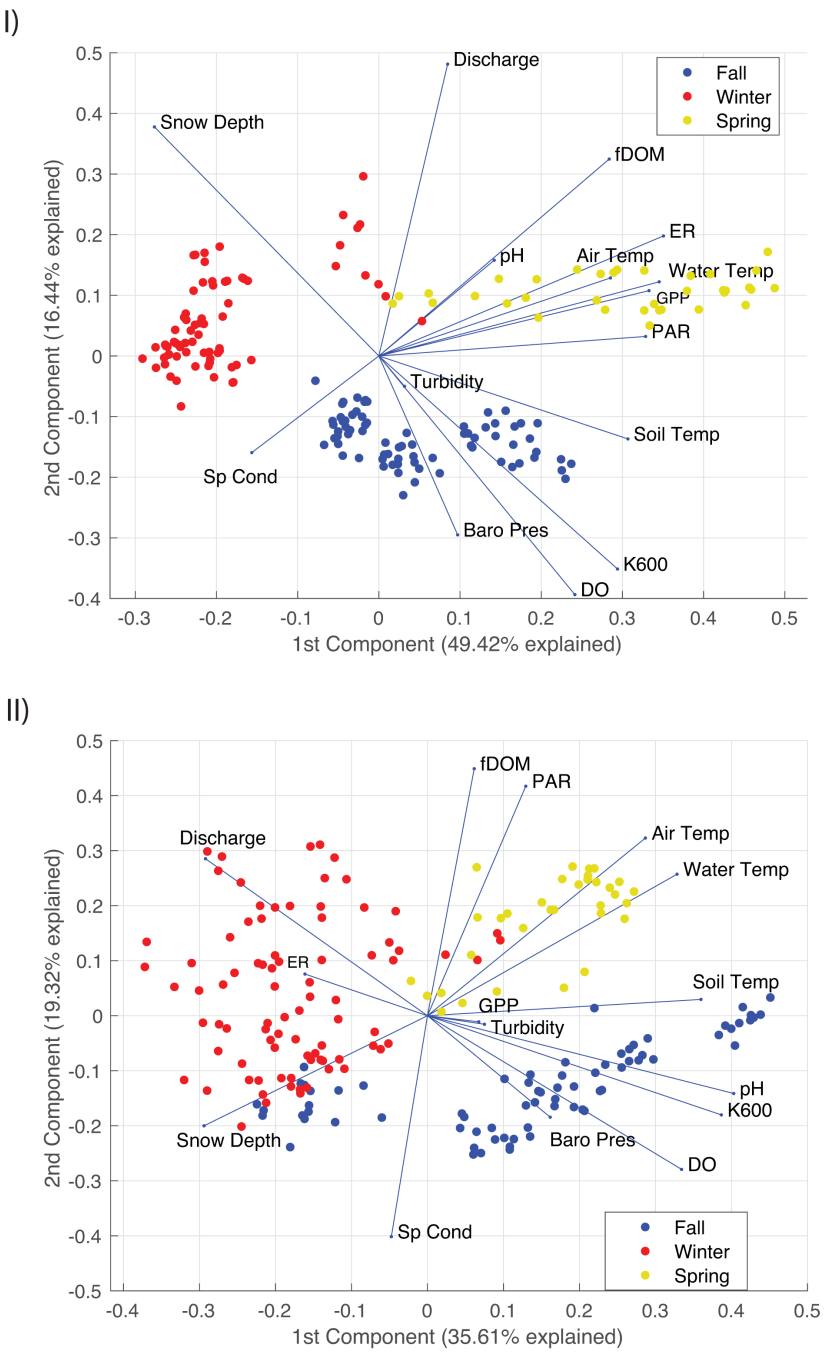

Figure 2.5: PCA biplot for daily averaged data for the I) 2018-2019 El Niño and II) 2020-2021 La Niña years. Parameters plotting in the same direction are positively correlated, those in opposite directions are negatively correlated, and those that are orthogonal are uncorrelated. Principal components one and two explained I) 65.86% and II) 54.93% of the total variation. Score values were added to the PCA biplot and are color-coded based on their respective period of analysis.

2.4. Discussion

2.4.1 Variable Interannual Snowpack Drives Lotic-Lentic Stream Transitions

The difference in snowpack between the two winters in this study continues to highlight the criticality of planetary-scale climatic controls on montane ecosystems, and their relevant implications to ecohydrology. During the El Niño year, as snowpack accumulated during the winter, stream depth was higher due to the downstream formation of ice dams resulting in a backup of water under the ice cover (Figure S2.4 and S2.5). Ice dams are known to occur where changes in stream slope and increases in substrate size are encountered (Turcotte et al., 2017), both of which are present immediately downstream of the research site as the EFJ River exits the low-gradient, fine substrate conditions of the Valles Caldera and enters a higher gradient reach with large cobble and boulder substrates. In addition to the ice dam, thick ice cover and frozen riparian soils would trap water within the channel. Such blockages have been shown to shift streams from fast-flow to slow-flow environments (Stickler et al., 2010). Thus, we suggest that the muted diel discharge signature and the increase in depth for the El Niño year signals a shift in function from a primarily lotic to primarily lentic environment (Figure S2.5).

2.4.2 Influence of Snowpack Variability on Stream Chemistry and Metabolism

Differences in snowpack dynamics also influenced stream chemistry, most notably the onset of persistent anoxia during the El Niño winter. Since atmospheric exchange is effectively cut off by ice and snow accumulation over the otherwise free surface of the stream, and groundwater exchange is an unlikely source of oxygen, we suggest that oxic conditions were maintained during the La Niña winter by a combination

of oxygenated inputs from upstream fluxes and in-stream GPP. In stark contrast to the El Niño winter, ER and GPP peaked in January of the La Niña year, indicating that winter metabolism was an important control on oxygen despite ice cover and light snowpack (Figure 2.2 and S2.5). In contrast, the anoxic conditions observed during the El Niño year suggests that the combination of reduced reaeration due to ice cover, the cessation of GPP as light availability declined, and the continuation of heterotrophic respiration, together resulted in the depletion of dissolved oxygen in the newly formed lentic-like conditions. Similar winter anoxia has been observed in other ice covered, low-flow, aquatic environments, including beaver dam ponds (Devito & Dillon, 1993) and lakes (Deshpande et al., 2015, 2017; Jansen et al., 2019). The importance of atmospheric forcing during the winter on stream metabolism suggests that snowpack has the potential to be as important for metabolism as other in-stream (e.g., hyporheic flow, algal overgrowth) and upslope (e.g., post-fire/precipitation ash and debris mobilization) ecological processes, not only during the winter but into the spring.

Using seven years of data collected between 2005-2011 during the spring and the fall seasons at the same study site (i.e., winter data were not available), we recently found unanticipated shifts from autotrophic to heterotrophic status within and across years (Summers et al., 2020). That study challenged previous paradigms where local attributes including geographic and landscape positioning (e.g., light and temperature regimes) were thought to control the trophic status of streams, and thus, streams were predicted to be either autotrophic or heterotrophic. Our findings from Summers et al. (2020) suggested that complex combinations of spatiotemporal factors, such as snow melt and summer precipitation, and their role in connecting terrestrial and aquatic ecosystems can

lead to substantial stream variation in metabolic status, which prompted us to start this winter-focused study, in an effort to fill the gap on the short and long-term ecological effects of winter dynamics noted in Tolonen et al. (2019) and Summers et al. (2020). Our findings are also consistent with previous research showing that reduced snowpack increases primary productivity in lakes (Garcia et al., 2019).

2.4.3 Implications of Changing Snowpack on Stream Function

Winter is the most rapidly changing season in the US, and its consistent warming causes reductions in snow pack, and shifts in the timing and volume of snowmelt (Climate Central, 2022; Elias et al., 2021; Godsey et al., 2014; Grimm et al., 2013; Reidmiller et al., 2018). The US Global Change Research Program indicate that atmospheric circulation patterns are changing due to global warming and will cause more aridity in the US southwest, where this study took place, particularly during La Niña years (Seager et al., 2007). Although our dataset represents two winter periods as examples, which limits our ability to comprehensively extrapolate our results to future climate predictions, we are able to gain some sense of expected physical, chemical, and metabolic responses to diminished winter snowpack.

Our study shows that stream metabolism in the spring is highly dependent on what happens in the winter, and the results from Summers et al. (2020) indicate that those winter-driven changes can also extend into the first part of the summer, before the monsoon season begins. Thus, winter precipitation changes have the potential to trigger multi-season, direct and indirect effects on in-stream physical, chemical, and biological processes. Moreover, as aerobic metabolism decreases under persistent anoxic conditions,

it is likely that redox conditions and associated cycles (e.g., denitrification) also shift. Prior studies identify many biogeochemical responses to anoxic conditions, including changes in the speciation of solutes mobilization of greenhouse gases, accumulation of silica, reduction of manganese, iron, phosphorous, and sulfate, and altered lability of exported dissolved organic and inorganic carbon stocks (Bicknell et al., 2020; Briggs et al., 2015; Harvey et al., 2013; Lautz & Fanelli, 2008; Navel et al., 2010; P. Regier et al., 2021; Sherson and Van Horn, et al., 2015; Zarnetske et al., 2011, 2012). Such significant shifts in biogeochemical cycles may paradoxically turn previously assumed winter "cold-spots" and "cold-moments" into hot-spots and hot-moments for biogeochemical processing.

Since our sensors did not capture the dynamics of anaerobic processes, and the winter ecology of streams remains understudied, we call for studies to focus on how winter driven anoxia activates ecological cycles that influence stream biogeochemistry through the rest of the year. This focus is timely because i) current data and climate projections suggest that winter is the most rapidly changing season and its warming is shifting the timing, amount, and type of precipitation, ii) in-stream freeze–thaw cycles, including ice and snow cover, occur in ~60% of river basins in the Northern Hemisphere and those ecosystems have evolved to sustain winter biogeochemical cycles, and iii) our study and others show that changes in winter precipitation patterns generate changes in stream metabolism, which propagate through the rest of the year. Accordingly, new studies should focus on investigating how losing the intermittency caused by freezing-thawing cycles due to global warming could negatively affect streams in high latitudes and altitudes, where freezing streams may become less abundant and frequent.

2.5 Conclusions

Winters are intuitively associated with ecological "cold-spots" and "cold-moments", i.e., lower than average ecological activity in space and time, but the effects of winter precipitation on stream metabolism and functioning are drastically understudied due to logistical challenges. We found that atmospheric forcing in the form of significant ice and snow cover during the winter drove drastic changes in oxygen availability and stream metabolism during a weak to moderate El Niño year (2018-2019). Two years later, during a moderate La Niña year (2020-2021), the same site underwent a significant reduction of snow cover, which not only resulted in a lack of winter anoxia but even in peak ER and GPP fluxes during the winter. Combining the two years of data, we found that winter and post-winter stream metabolism was highly dynamic and dependent on atmospheric forcing, which is changing due to the impacts of global warming on snowpack volume and timing particularly in the winter, the most rapidly warming season in the US.

Acknowledgements: The National Science Foundation provided support for this research through grants CBET-1707042, HRD- 1345169, HRD-1720912 and HRD-1914778.

Supplemental Information: Supplemental information for this publication is accessible at https://www.frontiersin.org/articles/10.3389/frwa.2022.1003159/full#supplementary-material

References:

Allard, G., Buffin-Bélanger, T., & Bergeron, N. (2011). Analysis of frazil ice as a geomorphic agent in a frazil pool. River Research and Applications, 27(9), 1136–1148. https://doi.org/10.1002/rra.1490

Appling, A. P., Hall, R. O., Yackulic, C. B., & Arroita, M. (2018). Overcoming Equifinality: Leveraging Long Time Series for Stream Metabolism Estimation. Journal of Geophysical Research: Biogeosciences, 123(2), 624–645. https://doi.org/10.1002/2017JG004140

Berghuijs, W. R., Woods, R. A., & Hrachowitz, M. (2014). A precipitation shift from snow towards rain leads to a decrease in streamflow. Nature Climate Change, 4(7), Article 7. https://doi.org/10.1038/nclimate2246

Bernhardt, E. S., Heffernan, J. B., Grimm, N. B., Stanley, E. H., Harvey, J. W., Arroita, M., Appling, A. P., Cohen, M. J., McDowell, W. H., Hall, R. O., Read, J. S., Roberts, B. J., Stets, E. G., & Yackulic, C. B. (2018). The metabolic regimes of flowing waters. Limnology and Oceanography, 63(S1), Article S1. https://doi.org/10.1002/lno.10726

Bicknell, K., Regier, P., Van Horn, D. J., Feeser, K. L., & González-Pinzón, R. (2020). Linking Hydrobiogeochemical Processes and Management Techniques to Close Nutrient Loops in an Arid River. Frontiers in Water, 2, 22. https://doi.org/10.3389/frwa.2020.00022

Briggs, M. A., Day-Lewis, F. D., Zarnetske, J. P., & Harvey, J. W. (2015). A physical explanation for the development of redox microzones in hyporheic flow. Geophysical Research Letters, 42(11), 4402–4410. https://doi.org/10.1002/2015GL064200

Climate Central. (2022). Warming Seasons. https://medialibrary.climatecentral.org/resources/warming-seasons

Cortés, G., & Margulis, S. (2017). Impacts of El Niño and La Niña on interannual snow accumulation in the Andes: Results from a high-resolution 31 year reanalysis. Geophysical Research Letters, 44(13), 6859–6867. https://doi.org/10.1002/2017GL073826

Davis, M. N., McMahon, T. E., Cutting, K. A., & Jaeger, M. E. (2020). Environmental and climatic factors affecting winter hypoxia in a freshwater lake: Evidence for a hypoxia refuge and for re-oxygenation prior to spring ice loss. Hydrobiologia, 847(19), 3983–3997. https://doi.org/10.1007/s10750-020-04382-z

Deshpande, B. N., MacIntyre, S., Matveev, A., & Vincent, W. F. (2015). Oxygen dynamics in permafrost thaw lakes: Anaerobic bioreactors in the Canadian subarctic. Limnology and Oceanography, 60(5), 1656–1670. https://doi.org/10.1002/lno.10126

Deshpande, B. N., Maps, F., Matveev, A., & Vincent, W. F. (2017). Oxygen depletion in subarctic peatland thaw lakes. Arctic Science, 3(2), 406–428. https://doi.org/10.1139/as-2016-0048

Devito, K. J., & Dillon, P. J. (1993). Importance of Runoff and Winter Anoxia to the P and N Dynamics of a Beaver Pond. Canadian Journal of Fisheries and Aquatic Sciences, 50(10), 2222–2234. https://doi.org/10.1139/f93-248

Elias, E., James, D., Heimel, S., Steele, C., Steltzer, H., & Dott, C. (2021). Implications of observed changes in high mountain snow water storage, snowmelt timing and

melt window. Journal of Hydrology: Regional Studies, 35, 100799. https://doi.org/10.1016/j.ejrh.2021.100799

Fang, X., & Stefan, H. G. (2009). Simulations of climate effects on water temperature, dissolved oxygen, and ice and snow covers in lakes of the contiguous U.S. under past and future climate scenarios. Limnology and Oceanography, 54(6part2), 2359–2370. https://doi.org/10.4319/lo.2009.54.6_part_2.2359

Frenette, J.-J., Thibeault, P., Lapierre, J.-F., & Hamilton, P. B. (2008). Presence of Algae in Freshwater Ice Cover of Fluvial Lac Saint-Pierre (st. Lawrence River, Canada)1. Journal of Phycology, 44(2), 284–291. https://doi.org/10.1111/j.1529-8817.2008.00481.x

Garcia, S. L., Szekely, A. J., Bergvall, C., Schattenhofer, M., & Peura, S. (2019). Decreased Snow Cover Stimulates Under-Ice Primary Producers but Impairs Methanotrophic Capacity. MSphere, 4(1), e00626-18. https://doi.org/10.1128/mSphere.00626-18

Goddard, L., & Gershunov, A. (2020). Impact of El Niño on Weather and Climate Extremes. In El Niño Southern Oscillation in a Changing Climate (pp. 361–375). American Geophysical Union (AGU). https://doi.org/10.1002/9781119548164.ch16

Godsey, S. E., Kirchner, J. W., & Tague, C. L. (2014). Effects of changes in winter snowpacks on summer low flows: Case studies in the Sierra Nevada, California, USA. Hydrological Processes, 28(19), 5048–5064. https://doi.org/10.1002/hyp.9943

Grimm, N. B., Chapin, F. S., Bierwagen, B., Gonzalez, P., Groffman, P. M., Luo, Y., Melton, F., Nadelhoffer, K., Pairis, A., Raymond, P. A., Schimel, J., & Williamson, C. E. (2013). The impacts of climate change on ecosystem structure and function. Frontiers in Ecology and the Environment, 11(9), 474–482. https://doi.org/10.1890/120282

Harvey, J. W., Böhlke, J. K., Voytek, M. A., Scott, D., & Tobias, C. R. (2013). Hyporheic zone denitrification: Controls on effective reaction depth and contribution to whole-stream mass balance: Scaling hyporheic flow controls on stream denitrification. Water Resources Research, 49(10), 6298–6316. https://doi.org/10.1002/wrcr.20492

Jansen, J., MacIntyre, S., Barrett, D. C., Chin, Y.-P., Cortés, A., Forrest, A. L., Hrycik, A. R., Martin, R., McMeans, B. C., Rautio, M., & Schwefel, R. (2021). Winter Limnology: How do Hydrodynamics and Biogeochemistry Shape Ecosystems Under Ice? Journal of Geophysical Research: Biogeosciences, 126(6), e2020JG006237. https://doi.org/10.1029/2020JG006237

Jansen, J., Thornton, B. F., Jammet, M. M., Wik, M., Cortés, A., Friborg, T., MacIntyre, S., & Crill, P. M. (2019). Climate-Sensitive Controls on Large Spring Emissions of CH4 and CO2 From Northern Lakes. Journal of Geophysical Research: Biogeosciences, 124(7), 2379–2399. https://doi.org/10.1029/2019JG005094

Jolliffe, I. T., & Cadima, J. (2016). Principal component analysis: A review and recent developments. Philosophical Transactions of the Royal Society A: Mathematical, Physical and Engineering Sciences, 374(2065), 20150202. https://doi.org/10.1098/rsta.2015.0202

Kirchner, J. W., Feng, X., & Neal, C. (2000). Fractal stream chemistry and its implications for contaminant transport in catchments. Nature, 403(6769), 524–527.

Krause, S., Lewandowski, J., Grimm, N., Hannah, D., Pinas., G., (2017). Ecohydrological interface as hot spots of ecosystem processes. Water Resources Research, 53, 8

Lautz, L. K., & Fanelli, R. M. (2008). Seasonal biogeochemical hotspots in the streambed around restoration structures. Biogeochemistry, 91(1), 85–104. https://doi.org/10.1007/s10533-008-9235-2

McClain, M. E., Boyer, E. W., Dent, C. L., Gergel, S. E., Grimm, N. B., Groffman, P. M., Hart, S. C., Harvey, J. W., Johnston, C. A., Mayorga, E., McDowell, W. H., & Pinay, G. (2003). Biogeochemical Hot Spots and Hot Moments at the Interface of Terrestrial and Aquatic Ecosystems. Ecosystems, 6(4), 301–312. https://doi.org/10.1007/s10021-003-0161-9

Meek, D., Hatfield, J., Howell, T., Idso, S., & Reginato, R. (1984). A generalized relationship between photosynthetically active radiation and solar radiation 1. Agronomy Journal, 76(6), Article 6.

Musselman, K. N., Addor, N., Vano, J. A., & Molotch, N. P. (2021). Winter melt trends portend widespread declines in snow water resources. Nature Climate Change, 11(5), Article 5. https://doi.org/10.1038/s41558-021-01014-9

Navel, S., Mermillod-Blondin, F., Montuelle, B., Chauvet, E., Simon, L., & Marmonier, P. (2010). Water–Sediment Exchanges Control Microbial Processes Associated with Leaf Litter Degradation in the Hyporheic Zone: A Microcosm Study. Microbial Ecology, 61(4), Article 4. https://doi.org/10.1007/s00248-010-9774-7

Odum, H. T. (1956). Primary production in flowing waters 1. Limnology and Oceanography, 1(2), 102–117.

O'Shaughnessy, P., & Cavanaugh, J. E. (2015). Performing T-tests to Compare Autocorrelated Time Series Data Collected from Direct-Reading Instruments. Journal of Occupational and Environmental Hygiene, 12(11), 743–752. https://doi.org/10.1080/15459624.2015.1044603

Palmer, M. A., Hondula, K. L., & Koch, B. J. (2014). Ecological Restoration of Streams and Rivers: Shifting Strategies and Shifting Goals. Annual Review of Ecology, Evolution, and Systematics, 45(1), 247–269. https://doi.org/10.1146/annurev-ecolsys-120213-091935

Petrov, M., Terzhevik, A. Y., Palshin, N., Zdorovennov, R., & Zdorovennova, G. (2005). Absorption of solar radiation by snow-and-ice cover of lakes. Water Resources, 32(5), 496–504.

Perdrial, J. N., McIntosh, J., Harpold, A., Brooks, P. D., Zapata-Rios, X., Ray, J., Meixner, T., Kanduc, T., Litvak, M., Troch, P. A., & Chorover, J. (2014). Stream water carbon controls in seasonally snow-covered mountain catchments: Impact of inter-annual variability of water fluxes, catchment aspect and seasonal processes. Biogeochemistry, 118(1–3), 273–290. https://doi.org/10.1007/s10533-013-9929-y

Price, D. S., Smith, D. W., & Stanley, S. J. (1995). Performance of lagoons experiencing seasonal ice cover. Water Environment Research, 67(3), 318–326. https://doi.org/10.2175/106143095X131538

Prowse, T. D. (2001). River-ice ecology. I: Hydrologic, geomorphic, and water-quality aspects. Journal of Cold Regions Engineering, 15(1), 1–16.

Prowse, T. D., Wrona, F. J., Reist, J. D., Hobbie, J. E., Lévesque, L. M. J., & Vincent, W. F. (2006). General features of the arctic relevant to climate change in freshwater ecosystems. Ambio, 35(7), 330–338. https://doi.org/10.1579/0044-7447(2006)35[330:gfotar]2.0.co;2

Regier, P., Ward, N. D., Indivero, J., Wiese Moore, C., Norwood, M., & Myers-Pigg, A. (2021). Biogeochemical control points of connectivity between a tidal creek and its floodplain. Limnology and Oceanography Letters, 6(3), 134–142. https://doi.org/10.1002/lol2.10183

Reidmiller, D. R., Avery, C. W., Easterling, D. R., Kunkel, K. E., Lewis, K. L. M., Maycock, T. K., & Stewart, B. C. (2018). Impacts, Risks, and Adaptation in the United States: The Fourth National Climate Assessment, Volume II. U.S. Global Change Research Program. https://doi.org/10.7930/NCA4.2018

Seager, R., Ting, M., Held, I., Kushnir, Y., Lu, J., Vecchi, G., Huang, H.-P., Harnik, N., Leetmaa, A., Lau, N.-C., Li, C., Velez, J., & Naik, N. (2007). Model Projections of an Imminent Transition to a More Arid Climate in Southwestern North America. Science, 316(5828), Article 5828. https://doi.org/10.1126/science.1139601

Sherson, L. R., Van Horn, D. J., Gomez-Velez, J. D., Crossey, L. J., & Dahm, C. N. (2015). Nutrient dynamics in an alpine headwater stream: Use of continuous water quality sensors to examine responses to wildfire and precipitation events: CONTINUOUS RESPONSES TO WILDFIRE AND PRECIPITATION

EVENTS. Hydrological Processes, 29(14), 3193–3207. https://doi.org/10.1002/hyp.10426

Stickler, M., Alfredsen, K. T., Linnansaari, T., & Fjeldstad, H.-P. (2010). The influence of dynamic ice formation on hydraulic heterogeneity in steep streams. River Research and Applications, 26(9), 1187–1197. https://doi.org/10.1002/rra.1331

Stroud Water Research Center. (2021). Model My Watershed [Software]. Available from https://wikiwatershed.org/

Summers, B. M., Horn, D. J. V., González-Pinzón, R., Bixby, R. J., Grace, M. R., Sherson, L. R., Crossey, L. J., Stone, M. C., Parmenter, R. R., Compton, T. S., & Dahm, C. N. (2020). Long-term data reveal highly-variable metabolism and transitions in trophic status in a montane stream. Freshwater Science, 39(2), Article 2. https://doi.org/10.1086/708659

Tolonen, K. E., Picazo, F., Vilmi, A., Datry, T., Stubbington, R., Pařil, P., Perez Rocha, M., & Heino, J. (2019). Parallels and contrasts between intermittently freezing and drying streams: From individual adaptations to biodiversity variation. Freshwater Biology, 64(10), 1679–1691. https://doi.org/10.1111/fwb.13373

Turcotte, B., Alfredsen, K., Beltaos, S., & Burrell, B. C. (2017). Ice-Related Floods and Flood Delineation along Streams and Small Rivers. 26.

Wagner, R. J., Boulger Jr., R. W., Oblinger, C. J., & Smith, B. A. (2006). Guidelines and standard procedures for continuous water-quality monitors: Station operation, record computation, and data reporting (Report No. 1-D3; Version 1.0, Techniques and Methods). USGS Publications Warehouse. https://doi.org/10.3133/tm1D3

Watras, C. J., Hanson, P. C., Stacy, T. L., Morrison, K. M., Mather, J., Hu, Y.-H., & Milewski, P. (2011). A temperature compensation method for CDOM fluorescence sensors in freshwater: CDOM temperature compensation. Limnology and Oceanography: Methods, 9(7), 296–301. https://doi.org/10.4319/lom.2011.9.296

Western Regional Climate Center. (2021). Hidden Valley (VC) New Mexico. Retrieved from https://wrcc.dri.edu/About/citations.php

Woods, P. F. (1992). Limnology of Big Lake, south-central Alaska, 1983-84. In Limnology of Big Lake, south-central Alaska, 1983-84 (USGS Numbered Series No. 2382; Water Supply Paper, Vol. 2382). U.S. Dept. of the Interior, U.S. Geological Survey ; Books and Open-File Reports Section [distributor],. https://doi.org/10.3133/wsp2382

Yellow Springs Instruments. n.d..

Zarnetske, J. P., Haggerty, R., Wondzell, S. M., & Baker, M. A. (2011). Labile dissolved organic carbon supply limits hyporheic denitrification. Journal of Geophysical Research, 116(G4), G04036. https://doi.org/10.1029/2011JG001730

Zarnetske, J. P., Haggerty, R., Wondzell, S. M., Bokil, V. A., & González-Pinzón, R. (2012). Coupled transport and reaction kinetics control the nitrate source-sink function of hyporheic zones: HYPORHEIC N SOURCE-SINK CONTROLS. Water Resources Research, 48(11). https://doi.org/10.1029/2012WR011894

Chapter 3: Longitudinal Propagation of Aquatic Disturbances From the Largest Wildfire Recorded in New Mexico, USA

Justin Nichols[1], Asmita Kaphle[1], Paige Tunby[1], Aashish Sanjay Khandelwal[1], Justin Reale[2], David J. Van Horn[3], Ricardo González-Pinzón[1]

[1]Department of Civil, Construction and Environmental Engineering, University of New Mexico, Albuquerque, New Mexico, USA, [2] U.S. Army Corps of Engineers, Albuquerque District, Albuquerque, NM, USA, [3]Department of Biology, University of New Mexico, Albuquerque, New Mexico, USA

Correspondence to: Justin Nichols justin67@unm.edu and Ricardo González-Pinzón gonzaric@unm.edu

Submitted to: Nature Communications Earth & Environment

DOI: 10.21203/rs.3.rs-3024492/v1

3.1 Introduction

Wildfires are increasing in frequency and extent across the western United States (US) and other regions of Earth (Ball et al., 2021; Flannigan et al., 2009; Westerling, 2016). These wildfires are associated with increased aridity and variability in precipitation patterns linked to global climate change (Cayan et al., 2001; Stewart et al., 2004; Westerling et al., 2006; Seager et al., 2007b; Westerling, 2016) and have been triggered by natural and anthropogenic factors (Allen et al., 2010; Breshears et al., 2005; Raffa et al., 2008; Weed et al., 2013; Williams et al., 2010). In addition to the impacts of wildfires to terrestrial ecosystems, property, and infrastructure, there is growing evidence that wildfires trigger cascading effects that propagate across fluvial networks, impacting environmental processes and ecosystem services in aquatic environments (Ball et al., 2021; Dahm et al., 2015b; Emmerton et al., 2020; Mast et al., 2016; Reale et al., 2015; Rhoades et al., 2019).

Wildfire impacts to environmental processes act as a pulse disturbance due to runoff associated with discontinuous precipitation events and a press disturbance when water quality is chronically impaired. The severity and duration of these impacts vary based on the characteristics of the watershed, burn severity, and the rate of ecosystem recovery (Proctor et al., 2020; Rhoades et al., 2019). Early acute impacts to environmental processes include sedimentation, debris flows, loss of riparian vegetation, and changes to water quality (Burton et al., 2016; Cerrato et al., 2016; Dahm et al., 2015b; Sherson and Horn, et al., 2015). Long-term, chronic impacts include increased rates of instream sediment loads, alterations of the habitat along the stream corridor, and long-term changes to water quality and nutrient loading (Mast et al., 2016; Neary et al.,

2016; Reale et al., 2015; Rhoades et al., 2018; Rust et al., 2019; Yu et al., 2019). Wildfires also affect multiple ecosystem services, including water purification and supply, soil and sediment management, flood attenuation, carbon and nutrient cycling, primary production, water quality, disease regulation, aesthetics and scenic resources, and recreational use (Adams, 2013; Bixby et al., 2015a; Brauman et al., 2007; Leemans, 2009).

Wildfire disturbances contribute to at least ten of the top twenty most crucial stream disturbances listed in US EPA water quality assessments, i.e., 1) elevated sediment levels, 2) nutrient enrichment, 3) organic enrichment and oxygen depletion, 4) elevated temperature, 5) elevated instream metal concentrations, 6) habitat alterations, 7) elevated turbidity, 8) flow alterations, 9) elevated salinity and total dissolved solids, and 10) changes to pH and conductivity. Paradoxically, while wildfire is known to contribute to these impairments and the disruption of vital ecosystem services, it is frequently excluded as a source of disturbance due to the unpredictable nature of wildfires and the logistical challenges of monitoring water quality post-fire (Ball et al., 2021).

Post-fire water quality propagation data have only been fortuitously measured in a few study cases where sensors had been deployed to monitor other non-fire-related water quality issues. The limited data available have revealed impacts over hundreds of kilometers downstream of the burn scar (Abram et al., 2003; Dahm et al., 2015a; Reale et al., 2015), primarily affecting reservoirs and municipal water supply systems, with associated restoration costs in the millions of dollars (Bladon et al., 2014). Temporally, fire inputs can persist within streams for years post-fire, influencing ecosystems and

overall stream functioning (Bêche et al., 2005; Bixby et al., 2015b; Earl & Blinn, 2003; Spencer et al., 2007).

Since current fire models consistently predict that the prevalence of wildfire and associated damage will continue to increase due to anthropogenic climate change and forest management practices (Abatzoglou & Williams, 2016; Adams, 2013; Calkin et al., 2015; North et al., 2015; Westerling et al., 2011), we need to quantify and predict the propagation of wildfire disturbances through fluvial networks. This knowledge gap hinders our ability to mitigate wildfire impacts on water quality and protect vital aquatic ecosystem services(Murphy et al., 2023).

We deployed a rapid response team to monitor first-flush watershed responses and longer-term trends associated with wildfire disturbance propagation from the Hermit's Peak – Calf Canyon wildfire (HPCC), the current largest fire recorded in New Mexico (Figure 3.1). The HPCC wildfire began on April 6th, 2022, and was contained on August 21st, 2022, after burning 1,382 km^2. Approximately 87% of the Gallinas Creek watershed burned, of which 19% was designated high severity, 25% moderate, and 43% low severity (Figure S3.1). We focused our monitoring along the 190km Gallinas Creek-Pecos River-Santa Rosa Lake fluvial network because Gallinas Creek supplies approximately 95% of the municipal water supply to 7,200 people living in the City of Las Vegas, NM, located ~25 km downstream of its headwaters (Huey & Meyer, 2010).

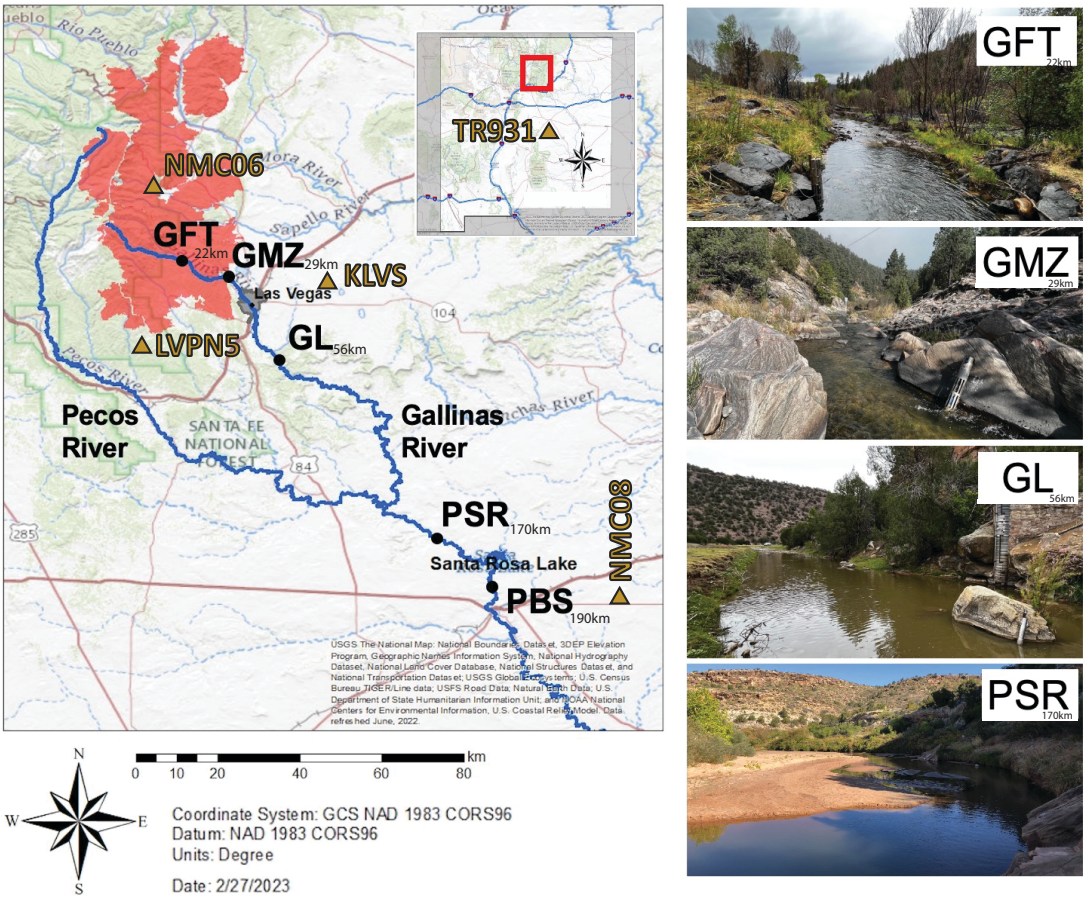

Figure 3.1: Water quality and meteorological monitoring. The red area represents the burn scar boundary of the Hermit's Peak – Calf Canyon wildfire. $GFT_{22\ km}$, Gallinas Creek near La Placita fire station, 22 km downstream from the headwaters of Gallinas Creek; $GMZ_{29\ km}$, Gallinas Creek near Montezuma; $GL_{56\ km}$, Gallinas Creek near Lourdes; $PSR_{170\ km}$, Pecos River upstream of Santa Rosa Lake; $PBS_{190\ km}$, Pecos River downstream of Santa Rosa Lake. Gold triangles represent the locations of MesoWest climate stations used for atmospheric data. Photos from $PBS_{190\ km}$ are shown in the Supplementary Information.

Two weeks after the fire began, we deployed YSI EXO multiparameter water quality sondes (Yellow Springs Instruments, n.d.) at three sites within the Gallinas Creek watershed, i.e., at La Placita fire station in Gallinas, NM (referred to as $GFT_{22\ km}$, as it is located 22 km from the headwaters of Gallinas Creek, our 0 km reference point), near Montezuma, NM ($GMZ_{29\ km}$), and near Lourdes, NM ($GL_{56\ km}$). Two additional sondes

on the Pecos River ($PSR_{170\ km}$ and $PBS_{190\ km}$) were deployed in late 2020 to monitor water quality upstream and downstream of Santa Rosa Lake through a partnership between USACE and the University of New Mexico (Figure 3.1). We used those sites to compare changes pre- and post-fire. All EXO sondes measured water temperature, specific conductivity, dissolved oxygen (DO), turbidity, and pH at 15-min intervals. In addition, the sondes in the Gallinas Creek watershed measure fluorescent dissolved organic matter (fDOM) at 15-min intervals (Table S3.1). All sondes were cleaned and calibrated monthly, following guidelines from the U.S. Geological Survey (USGS) (Wagner et al., 2006). Discharge and meteorological data from multiple stations near water quality monitoring sites were used to contextualize the generation and propagation of wildfire disturbances (see Methods). Gross primary production (GPP) and ecosystem respiration (ER) were estimated from sensor data using StreamMetabolizer (see Methods). Also, metabolic fingerprints(Bernhardt et al., 2018), which relate GPP and ER kernel distributions, were used to qualitatively compare metabolic regimes in response to changing site conditions and pulse events.

Based on flow time-series analyses (see Methods), we defined a pre-monsoon period from the beginning of our monitoring on April 25th, 2022, to June 26th, 2022; a monsoon (high precipitation-runoff) period from June 26th, 2022, to September 13th, 2022; and a post-monsoon from September 13th, 2022, to December 1st, 2022. The same three periods of analyses were used at $PSR_{170\ km}$ and $PBS_{190\ km}$ to compare the data from 2021 and 2022. With the data collected, we addressed 1) how far downstream water quality disturbances propagate following a wildfire, 2) what is the role of seasonality in

that propagation, and 3) what is the impact of a downstream lake in mitigating further longitudinal propagation.

3.2 Methods

3.2.1 Site and Wildfire Descriptions

Gallinas Creek is a perennial stream, and most of its flow is associated with snowmelt during the spring and monsoonal storms in the summer and fall. The catchment supplies approximately 95% of the municipal water supply to 7,200 people living in the City of Las Vegas, NM, located ~25 km downstream of its headwaters (Huey & Meyer, 2010). Further downstream, Gallinas Creek flows through a mix of canyonlands and farmlands before joining the Pecos River, ~142 km from its headwaters (Figure 3.1). The Pecos River flows into Santa Rosa Lake, located ~ 43 km downstream of the confluence with Gallinas Creek. This reach of the Pecos River is perennial, except for short reaches of intermittent flow between Anton Chico and Colonias, NM (USBOR & NMISC, 2021). Santa Rosa Lake is operated by the U.S. Army Corp of Engineers (USACE) for flood control, irrigation, and sediment retention. Water releases from Santa Rosa Lake typically occur only during block releases, which are typically 15-40 m^3/s for a period of 5-15 days. The frequency of these releases depends on available reservoir storage and irrigation demand, but cannot exceed 65 days (Moore et al., 2022). However, the reach downstream of the Lake to the City of Santa Rosa remains perennial due to groundwater inputs.

3.2.2 Monitoring Description

Discharge and meteorological data: Discharge and stage data were also collected at 15-minute intervals at stream gages maintained by the USGS (Nos. 08380400, 08380500, 08382000, 08382650, and 08382830) collocated or proximal to sonde sites $GFT_{22\ km}$, $GMZ_{29\ km}$, $GL_{56\ km}$, $PSR_{170\ km}$, and $PBS_{190\ km}$, respectively (U.S. Geological Survey, 2022). During periods before the deployment of non-contact radar, the height at 08380400 was estimated using a 2-hour lagged relationship between heights from USGS gages 08380500 and 08380400.

Meteorological data were exported from MesoWest with barometric pressure being measured at climate station KLVS, and precipitation and solar radiation were recorded at climate stations LVPN5, TR931, NMC06, and NMC08 at 10-min intervals (Figure 3.1 and Table S3.2) (MesoWest, 2022). Precipitation and solar radiation time series from multiple sites were aggregated to a single time series by taking the weighted average on the proximity of a sonde site to the respective climate station. Differences between the site's readings and KLVS's barometric pressure were accounted for by a factor of 0.16 KPa per 15.3 m elevation difference.

Data quality control, assurance, and conversions: Raw and converted data were processed for outliers and sensor drift with Aquarius Timeseries 21.1 (Aquatic Informatics, Vancouver, Canada). Erroneous outliers were eliminated using a moving average filter targeting points deviating more than 20% from a two-hour moving window. We corrected sensor drift and biofouling by comparing pre- and post-cleaning and calibration values and applied a linear correction from the date of the previous maintenance (Wagner et al., 2006). Lastly, we performed a final visual inspection of data quality.

A high discharge event on September 10th, 2022, damaged the sonde at the $GFT_{22\ km}$ monitoring site, effectively terminating data collection on August 28th, 2022 (Table S3.4). At $GL_{56\ km}$, sensor connectivity issues halted data recording from June 20th to July 11th, 2022. Starting September 4th, 2022, the DO sensor at $PSR_{170\ km}$ was damaged, producing negative values, and was excluded from the analysis. Also, at $PSR_{170\ km}$ and $PBS_{190\ km}$, there were periods with data removed because the sondes were buried or out of the water column. On August 10th, 2022, the sonde at $PBS_{190\ km}$ was pulled for routine calibration, but high flow prevented its redeployment until September 14th, 2022. Also, a firmware issue prevented data from being recorded from May 18th to June 17th, 2022.

fDOM was corrected for changes in water temperature and turbidity using the following equations (Downing et al., 2012):

$$\mathrm{fDOM_{temp}} = \frac{\mathrm{fDOM}}{1+\rho(\mathrm{W_T}-\mathrm{T_l})} \quad (1),$$

$$\mathrm{fDOM}_{cor} = \frac{\mathrm{fDOM_{temp}}}{\mathrm{a+b}*exp^{(c*turb)}} \quad (2),$$

where $\mathrm{fDOM_{temp}}$ is the temperature corrected fDOM concentration (QSU); fDOM is the uncorrected fDOM concentration (QSU); ρ is temperature-specific fluorescence coefficient of $-7.545 \times 10^{-3}\ °\mathrm{C}^{-1}$; $\mathrm{W_T}$ is the water temperature (°C); $\mathrm{T_l}$ is the lab temperature of 22 °C when fDOM was calibrated; $\mathrm{fDOM_{cor}}$ is the temperature and turbidity corrected fDOM concentration (QSU); $turb$ is the water turbidity (FNU); a, b, and c are turbidity correction coefficients of 0.38901, 0.72842, and -0.00618 when turbidity is less than 600 FNU, or 0.17573, 0.25597, and -0.00038 when turbidity is greater than 600 FNU (P. J. Regier et al., 2020).

Photosynthetically active radiation (PAR) was derived by multiplying total solar radiation by a factor of 2.04 (Meek et al., 1984b). Average stream depth was derived by

dividing the measured cross-sectional area by stream width from 2000 to 2022 USGS field measurements taken at each stream gage.

3.2.3 Estimates of Stream Metabolism

Stream metabolism modeling: We estimated daily averages of stream metabolism using the USGS streamMetabolizer model (Appling et al., 2018), which uses a one-station model based on the open-channel metabolism approach (Odum, 1956), and incorporates inverse Bayesian Markov Chain Monte Carlo modeling. The equations used in streamMetabolizer are:

$$\frac{dDO_t}{dt} = \frac{1}{Z_t}\left(\frac{GPP(t_1-t_0)*PPFD_t}{\int_{u=t_0}^{t_1} PPFD_u du} + ER\right) + \frac{K_{600}(DO_{sat,t}-DO_{mod,t})}{\sqrt{\frac{S_A-S_B T_t+S_C T_t^2+S_D T_t^3}{600}}} \quad (3),$$

$$DO_{mod,t} = DO_{mod,t-\Delta t} + \int_{u=t-\Delta t}^{t}\left(\frac{dDO_{mod,u}}{du} + \varepsilon_{proc,u}\right) du \quad (4),$$

$$DO_{obs,t} = DO_{mod,t} + \varepsilon_{obs,t} \quad (5),$$

where DO_t is the observed dissolved oxygen (mg L^{-1}) at time t; $DO_{sat,t}$ is the hypothetical saturated DO concentration (mg L^{-1}); $DO_{mod,t}$ is the modeled DO concentration (mg L^{-1}); ε_{obs} and ε_{proc} are the observation and processes error; t_0 and t_1 are the beginning and end of the day (d); Z_t is stage (m); $PPFD_t$ is photosynthetic photon flux density (µmol m^{-2} d^{-1}); T_t is the water temperature (°C); $S_{A,B,C,D}$ are dimensionless Schmidt coefficients (-); GPP is the daily average areal rate of gross primary production ($gO_2\ m^{-2}\ d^{-1}$); ER is the daily average areal rate of ecosystem respiration ($gO_2\ m^{-2}\ d^{-1}$); and K_{600} is the standardized gas exchange rate coefficient (d^{-1}).

Stream metabolic fingerprints: We used the stream metabolic fingerprint technique (Bernhardt et al., 2018) to compare stream metabolism patterns across periods of analysis and monitoring sites. This technique analyzes GPP and ER kernel distributions to qualitatively compare metabolic regimes in response to changing site conditions and pulse events (Figure 3.3F) (Bernhardt et al., 2018). We derived GPP and ER kernel distributions using the R package MASS's *kde2d* function at a bandwidth of 7.5. The *kde2d* function is a nonparametric representation of the probability density function that is useful when data do not fall within a Gaussian distribution (Venables & Ripley, 2002).

3.2.4 Periods of Analysis and Statistical Tests

Periods of Analysis: Due to the dominant influence of rainfall-runoff events in wildfire disturbance generation and longitudinal propagation, we used changes in mean discharge values to establish periods to guide our time-based comparisons. For this, we used MATLAB's *ischange* function with discharge data from USGS stream gage 08380500, which had the greatest number of records available near the burned perimeter. MATLAB's *ischange* function determines points of significant change in a time series mean trend (Killick et al., 2012).

Diel cycling analysis: We generated spectrograms using the *pspectrum* function in Matlab for water temperature, pH, and DO to monitor changes associated with physical, chemical, and biological signals (Nichols et al., 2022; Nimick et al., 2011). Spectrograms use discrete, short-time Fourier transforms to quantify the significance of sinusoidal signals at multiple frequencies or periodicities within a time series. We

extracted the spectral power at a periodicity of 24 hours to quantify diel cycling within the time series. We also generated heatmaps that quantify when a diel signal reached its peak value within 24 hours for the same time series used for frequency analysis. For this, we used Matlab's *findpeaks* function with a minimum peak distance of 12 hours to determine the time diel cycling reached in maximum value during 24 hours. The daily peak times were then aggregated to weekly values by taking the median peak times for each week. These diel cycling analyses were combined with stream metabolism to understand the role of seasonality in the longitudinal propagation of wildfire disturbances.

Maximum daily discharge exceedance probability: We computed exceedance probabilities of maximum daily discharge from recorded values upstream of Santa Rosa Lake to compare flow changes pre- and post-fire. Discharge records available spanned from October 1st, 1990, to December 1st, 2022, for stream gages 08380500 and 08382650, and March 13th, 2006, to December 1st, 2022, for stream gage 08382000. We used the maximum daily value observed in 15-min during 24 hours to calculate exceedance probabilities, $P_{exc.}$:

$$P_{exc.} = 100\,\frac{m}{(n+1)} \qquad (6),$$

where m is an index representing ranked values of discharge from highest to lowest for the total number of daily discharge observations n. Low $P_{exc.}$ values indicate atypical high-flow events, and high values indicate commonly observed flows. In this work, when $P_{exc.} < 1\%$, the event is classified as a high-flow event.

Principal component and multi-comparison analysis: We used Matlab's *pca* function to generate principal component analysis (PCA) and examine relationships

between water quality parameters and stream metabolism estimates. The first two principal components were used for statistical analysis since they explained approximately 60% of the total variance at each sonde site. We plotted the first two principal components in a biplot. Parameters aligned in the same direction represent positive correlations, those in opposite directions represent negative correlations, and those orthogonal are uncorrelated (Jolliffe & Cadima, 2016). We also categorized by color the latent space daily points in each period of analysis to understand their dominance. Daily mean water quality values were derived to align with the timestep of stream metabolism estimates. Lastly, we standardized each parameter's daily average by centering its mean at zero and scaling by its standard deviation to make parameters with varying magnitudes and units comparable:

$$S_X = \frac{X - \mu_X}{\sigma_X} \quad (7),$$

where S_X is the standardized parameter X (-), and μ_X and σ_X are the mean and standard deviation of parameter X.

Comparison tests: We used Pairwise Wilcoxon Rank Sum tests to compare period-to-period changes. The Pairwise Wilcoxon Rank Sum is a nonparametric, multiple comparison test that determines if groups within the data are statically similar, the null hypothesis, or significantly different (Mast et al., 2016; Wickham & Grolemund, 2016). We used the Holm-Bonferroni method to calculate p-values to minimize family-wise error rates. Each time series was aggregated to 5-day averages to reduce autocorrelation and type one error, except for $PBS_{190\ km}$, which required 3-day averages due to a reduced number of days of observation during the pre-monsoon period.

3.3 Results

3.3.1 Seasonal Changes in Flow

There were no high-flow events during the pre-monsoon period (Figure S3.2). Discharges upstream of Santa Rosa Lake were at the lowest values in that period during the fire year, with average values ranging from 0.02 to 0.17 m^3/s (Tables S3.2 and S3.3). In mid-June, a block release from Santa Rosa Lake increased the average discharge at $PBS_{190\ km}$ to 2.81 m^3/s for approximately 8 days.

During the monsoon period, 243 mm of precipitation fell on the burn scar, mainly between July 26th-30th (70 mm) and August 17th to 18th (42 mm). Twelve high-flow events occurred at the $GMZ_{29\ km}$ site, two at $GL_{56\ km}$, and one at $PSR_{170\ km}$ in this period (Figures S3.2 and S3.3). Maximum discharges across the three sites were 66.0, 20.4, and 68.0 m^3/s, corresponding to high flow events with low exceedance probabilities of 0.06, 0.58, and 0.75%, respectively (Figure S3.3). Average discharges across all sites ranged from 1.30 to 7.93 m^3/s, with the lowest value measured at $GL_{56\ km}$ and the highest at $PSR_{170\ km}$ (Tables S3.2 and S3.3).

During the post-monsoon period, 110 mm of precipitation fell within the burn scar. Most precipitation occurred between October 3rd-8th and October 16th, with 57 mm and 34 mm of precipitation, respectively. The highest peak discharge values were 6.8, 3.8, and 15.1 m^3/s at the $GMZ_{29\ km}$, $GL_{56\ km}$, or $PSR_{170\ km}$ sites, with exceedance probabilities of 1.3, 2.3, and 6.2%, respectively (Figure S3.3). Average post-monsoon discharges across all sites ranged from $3x10^{-4}$ to 2.1m^3/s, with the lowest value measured at $PBS_{190\ km}$ and the highest at $PSR_{170\ km}$ (Tables S3.2 and S3.3; Figure 3.2).

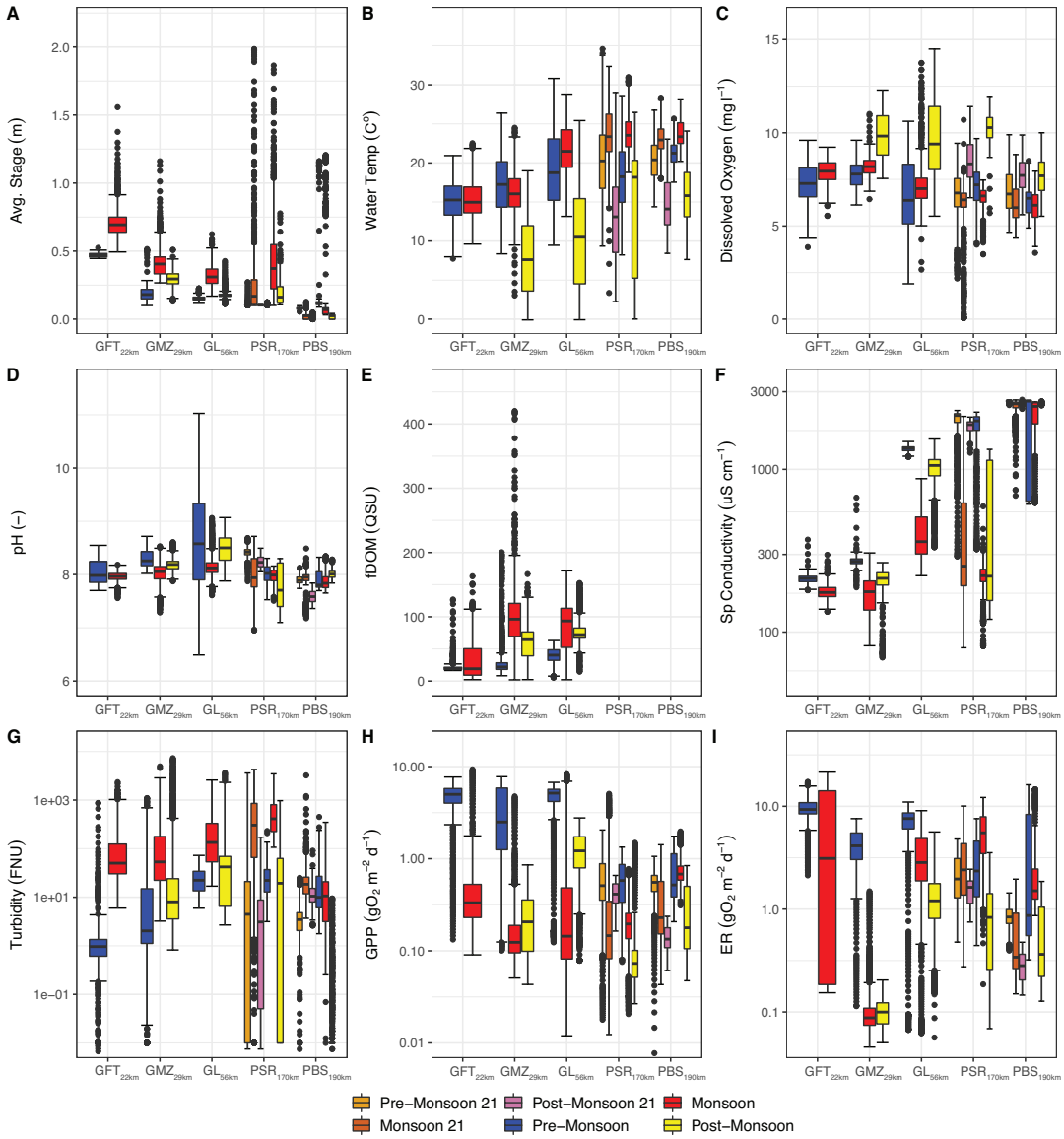

Figure 3.2: Boxplots of parameters and fluxes from all monitoring sites, grouped by analysis period. The statistical comparisons between periods are presented in Table 1. $GFT_{22\ km}$, Gallinas Creek near La Placita fire station, 22 km downstream from the headwaters of Gallinas Creek; $GMZ_{29\ km}$, Gallinas Creek near Montezuma; $GL_{56\ km}$, Gallinas Creek near Lourdes; $PSR_{170\ km}$, Pecos River upstream of Santa Rosa Lake; $PBS_{190\ km}$, Pecos River downstream of Santa Rosa Lake.

3.3.2 Seasonal Changes in Water Quality Parameters

During the pre-monsoon period, turbidity and fDOM were at their lowest values of the fire year at sites upstream of Santa Rosa Lake, with averages ranging from 5.93 to

62.7 FNU and 21.7 to 38.7 QSU (Tables S3.2 and S3.3). The $PBS_{190\ km}$ site, downstream of the lake, had its highest turbidity of the fire year, with an average of 26.3 FNU. There was an increase in specific conductivity from the headwaters to the lower sites, with a 1,870 uS/cm difference between $GFT_{22\ km}$ and $PBS_{190\ km}$ pre-monsoon averages (Figures 3.2 and S3.2; Tables S3.2 and S3.3).

With respect to the pre-monsoon, most water quality parameters significantly changed at the stations upstream of Santa Rosa Lake (i.e., $GFT_{22\ km}$, $GMZ_{29\ km}$, $GL_{56\ km}$, and $PSR_{170\ km}$) during the monsoon period, and only a few changed downstream of the lake at $PBS_{190\ km}$ (Table 3.1). At $GFT_{22\ km}$, water temperature and fDOM were the only quantities that did not change significantly. At $GMZ_{29\ km}$, only the water temperature did not change. At $GL_{56\ km}$ and $PSR_{170\ km,}$ only DO, and pH did not change. At $PBS_{190\ km}$, DO, specific conductivity, pH, and turbidity did not change. Summarizing the main changes during the monsoon period, the average values of fDOM increased from 33 to 96 QSU at $GMZ_{29\ km}$ (Table S3.2) and from 39 to 83 QSU at $GL_{56\ km}$. Turbidity experienced a significant increase at the monitoring sites upstream of Santa Rosa Lake (Figures 3.2 and S3.2), with period averages ranging from 149 to 574 FNU. However, unlike observed values at locations upstream of the lake, $PBS_{190\ km}$ experienced minimal reductions in turbidity, with a period average of 16 FNU. Specific conductivity significantly decreased at monitoring sites upstream of Santa Rosa Lake, with average ranges of 172 to 442 uS/cm, while it remained relatively high at $PBS_{190\ km}$, averaging 2087 uS/cm (Tables 3.1 and S3.2).

Table 3.1: p-values from Pairwise Wilcoxon Rank Sum tests between periods of analysis, i.e., pre-M, M, and post-M indicating pre-monsoon, monsoon, and post-monsoon. Light green shows statically significant differences at p-values <0.05.

Site	Season	Stage and Discharge	DO	Water Temp	fDOM	Specific Cond.	pH	Turbidity	GPP	ER
GFT_2 2 km	Pre-M vs M	0.00	0.02	0.47	0.65	0.00	0.00	0.00	0.00	0.5
	M vs Post-M	NA	NA	NA	NA	NA	NA	NA	NA	NA
	Pre-M vs Post-M	NA	NA	NA	NA	NA	NA	NA	NA	NA
GMZ 29 km	Pre-M vs M	0.00	0.03	0.37	0.00	0.00	0.00	0.04	0.00	0.00
	M vs Post-M	0.00	0.00	0.00	0.00	0.04	0.00	0.06	0.45	0.74
	Pre-M vs Post-M	0.00	0.00	0.00	0.04	0.00	0.01	0.21	0.00	0.00
GL_{56} km	Pre-M vs M	0.00	0.23	0.02	0.04	0.00	0.60	0.00	0.00	0.00
	M vs Post-M	0.00	0.01	0.00	0.43	0.00	0.02	0.01	0.00	0.00
	Pre-M vs Post-M	0.00	0.00	0.00	0.00	0.00	0.85	0.72	0.00	0.00
PSR_1 70 km	21 vs 22 Pre-M	0.00	0.74	0.31	NA	0.83	0.00	0.21	0.98	0.83
	21 vs 22 M	0.00	0.46	0.98	NA	0.07	0.98	0.98	0.98	0.00
	21 vs 22 Post-M	0.00	0.02	0.98	NA	0.00	0.01	0.83	0.00	0.00
	Pre-M vs M	0.00	0.46	0.00	NA	0.00	0.98	0.00	0.00	0.01
	M vs Post-M	0.00	0.02	0.00	NA	0.98	0.98	0.00	0.00	0.00
	Pre-M vs Post-M	0.00	0.00	0.98	NA	0.00	0.98	0.98	0.02	0.00
PBS_1 90 km	21 vs 22 Pre-M	0.00	0.98	0.59	NA	0.93	0.99	0.07	0.40	0.40
	21 vs 22 M	0.00	0.98	0.22	NA	0.88	0.94	0.42	0.00	0.00
	21 vs 22 Post-M	0.00	0.98	0.25	NA	0.00	0.00	0.00	0.08	0.04
	Pre-M vs M	0.01	0.75	0.02	NA	0.98	0.96	0.98	0.98	0.97

Table 3.1: p-values from Pairwise Wilcoxon Rank Sum tests between periods of analysis, i.e., pre-M, M, and post-M indicating pre-monsoon, monsoon, and post-monsoon. Light green shows statically significant differences at p-values <0.05.

Site	Season	Stage and Discharge	DO	Water Temp	fDOM	Specific Cond.	pH	Turbidity	GPP	ER
	M vs Post-M	0.00	0.00	0.00	NA	0.00	0.02	0.00	0.00	0.00
	Pre-M vs Post-M	0.00	0.02	0.02	NA	0.98	0.98	0.03	0.02	0.21

Most water quality parameters significantly changed at all stations between the monsoon and post-monsoon periods. At $GMZ_{29\ km}$, turbidity changes had a marginal p-value=0.06. At $GL_{56\ km}$, only fDOM did not change significantly. At $PSR_{170\ km}$, only DO, and pH did not change. At $PBS_{190\ km}$, all quantities changed (Table 3.1). Summarizing the main changes during the post-monsoon period, fDOM significantly decreased at $GMZ_{29\ km}$ (Table 3.1) with respect to the monsoon season, with an average period value of 58 QSU. Turbidity increased near the burn scar to an average of 260 FNU at $GMZ_{29\ km}$ but significantly decreased at the $GL_{56\ km}$, $PSR_{170\ km}$, and $PBS_{190\ km}$, averaging 85, 48, and 0.2 FNU, respectively (Table S3.2). Specific conductivity experienced significant increases at $GMZ_{29\ km}$, $GL_{56\ km}$, $PSR_{170\ km}$, and $PBS_{190\ km}$, averaging 210, 992, 537, and 2573 uS/cm, respectively (Tables 3.1, S3.2, S3.3; Figure 3.2).

Between the pre-monsoon and post-monsoon periods, most parameters changed significantly. At $GMZ_{29\ km}$, only turbidity did not change. At $GL_{56\ km}$, only pH and turbidity did not change. At $PSR_{170\ km}$, water temperature, pH, and turbidity did not change. At $PBS_{190\ km}$, specific conductivity and pH did not change (Table 3.1).

3.3.3 Seasonal Changes in Stream Metabolism

GPP averages ranged from 0.6 to 4.9 $gO_2\ m^{-2}\ d^{-1}$ during the pre-monsoon period, with the lowest and highest values occurring at $PSR_{170\ km}$ and $GL_{56\ km}$, respectively (Tables S3.2 and S3.3). ER averages ranged from 3.1 to 9.5 $gO_2\ m^{-2}\ d^{-1}$, with the lowest and highest values occurring at $PSR_{170\ km}$ and $GFT_{26\ km}$, respectively (Figures 3.2 and S3.2). The metabolic fingerprint distributions across monitoring sites upstream of Santa Rosa Lake had centroids with larger ER vs. GPP values and uniform spreads (Figure 3.3). In contrast, $PBS_{190\ km}$ had two centroids, i.e., one falling on the 1:1 line (0.5, -0.5) and another with heightened ER (1, -15), which was associated with the block release period (Figure 3.3E). Conceptually, kernel distributions favoring high ER and low GPP indicate increased organic matter, nutrient, and sediment fluxes; distributions near zero GPP and ER indicate scouring of the benthic zone; distributions that fall on a 1:1 ratio between GPP and ER indicate metabolic equilibrium (Bernhardt et al., 2018).

With respect to the pre-monsoon, GPP and ER changed at most sites during the monsoon period, except at $PBS_{190\ km}$. ER did not change significantly at $GFT_{22\ km}$ (Table 3.1). Upstream of Santa Rosa Lake, GPP was reduced with respect to the pre-monsoon, with average values ranging from 0.2 $gO_2\ m^{-2}\ d^{-1}$ at $GMZ_{29\ km}$ and $PSR_{170\ km}$ to 1.3 $gO_2\ m^{-2}\ d^{-1}$ at $GL_{56\ km}$ (Figure 3.2; Tables S3.2 and S3.3). There was a reduction in ER at most monitoring sites along Gallinas Creek, with average values ranging from 0.1 $gO_2\ m^{-2}\ d^{-1}$ at $GMZ_{29\ km}$ to 6.6 $gO_2\ m^{-2}\ d^{-1}$ at $GFT_{22\ km}$. ER increased at $PSR_{170\ km}$, reaching an average of 5.5 $gO_2\ m^{-2}\ d^{-1}$ (Tables 3.1, S3.2, and S3.3). Metabolic fingerprint distributions at monitoring sites upstream of Santa Rosa Lake shifted away from the 1:1 line. The $GMZ_{29\ km}$ distribution moved near the zero-to-zero axis (Figure

3.3B). The distributions from $GFT_{22\ km}$, $GL_{56\ km}$, and $PSR_{170\ km}$ shifted to lower GPP and higher ER magnitudes compared to the pre-monsoon period (Figure 3.3C-D). $PBS_{190\ km}$ was the only site where metabolic fingerprint distributions in the pre-monsoon and monsoon periods overlapped, not including the dam release flow cluster, and its centroid had the same GPP with slightly higher ER, indicating little change between periods (Figure 3.3E).

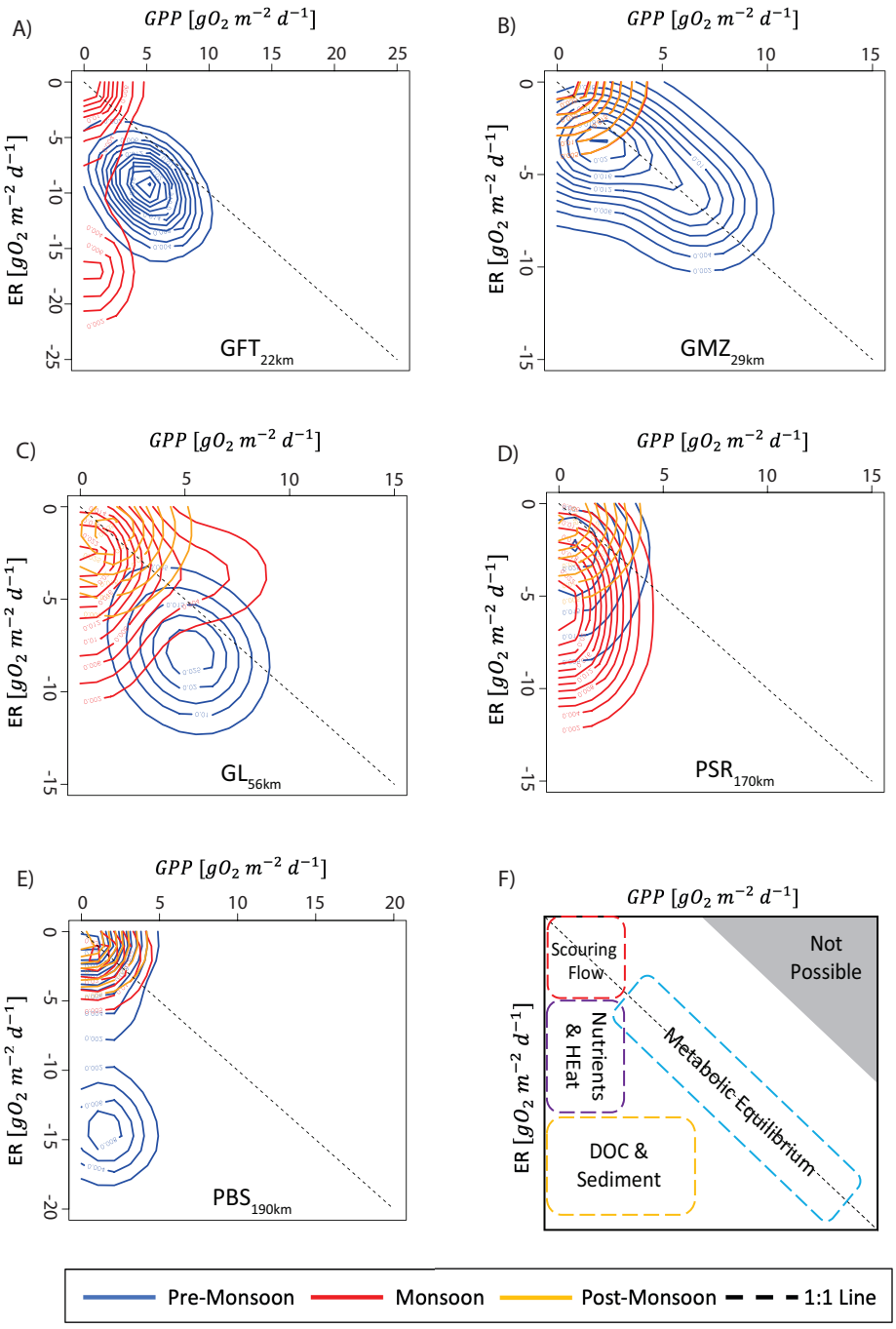

Figure 3.3: Metabolic fingerprints at each monitoring site grouped by their respective temporal period. A) $GFT_{22\ km}$, Gallinas Creek near La Placita fire station, 22 km downstream from the headwaters of Gallinas Creek, B) $GMZ_{29\ km}$, Gallinas Creek near Montezuma, C) $GL_{56\ km}$, Gallinas Creek near Lourdes, D) $PSR_{170\ km}$, Pecos River upstream of Santa Rosa Lake, E) $PBS_{190\ km}$, Pecos River downstream of Santa Rosa Lake, F) Conceptual figure modified from Bernhardt et al. (2018) illustrating where forcing variables change the position of a metabolic distribution.

Between the monsoon and post-monsoon periods, GPP and ER changed at all sites except at $GMZ_{29\ km}$. GPP increased at $GL_{56\ km}$ to an average of 1.9 $gO_2\ m^{-2}\ d^{-1}$. $PSR_{170\ km}$ and $PBS_{190\ km}$ experienced a significant reduction in GPP, averaging 0.1 and 0.3 $gO_2\ m^{-2}\ d^{-1}$, respectively (Table S3.2 and Figure 3.2). ER at $GL_{56\ km}$, $PSR_{170\ km}$, and $PBS_{190\ km}$ had a significant reduction to averages of 1.8, 1.0, and 0.6 $gO_2\ m^{-2}\ d^{-1}$, respectively. There were little changes to the metabolic fingerprint distributions at $GMZ_{29\ km}$, with a centroid near the zero axis. At $GL_{56\ km}$ and $PSR_{170\ km}$, the distributions shifted back to the 1:1 line but stayed lower than in the pre-monsoon period (Figure 3.3). There were minor changes in metabolic clusters at $PBS_{190\ km}$, which overlapped with pre-monsoon and monsoon clusters. Between the pre-monsoon and post-monsoon periods, GPP and ER changed at all sites except at $PBS_{190\ km}$, where ER did not change (Table 3.1).

3.4 Discussion

3.4.1 Pre-Fire vs. Fire Year Differences at the Two Stations ($PSR_{170\ km}$ and $PBS_{190\ km}$) with Comparable Data

With respect to the values observed in 2021, only stage and pH values were significantly different in 2022 at $PSR_{170\ km}$ during the pre-monsoon period. While average stage values were similar (Table S3.2), they were more variable in 2021 (Figures 3.2 and S3.2; Table S3.3). Average pH values were greater in 2021 (i.e., 8.4 vs 8.0). At $PBS_{190\ km}$, only stage values differed and had a greater average in 2022 (i.e., 0.08 vs. 0.2m). All the other parameters and stream metabolism fluxes remained similar (Table 3.1).

During the monsoon period, only stage and ER values were significantly different at $PSR_{170\ km}$. Average stage and ER values were greater in 2022 (i.e., 0.2 vs 0.4 m; 3.1 vs. 5.5 $gO_2\ m^{-2}\ d^{-1}$, respectively) (Tables 3.1, S3.2, and S3.3). At $PBS_{190\ km}$, average stage, GPP, and ER values were greater in 2022 (i.e., 0.02 vs. 0.2 m; 0.4 vs. 0.8 $gO_2\ m^{-2}\ d^{-1}$; and 0.6 vs. 2.8 $gO_2\ m^{-2}\ d^{-1}$, respectively).

During the post-monsoon period, average stage, DO, specific conductivity, pH, GPP, and ER values differed at $PSR_{170\ km}$. Average specific conductivity, pH, GPP, and ER values were greater in 2021 (i.e., 1847 vs. 536 uS/cm; 8.2 vs. 7.8; 0.4 vs. 0.1 $gO_2\ m^{-2}\ d^{-1}$; and 1.5 vs. 1.0 $gO_2\ m^{-2}\ d^{-1}$, respectively) (Tables 3.1, S3.2, and S3.3). Average stage and DO values were greater in 2022 (i.e., 0.1 vs. 0.2 m; 8.5 vs. 10.2 mg/L, respectively). At $PBS_{190\ km}$, average stage, specific conductivity, pH, turbidity, and ER values were different. Average stage, specific conductivity, and turbidity were greater in 2021 (i.e., 0.03 vs. 0.02 m; 2630 vs. 2572 uS/cm; 12.6 vs. 0.2 FNU, respectively). Average pH and ER values were greater in 2022 (i.e., 7.6 vs. 8.0; 0.3 vs. 0.6 $gO_2\ m^{-2}\ d^{-1}$, respectively).

3.4.2 Wildfire Disturbance Generation and Propagation: Impacts to Stream Metabolism and Ecosystem Services

The most significant changes observed in our study occurred during the monsoon period. We identified twelve high-flow events with exceedance probability < 1% at the $GMZ_{29\ km}$ monitoring site (Figure S3.3), coupled with a rapid increase in turbidity from $GFT_{22\ km}$ to $PSR_{170\ km}$ and fDOM from $GFT_{22\ km}$ to $GL_{56\ km}$. Due to the low probability nature of these flows with respect to historical records, they are likely associated with

altered hydrologic processes within the burn scar. Beyond flow increases, turbidity concentrations increased by 25x, 3x, 11x, and 20x at $GFT_{22\ km}$, $GMZ_{29\ km}$, $GL_{56\ km}$, and $PSR_{170\ km}$, respectively, with respect to the pre-monsoon period. Similarly, fDOM values increased by 2x, 3x, and 2x at $GFT_{22\ km}$, $GMZ_{29\ km}$, and $GL_{56\ km}$, respectively. Since fDOM and turbidity are common surrogates for dissolved organic carbon (DOC) and suspended sediment concentrations (SSC), these constituents were also likely elevated during the high-flow monsoonal events (Holliday et al., 2003; Lee et al., 2015). Specific conductivity further validates the increase DOC and SSC with it experiencing an significant decrease during the monsoon period, which indicates a reduction in baseflow and an increase in overland flow would mobilize allochthonous sediments and organics into the fluvial network.

Impacts to stream metabolism: During the monsoon period, $PSR_{170\ km}$ experienced similar increases in turbidity in 2021 and 2022 (Figure 3.2; Tables S3.2 and S3.3). This may suggest seasonal increases unrelated to wildfire disturbances. However, the metabolic fingerprint analysis indicates that during the 2022 monsoon season, the sites upstream of Santa Rosa Lake had high ER and low GPP patterns, and at $PSR_{170\ km}$ the metabolic regime skewed to higher ER values compared to 2021 (Figure S3.5), indicating an increase in DOC, nutrients, and SSC post-fire, which together provide resources for heterotrophic respiration while limiting light availability for phototrophic production (Bernhardt et al., 2018).

Our stream metabolism estimates show significant decreases in GPP during the monsoon period (Table 3.1), with an average reduction of 88%, 93%, 74%, and 45% at $GFT_{22\ km}$, $GMZ_{29\ km}$, $GL_{56\ km}$, and $PSR_{170\ km}$, respectively. Like GPP, ER showed a

significant decrease during the monsoon period at $GFT_{22\ km}$, $GMZ_{29\ km}$, and $GL_{56\ km}$, with an average attenuation of 31%, 98%, and 42%, respectively. However, at $PSR_{170\ km}$, ER experienced a significant increase of 44% during the monsoon period. The reductions in ER and GPP are most likely due to the scouring of autotrophic and heterotrophic communities and biofilms from the benthic zone but are also associated with changes in light penetration due to increased turbidity and greater flow depths (Dodds et al., 2013; Ganju et al., 2020; Solins & Cadenasso, 2022). Our principal component analysis shows strong relationships between discharge, turbidity, and fDOM during the monsoon period and inverse relationships between these variables and GPP and ER (Figure 3.4). Unlike the year of the fire, seasonal clusters at $PSR_{170\ km}$ during 2021 had less separation and a weakened relationship between discharge and turbidity to ER (Figure S3.6).

The weakening of DO diel cycling (see Methods) and its shift in peak diel values from 12:00 pm to 8:00 am validates the reduction in GPP at $GFT_{22\ km}$, $GMZ_{29\ km}$, and $GL_{56\ km}$, indicating that Gallinas Creek went from being biologically driven to being physically driven (Figure S3.7). These results suggest a reduction of phototrophic communities, which would typically increase DO during hours of peak solar radiation around noon. With losses in phototrophic biomass, the primary driver of DO diel cycling became gas solubility, which increases with lower water temperatures. As a result, DO concentrations peaked in the early morning. While many mechanisms can cause the loss of benthic phototrophic communities, our metabolic fingerprint analysis suggests that the loss of phototrophic communities was primarily due to scouring of the benthic zone. This was supported by increases in turbidity, fDOM, and stage values during the monsoon period. Cooccurring with the scouring of the benthic zone and loss of phototrophic

communities, there were distinct DO sags that resulted in short-term hypoxia within the water column. These DO sags can further exacerbate stressed aquatic communities that rely on high concentrations of DO for aerobic respiration.

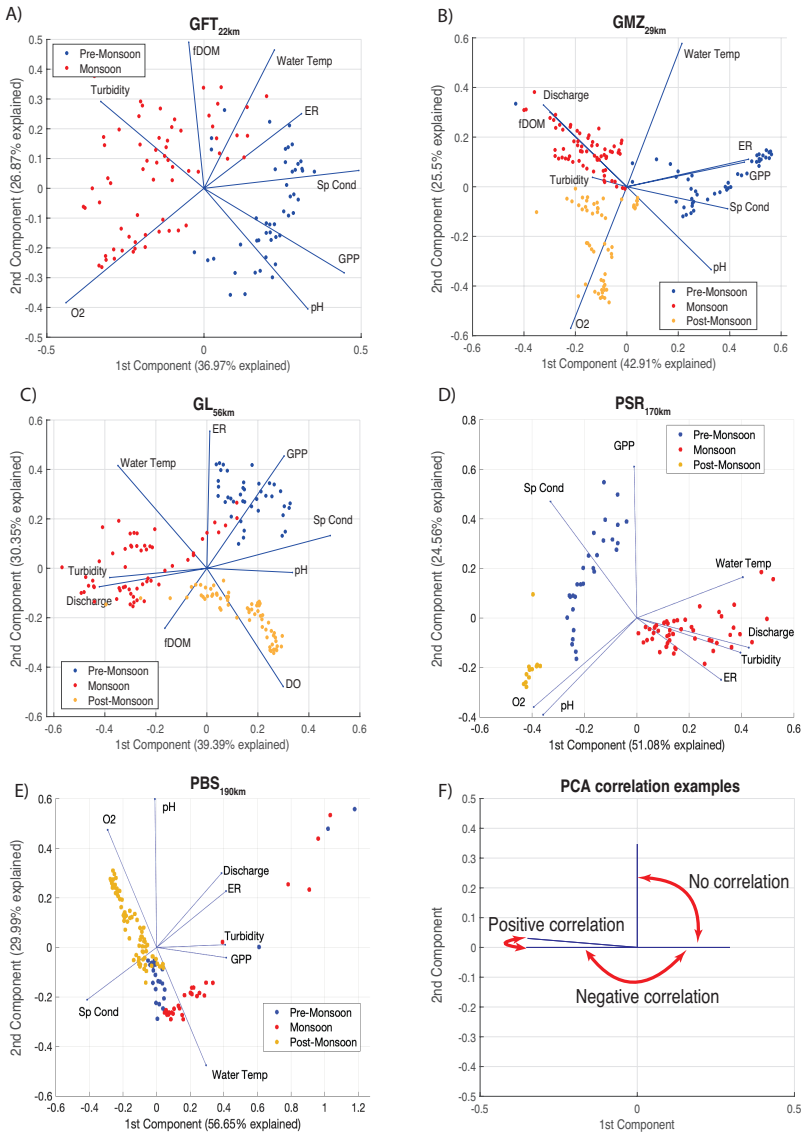

Figure 3.4. PCA biplots with parameter eigen vectors represented by blue lines. A) $GFT_{22\ km}$, Gallinas Creek near La Placita fire station, 22 km downstream from the headwaters of Gallinas Creek, with a total of 64% variability explained; B) $GMZ_{29\ km}$, Gallinas Creek near Montezuma, with a total of 68% variability explained; C) $GL_{56\ km}$, Gallinas Creek near Lourdes, with a total of 70% variability explained; D) $PSR_{170\ km}$, Pecos River upstream of Santa Rosa Lake, with a total of 76% variability explained; E) $PBS_{190\ km}$, Pecos River downstream of Santa Rosa Lake, with a total of 87% variability explained; F) Conceptual figure explaining common positive, negative, and no correlations in PCA biplots.

Impacts to ecosystem services: Besides altering water quality, carbon and nutrient cycling, and stream metabolism fluxes, the propagation of wildfire disturbances affects ecosystem services. For example, increases in turbidity overburdens water purification in water treatment plants, disrupting day-to-day activities in affected locations(Murphy et al., 2023). During the HPCC fire, high turbidity and organics in Gallinas Creek forced the City of Las Vegas, NM, to halt its use as the primary source of potable water. This led to large-scale and restricted use of bottled water in the region and the installation of a 2-million-dollar filtration system at Storrie Lake, a nearby reservoir typically used for irrigation purposes, to be used as a backup water supply. Beyond these impacts, the HPCC wildfire caused soil and sediment management problems due to an increase in overland flow in the watershed, affecting ecosystem services associated with aesthetics, scenic, and recreational uses of the streams and lakes (Figure S3.4).

Post-fire recovery: While $GMZ_{29\ km}$ was still experiencing a reduction in stream metabolism in December 2022, monitoring sites farther downstream of the burn scar started to show signs of recovery in metabolic activity during the post-monsoon period. During that period, sites upstream of Santa Rosa Lake experienced an overall reduction in turbidity and reached values previously experienced during the pre-monsoon season (Table 3.1). Coupled with the shift of metabolic fingerprints from high ER and low GPP to a 1:1 ratio at $GL_{56\ km}$ and $PSR_{170\ km}$ (Figure 3.3), our data suggest metabolic signs of recovery near the end of 2022. However, GPP and ER post-monsoon values were significantly smaller than those observed during the 2021 post-monsoon period (Tables 3.1, S3.2, and S3.3).

Other indications suggest that the fluvial network was still highly susceptible to post-fire precipitation events during the post-monsoon period. For example, on October 23rd, 2022, a 3 mm precipitation event increased discharge to 6.7 m^3/s at $GMZ_{29\ km}$, a flow with an exceedance probability of ~1%, and resulted in the highest turbidity value observed, i.e., 7247 FNU (Table S3.3). Likewise, another precipitation event on October 8th, 2022, produced 5 mm of precipitation and resulted in a 3.76 m^3/s increase in discharge at $GL_{56\ km}$, coinciding with the highest turbidity value measured at that site during the fire year, i.e., 3677 FNU, and a two-day reduction in GPP (Figures S3.2; Table S3.3). These post-monsoon data suggest that while some metabolic fluxes showed signs of recovery, the Gallinas Creek watershed had not fully recovered from the HPCC fire by the end of 2022.

3.4.3 The Role of Santa Rosa Lake in Disturbance Attenuation

The metabolic fingerprints during the 2021 and 2022 monsoon periods at $PSR_{170\ km}$ show distributions with higher ER in 2022. Unlike $PSR_{170\ km}$, the metabolic fingerprints between the two years remain unchanged at $PBS_{190\ km}$. In 2022, most water quality changes were decoupled between $PSR_{170\ km}$ and $PBS_{190\ km}$ (Table 3.1). For example, while only DO and pH did not change at $PSR_{170\ km}$ between the pre-monsoon and monsoon periods, at $PBS_{190\ km}$ DO, specific conductivity, pH, turbidity, GPP, and ER did not change between those two periods.

The decoupling of and differences between water quality parameters and metabolic fluxes observed at $PSR_{170\ km}$ and $PBS_{190\ km}$ (Figures 3.2 and S3.2; Tables 3.1, S3.2, and S3.3) suggest that Santa Rosa Lake buffered wildfire disturbances originating

from the HPCC wildfire burn scar. A separate study from our rapid response research team measured surface water quality longitudinal profiles at Santa Rosa Lake during the monsoon period using an autonomous vehicle (Khandelwal et al., in review) and registered turbidity reductions of up to 650 FNU in the delta of the Pecos River and Santa Rosa Lake, suggesting the existence of hyperpycnal flows, in which the higher density river water sinks below the lower density lake water, effectively mobilizing wildfire disturbance material from the water column into the lake's bed. This deposition and hyperpycnal flow processes help explain why PSB has not shown signals indicating wildfire-related impacts to metabolic processes downstream of the lake and suggests that the lake substantially buffered the longitudinal propagation of wildfire disturbances along the Gallinas Creek-Pecos River continuum.

In Ball et al. (2021), we proposed a simple model to estimate the total longitudinal stream length (SL_{LE}) impacted inside and outside burned watersheds by a disturbance initiating at a stream order ω_0. Briefly, $SL_{LE} = \bar{L}_{\omega_0}(1 - R_L^w)/(1 - R_L)$, where $R_L = \bar{L}(\omega + 1)/\bar{L}(\omega)$ and fluctuates between $1.5<R_L<3.5$, and $\bar{L}(\omega)$ is the arithmetic average of the length of streams of order ω. We applied SL_{LE} to the Las Conchas wildfire dataset presented in Dahm et al. (2015a), which burned first-order streams ($\omega_0 = 1$) with $\bar{L}_1$~1.3 km in Peralta Canyon, to predict that the Rio Grande would still be affected where it was an 8th order stream, assuming the average value recommended of R_L=2. From our data-limited analysis, we proposed that SL_{LE} conservatively should be about equal to the river length impacted within burned areas SL_{BA} (Ball et al., 2021). From the HPCC wildfire dataset, we know that the wildfire disturbances generated in the headwaters of Gallinas Creek (where $\bar{L}_1$~0.6 km) propagated to the 5th order stream Pecos River (ω=5) upstream

of Santa Rosa Lake. Since our data showed that $PSR_{170\ km}$ was affected by the disturbances but $PBS_{190\ km}$ was not affected, we assume SL_{LE} ~180 km. This propagation can be predicted with our SL_{LE} equation when $3.0<R_L3.5$. Smaller R_L values would consistently overestimate the stream order to which the disturbances propagated, highlighting the key role that lakes have in resetting water quality disturbances.

While overestimations of SL_{LE} in watersheds with significant lakes are expected because Horton's original equation predicts the uninterrupted growth of stream orders from headwaters to the ocean, our HPCC fire analysis suggests that such overestimations should be much more common in fluvial networks with lakes that are not bypassed by most flow paths draining the burned area. For example, compared to the dominant role that Santa Rosa Lake had in the longitudinal propagation of wildfire disturbances from the HPCC fire, Cochiti Lake played a less dominant role in resetting water quality after the 2011 Las Chochas Fire (Dahm et al., 2015a). This was because Cochiti Lake only received flow paths draining the east side of the burned Jemez Mountains, but multiple discharge-relevant flow paths draining the west side connected to the Jemez River, a tributary draining into the Rio Grande downstream of Cochiti Lake. Also, water operations (i.e., storage and releases) at those two reservoirs differ significantly, i.e., while Cochiti Dam allows continuous river flow, except during flood control operations, Santa Rosa Lake's gates are closed, except during block releases. Therefore, while our equation to estimate SL_{LE} can be used as a first approximation to conservatively estimate the longitudinal propagation of wildfire disturbances, the role of lakes and similar reservoirs is not captured but may be dominant. In those cases, our Horton-based estimation of SL_{LE} would tend to overestimate the total length of streams and rivers

impacted. Given the lake-specific complexity of the relationships between lake size and the scheduling of water storage, water release, and sediment dredging operations, it is unlikely that a simple term to account for those relevant features can be added to our simplistic SL_{LE} model.

3.5 Conclusions

The HPCC wildfire is currently the largest fire recorded in New Mexico, with a burn scar of 1,382 km^2. The Gallinas Creek watershed was ~ 87% burned and holds the highest population density around the HPCC burn perimeter. About 19% of this watershed had a high severity burn, 25% a moderate severity, and 43% a low severity. From our monitoring of five instrumented sites located along a 198 km network of Gallinas Creek – Pecos River – and Santa Rosa Lake, we observed twelve high-flow events during the monsoon season, with exceedance probabilities smaller than 1%. These unusual high-flow events featured elevated turbidity and fDOM along Gallinas Creek, coupled with reductions in GPP and ER and a shift in metabolic fingerprints, indicating scouring of the benthic zone. The site on the Pecos River upstream of Santa Rosa Lake featured reductions in GPP and increases in ER associated with the propagation of wildfire disturbances, while water quality parameters and stream metabolism at the site downstream of the lake remained largely unchanged. Interestingly, the marked and decoupled differences between the sites upstream and downstream of Santa Rosa Lake suggest that the lake was able to buffer wildfire disturbances over the ten months post-fire included in this study.

This work addresses critical recommendations for incorporating wildfires into the spatiotemporal analysis of water impairment along fluvial networks(Ball et al., 2021). We increased focus on longitudinal behaviors by capturing the propagation of wildfire disturbances over 190 km and incorporated high-frequency data to the monitoring of multiple water quality parameters and fluxes sub-hourly, at multiple sites, from 'first-flush' events to multiple months after the fire was extinguished. This rapid-response and comprehensive research was possible due to the funding investment for preparation and readiness made available by the National Science Foundation before the historic 2022 fire season began.

Acknowledgments

The National Science Foundation funded this work through grants CBET 2054444 and HDR 1914490. The U.S. Army Corps of Engineers supported part of this research through internal funding to JKR and Cooperative Agreement W912HZ-14-2-0014 to DJVH and RGP. However, the findings and conclusions in this article are those of the authors and do not necessarily represent the views of the U.S. Government. The New Mexico Water Resources Research Institute also funded part of this research through faculty and student grants to Ricardo González-Pinzón and Asmita Kaphle. We thank Matthew Segura and Christopher McGibbon from USACE for assisting with the operation and maintenance of the sites above and below Santa Rosa Lake. We thank Lea Knutson and Conrad Greaves from the Hermit's Peak Watershed Alliance for helping us secure site access to monitoring stations; Jennifer Aldred from New Mexico Highlands

University for help setting up sensor stations; and the firefighters who saved lives and property during this devastating event.

Supplemental Information:

Figure S3.1: The burn severity within Gallinas Creek's watershed. Gallinas Creek and Beaver Creek, a perennial tributary to Gallinas Creek, are both highlighted in blue.

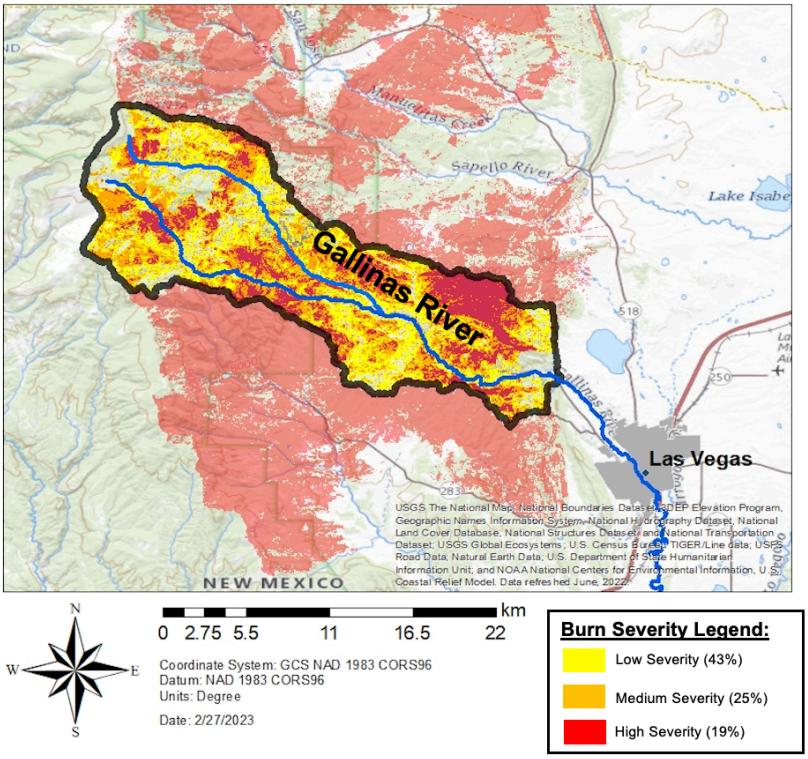

Figure S3.2) Sonde time series of QA/QC data from monitoring sites.
A) $GFT_{22\ km}$ monitoring site

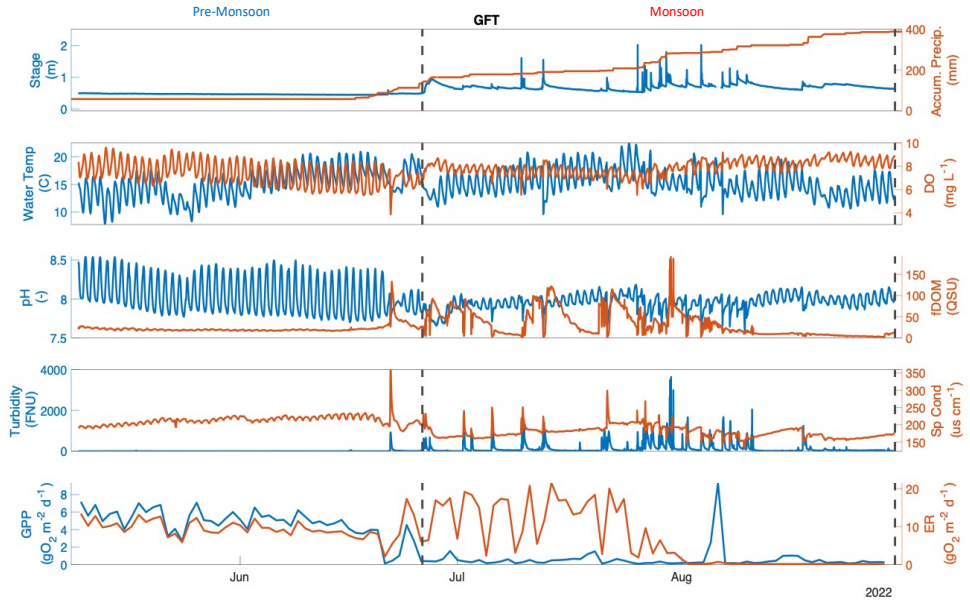

B) $GMZ_{29\ km}$ monitoring site

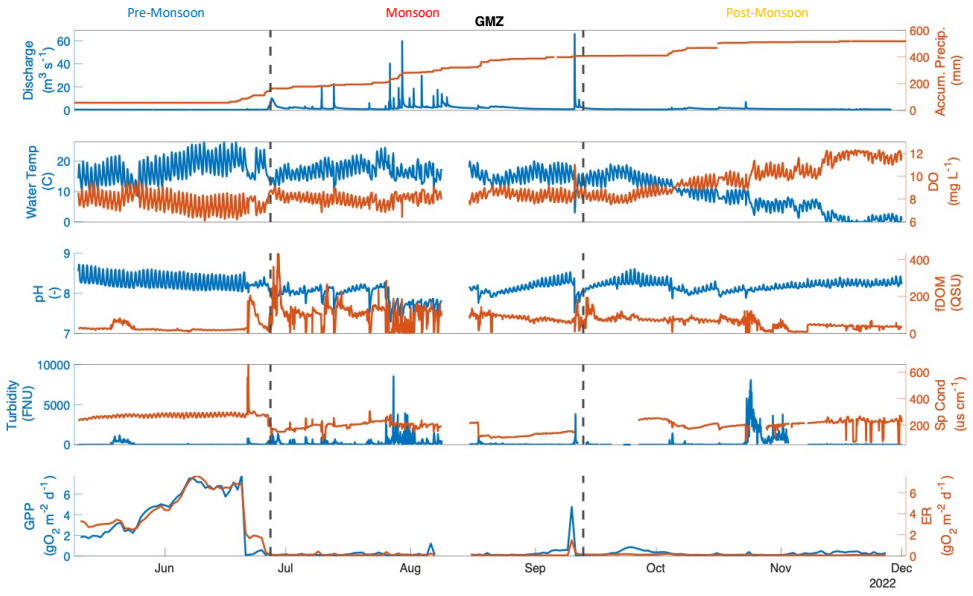

C) $GL_{56\ km}$ monitoring site

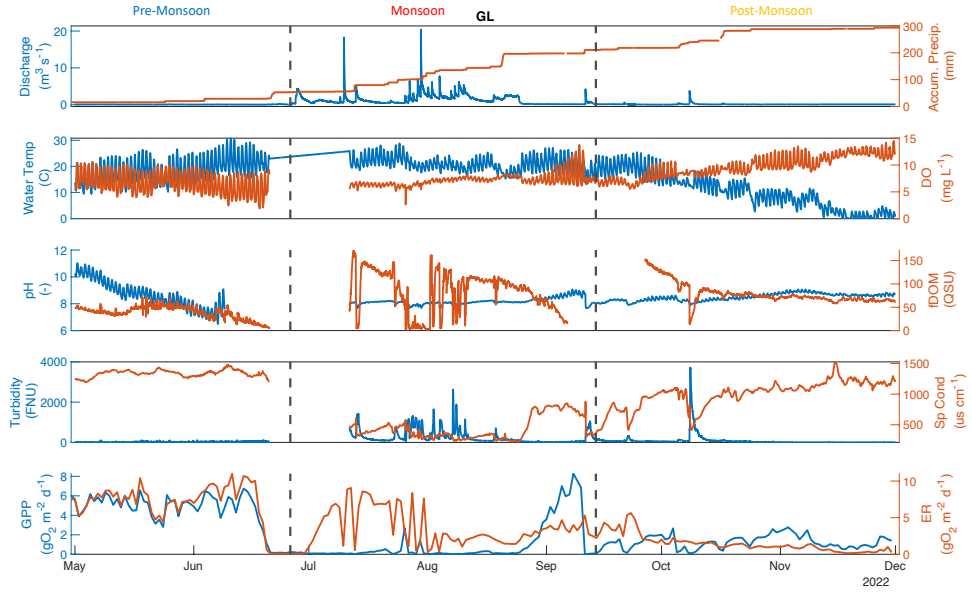

D) $PSR_{170\ km}$ monitoring site during 2022

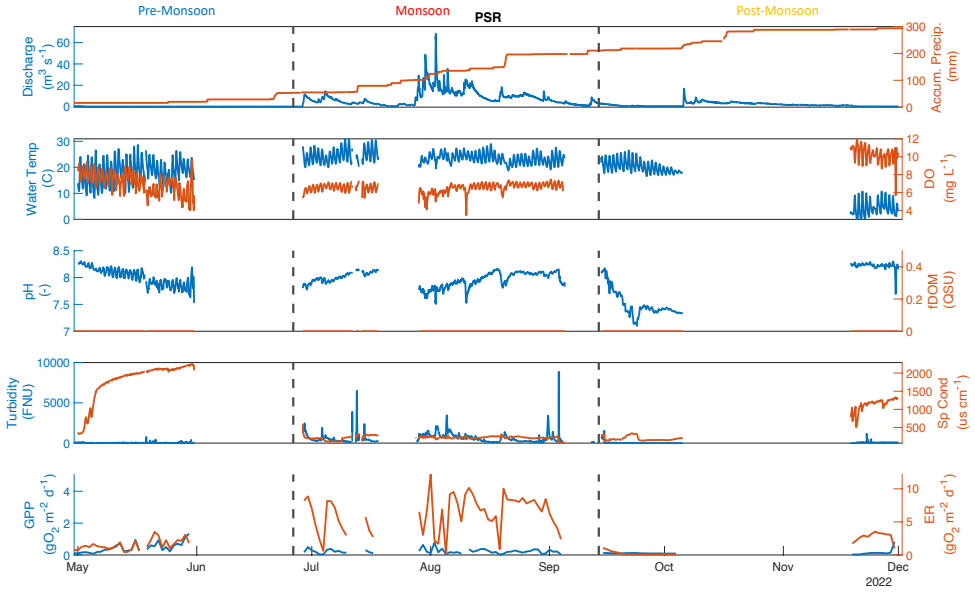

E) $PSR_{170\ km}$ monitoring site during 2021

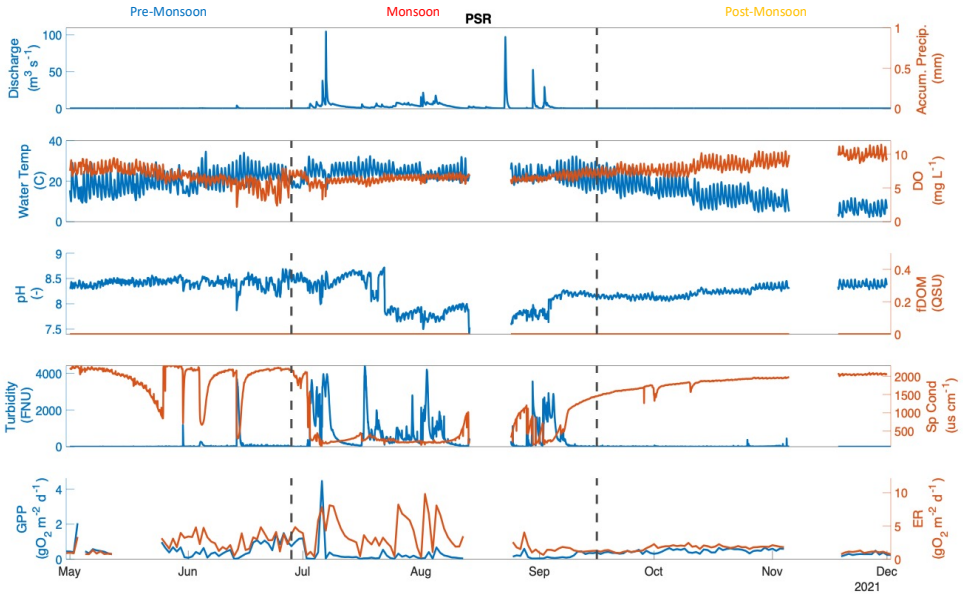

F) $PBS_{190\ km}$ monitoring site during 2022

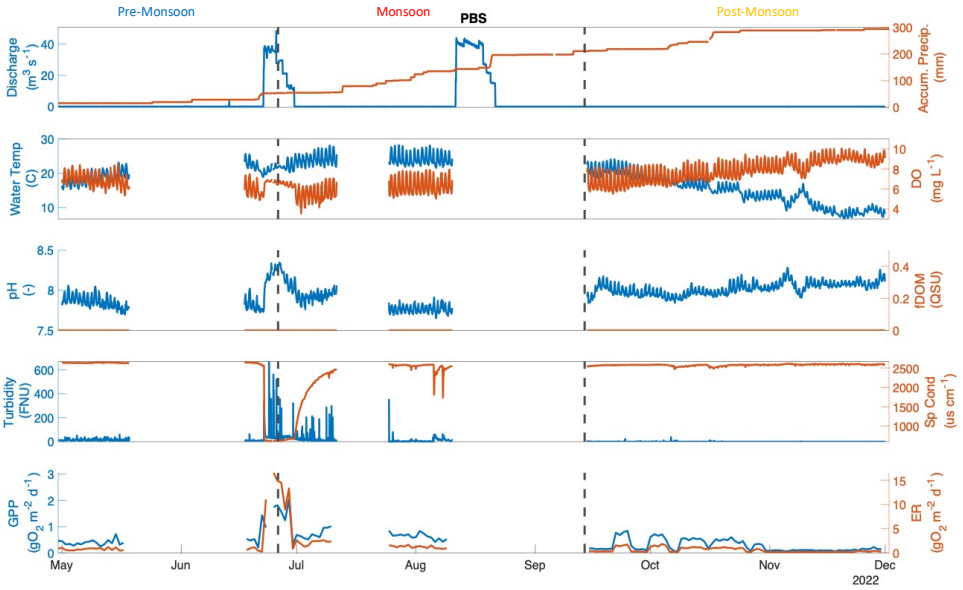

G) $PBS_{190\ km}$ monitoring site during 2021

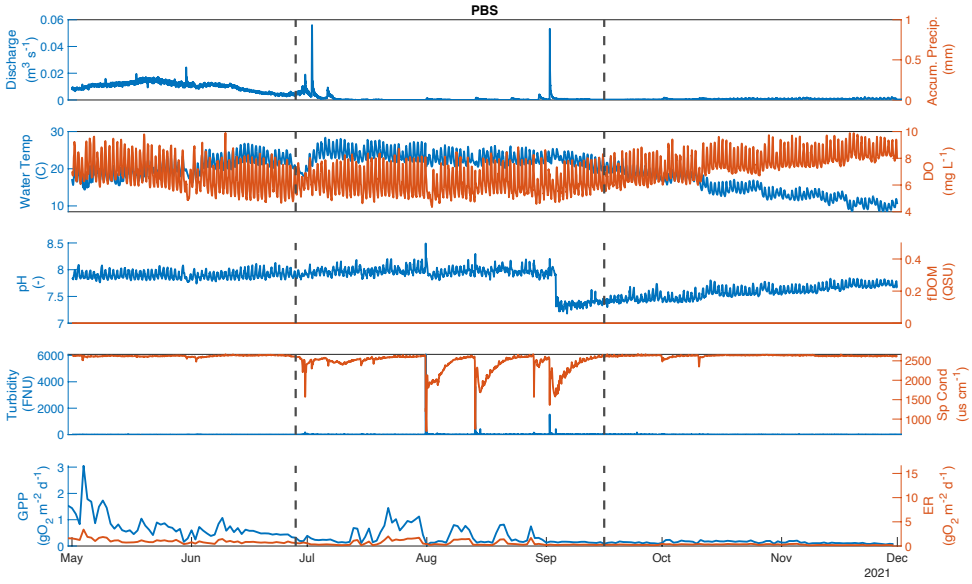

Figure S3.3) Exceedance probability plots at the four USGS stream gages collocated to monitoring sites. The highest four daily discharge events during the study period are annotated.

A) $GMZ_{29\ km}$

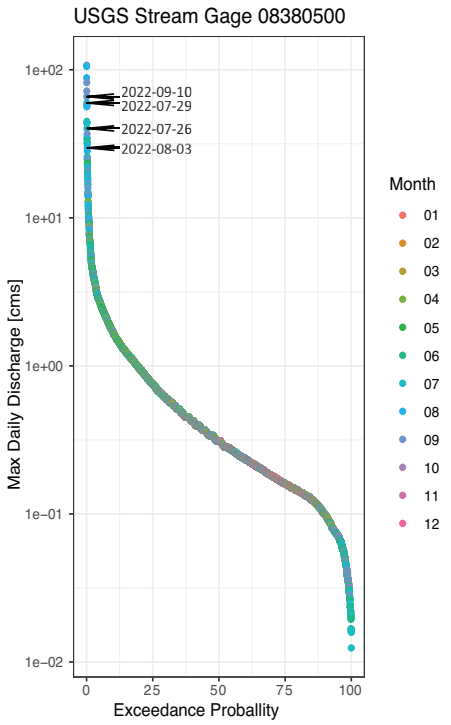

B) $GL_{56\ km}$

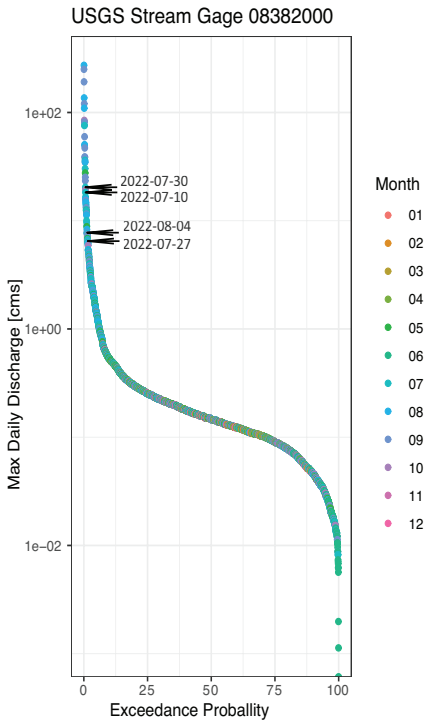

C) $PSR_{170\ km}$

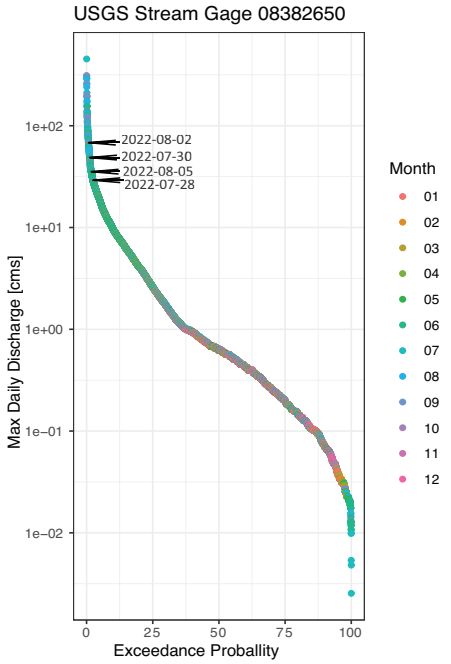

D) $PBS_{190\ km}$

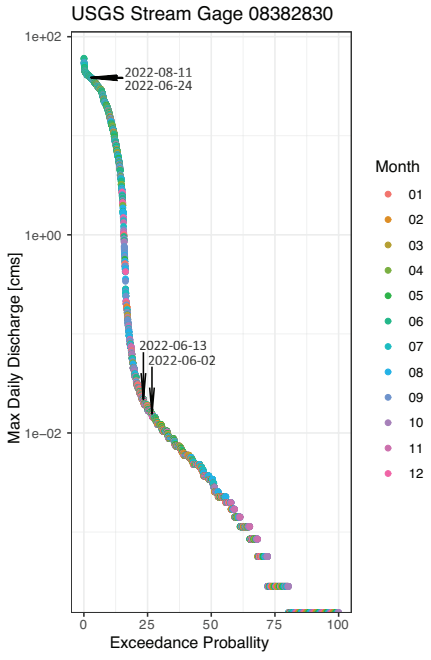

Figure S3.4) Field Photos Taken During Site Maintenance

A) Gabions constructed in the Gallinas River downstream of $GMZ_{29\ km}$. Photo taken: June 29th, 2022

B) Backwatering occurring at gabions with sediment, organics, and woody debris depositing in the surrounding pools. Gallinas River downstream of $GMZ_{29\ km}$. Photo taken: July 20th, 2022

C) Scouring observed in one of the ephemeral tributaries connecting to the Gallinas River upstream of $GMZ_{29\ km}$. Photo taken: July 11th, 2022

D) Overbank flooding observed at $GFT_{22\ km}$. Photo taken: July 11th, 2022

E) Dead aquatic vertebrates observed on the banks of $GFT_{22\ km}$. Photo taken: July 11th, 2022

F) Visible turbid water during the Monsoon period at $GMZ_{29\ km}$. Photo Taken: July 11th, 2022

G) Visible turbid water during the Monsoon period at $GL_{56\ km}$. Photo Taken: July 11th, 2022

Figure S3.5) Metabolic Fingerprints for $PSR_{170\ km}$ and $PBS_{190\ km}$ during 2021.

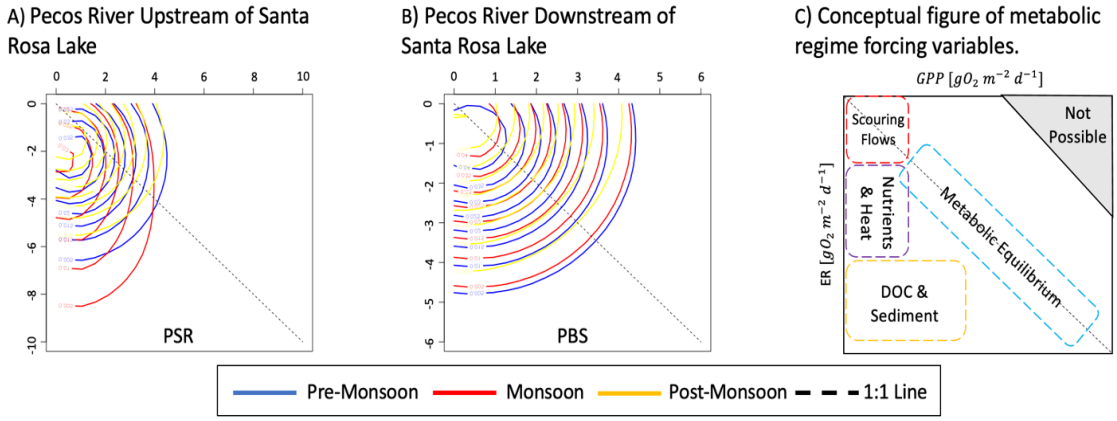

Figure S3.6) PCA biplots for $PSR_{170\ km}$ and $PBS_{190\ km}$ during 2021 study period.

A) Pecos River Upstream of Santa Rosa Lake

B) Pecos River Downstream of Santa Rosa Lake

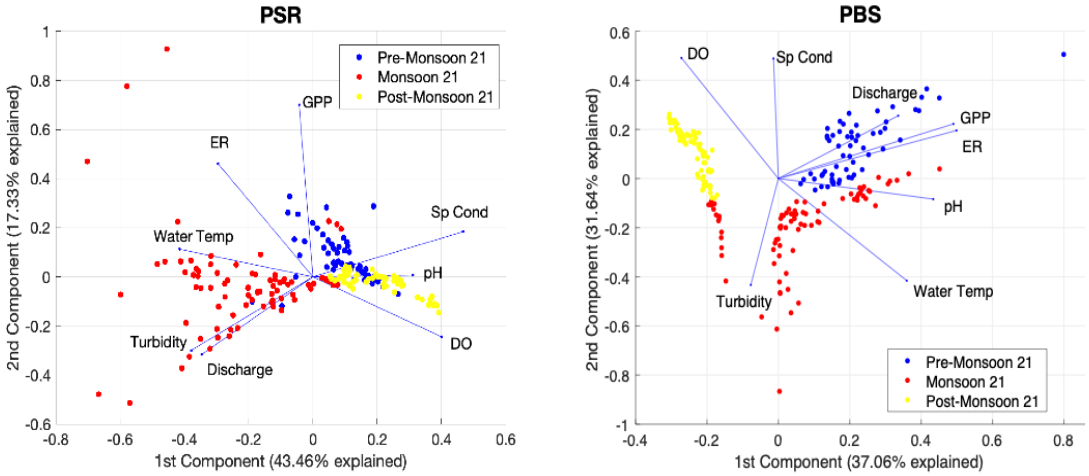

Figure S3.7) Diel spectrograms (top) and diel peak values (bottom) heatmap at each monitoring site. Grey coloring indicates periods of missing data due to sonde damage, burial, or firmware issues. A) $GFT_{22\ km}$, Gallinas Creek near La Placita fire station, 22 km downstream from the headwaters of Gallinas Creek, B) $GMZ_{29\ km}$, Gallinas Creek near Montezuma, C) $GL_{56\ km}$, Gallinas Creek near Lourdes, D) $PSR_{170\ km}$, Pecos River upstream of Santa Rosa Lake, E) $PBS_{190\ km}$, Pecos River downstream of Santa Rosa Lake. F) Conceptual figure generated from GFT data illustrating how spectrograms and peak time of day plots can be utilized to understand changes to diel cycling magnitude and timing.

A)

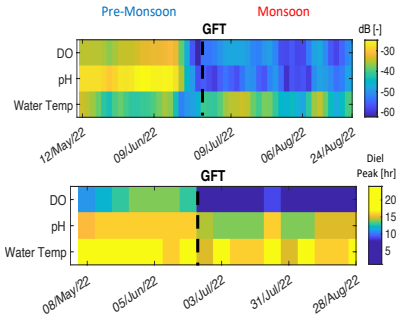

B)

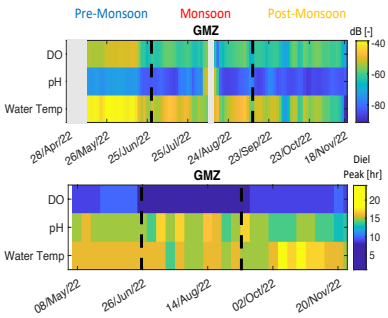

C)

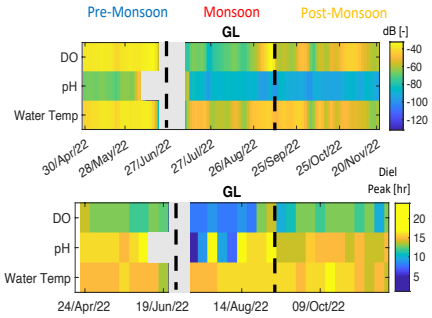

D)

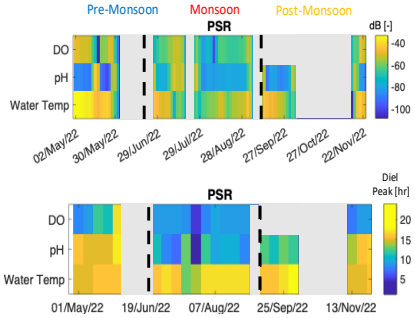

E)

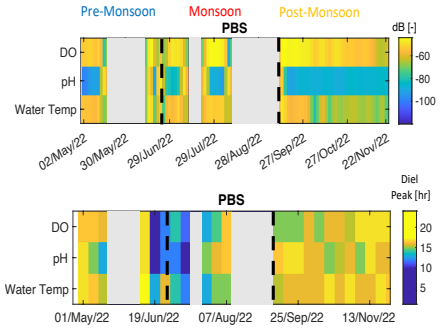

F)

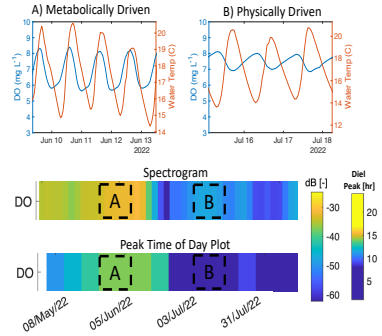

Table S3.1) Parameters, corresponding sensors, and sampling frequencies available during the study.

Source	Parameter	Abbreviation	Units	Sites	Sampling frequency (min)
USGS	Discharge	Discharge	$m^3\ s^{-1}$	$GMZ_{29\ km}$, $GL_{56\ km}$, $PSR_{170\ km}$, $PBS_{190\ km}$	15
	Stage	Stage	m	$GFT_{22\ km}$, $GMZ_{29\ km}$, $GL_{56\ km}$, $PSR_{170\ km}$, $PBS_{190\ km}$	15
YSI EXO2	Dissolved oxygen	DO	ppm	$GFT_{22\ km}$, $GMZ_{29\ km}$, $GL_{56\ km}$, $PSR_{170\ km}$, $PBS_{190\ km}$	15
	Specific conductivity	Sp Cond	$uS\ cm^{-1}$	$GFT_{22\ km}$, $GMZ_{29\ km}$, $GL_{56\ km}$, $PSR_{170\ km}$, $PBS_{190\ km}$	15
	Water temperature	Water Temp	ºC	$GFT_{22\ km}$, $GMZ_{29\ km}$, $GL_{56\ km}$, $PSR_{170\ km}$, $PBS_{190\ km}$	15
	Turbidity	Turbidity	FNU	$GFT_{22\ km}$, $GMZ_{29\ km}$, $GL_{56\ km}$, $PSR_{170\ km}$, $PBS_{190\ km}$	15
	pH	pH	-	$GFT_{22\ km}$, $GMZ_{29\ km}$, $GL_{56\ km}$, $PSR_{170\ km}$, $PBS_{190\ km}$	15
	Fluorescent dissolved organic matter	fDOM	RFU	$GFT_{22\ km}$, $GMZ_{29\ km}$, $GL_{56\ km}$	15
MesoWest	Barometric pressure	Baro Press	mmHg	KLVS	10
	Solar radiation	PAR	$\mu mol\ m^{-2}\ s^{-1}$	LVPN5, TR931, NMC06, NMC08	10
	Precipitation	Precip	mm	LVPN5, TR931 NMC08, NMC06	10

Table S3.2) Temporal period average values by monitoring site. Pre-M, M, and post-M indicate pre-monsoon, monsoon, and post-monsoon.

Site	Season	Discharge (m^3/s)	Stage (m)	DO (mg/L)	Water Temp (C)	fDOM (QSU)	Sp Cond (uS/cm)	pH	Turbidity (FNU)	GPP (gO_2/m^2d)	ER (gO_2/m^2d)
GFT_2 2km	Pre-M	NA	0.5	7.3	15.2	21.7	212.8	8.0	5.9	4.8	9.5
	M	NA	0.7	7.9	15.3	32.9	178.4	8.0	149.0	0.6	6.6
GMZ 29km	Pre-M	0.2	0.2	7.8	17.3	32.8	272.9	8.3	62.7	3.4	4.3
	M	2.0	0.4	8.2	16.2	95.8	171.8	8.0	182.2	0.2	0.1
	Post-M	0.7	0.3	9.9	8.0	58.0	210.4	8.2	259.5	0.3	0.1
GL_{56km}	Pre-M	0.05	0.2	6.7	18.9	38.7	1332.9	8.7	23.8	4.9	7.6
	M	1.3	0.3	7.2	21.6	82.7	442.1	8.2	268.8	1.3	4.4
	Post-M	0.1	0.2	9.6	10.5	79.2	992.4	8.5	85.0	1.9	1.8
PSR_1 70km	Pre-M 21	0.09	0.1	6.7	20.3	NA	1966.9	8.4	53.8	0.6	2.2
	M 21	3.4	0.2	6.1	23.7	NA	501.3	8.0	660.6	0.4	3.1
	Post-M 21	0.06	0.1	8.5	13.1	NA	1847.1	8.2	6.7	0.4	1.5
	Pre-M	0.03	0.1	7.1	18.1	NA	1790.4	8.0	28.5	0.6	3.1
	M	7.9	0.4	6.5	23.8	NA	218.0	8.0	574.1	0.2	5.5
	Post-M	1.8	0.2	10.2	14.4	NA	536.6	7.8	48.4	0.1	1.0
PBS_1 90km	Pre-M 21	0.01	0.08	6.9	20.5	NA	2624.0	7.9	4.0	0.4	0.9
	M 21	0.0007	0.02	6.2	23.1	NA	2427.9	7.9	25.5	0.4	0.6
	Post-M 21	0.0008	0.03	7.7	14.7	NA	2630.2	7.6	12.6	0.1	0.3

Table S3.2) Temporal period average values by monitoring site. Pre-M, M, and post-M indicate pre-monsoon, monsoon, and post-monsoon.

Site	Season	Discharge (m^3/s)	Stage (m)	DO (mg/L)	Water Temp (C)	fDOM (QSU)	Sp Cond (uS/cm)	pH	Turbidity (FNU)	GPP (gO_2/m^2d)	ER (gO_2/m^2d)
	Pre-M	2.8	0.2	6.3	21.3	NA	2088.7	7.9	26.3	0.8	4.2
	M	5.5	0.2	6.1	23.8	NA	2086.5	7.9	16.3	0.8	2.8
	Post-M	0.0003	0.02	7.7	15.9	NA	2572.5	8.0	0.2	0.3	0.6

Table S3.3) Range values by monitoring site. Pre-M, M, and Post-M indicate pre-monsoon, monsoon, and post-monsoon.

Site	Season	Discharge (m^3/s)	Stage (m)	DO (mg/L)	Water Temp (C)	fDOM (QSU)	Sp Cond (uS/cm)	pH	Turbidity (FNU)	GPP (gO_2/m^2d)	ER (gO_2/m^2d)
GFT$_{22km}$	Pre-M min	NA	0.4	3.9	7.7	16.4	180.9	7.7	0.01	0.1	2.1
	Pre-M max	NA	0.5	9.6	20.9	127	369.7	8.5	871	7.7	17.3
	M min	NA	0.5	5.5	9.6	2.2	133.3	7.6	6.0	0.1	0.2
	M max	NA	1.6	9.2	22.5	163	298.6	8.2	2350	9.3	21.5
GMZ$_{29km}$	Pre-M min	0.02	0.1	6.1	8.4	8.3	188.2	8.0	0.01	0.1	0.1
	Pre-M max	3.5	0.5	9.6	26.4	200	669.5	8.7	1100	7.8	7.6
	M min	0.4	0.3	6.4	3.0	1.9	82.4	7.3	3.2	0.1	0.0
	M max	51.1	1.2	11.0	24.5	420	306.5	8.5	4920	4.8	1.5
	Post-M min	0.04	0.1	7.6	-0.1	2.2	69.7	7.9	0.8	0.04	0.1
	Post-M	4.0	0.5	12.3	19.0	166	267.1	8.6	7250	0.9	0.2

Table S3.3) Range values by monitoring site. Pre-M, M, and Post-M indicate pre-monsoon, monsoon, and post-monsoon.

Site	Season	Discharge (m^3/s)	Stage (m)	DO (mg/L)	Water Temp (C)	fDOM (QSU)	Sp Cond (uS/cm)	pH	Turbidity (FNU)	GPP (gO_2/m^2d)	ER (gO_2/m^2d)
	max										
GL_5 6km	Pre-M min	0.01	0.1	1.9	9.5	5.5	1121	6.5	5.8	1.9	4.6
	Pre-M max	0.2	0.2	10.9	30.8	63.0	1483	11.0	72.6	6.8	11.3
	M min	0.1	0.2	2.7	13.2	2.1	222.1	7.6	16.9	0.01	0.4
	M max	18.2	0.6	13.7	28.8	171.5	876.5	9.1	2583	8.7	8.7
	Post-M min	0.01	0.1	5.5	-0.1	14.7	332.7	7.9	2.7	0.1	0.6
	Post-M max	3.5	0.4	14.5	25.4	152.5	1537	9.1	3678	5.8	6.1
PS R_{170} km	Pre-M 21 Min	0.0	0.1	2.2	9.4	NA	291.4	7.9	0.0	0.0	0.5
	Pre-M 21 Max	3.8	0.3	9.4	34.6	NA	2301	8.7	3602	2.1	4.8
	M 21 Min	0.0	0.1	0.1	3.3	NA	80.1	7.0	0.0	0.0	0.3
	M 21 Max	101.1	2.0	10.7	32.4	NA	2116	8.7	4264	5.1	10.1
	Post-M Min 21	0.0	0.1	6.5	2.2	NA	1265	8.1	0.0	0.2	0.7
	Post-M Max 21	0.1	0.1	11.4	29.0	NA	2095	8.5	171	0.7	2.4

Table S3.3) Range values by monitoring site. Pre-M, M, and Post-M indicate pre-monsoon, monsoon, and post-monsoon.

Site	Season	Discharge (m^3/s)	Stage (m)	DO (mg/L)	Water Temp (C)	fDOM (QSU)	Sp Cond (uS/cm)	pH	Turbidity (FNU)	GPP (gO_2/m^2d)	ER (gO_2/m^2d)
	Pre-M min	0.01	0.1	4.0	8.2	NA	323.2	7.5	3.2	0.1	0.4
	Pre-M max	0.5	0.1	9.7	28.6	NA	2246	8.3	231.3	1.3	7.6
	M min	0.02	0.1	3.5	18.8	NA	81.9	7.5	106.6	0.02	0.2
	M max	66.6	1.9	7.5	31.0	NA	592.7	8.2	3465	0.8	12.2
	Post-M min	0.1	0.1	5.7	0.01	NA	119.8	7.1	0.01	0.03	-1.0
	Post-M max	16.6	0.8	12.0	26.5	NA	1327	8.3	972.4	1.5	3.5
PBS$_{190}$ km	Pre-M 21 Min	0.003	0.1	4.7	14.4	NA	2479	7.7	0.0	-1.2	0.4
	Pre-M 21 Max	0.02	0.1	9.9	26.8	NA	2667	8.1	24.9	1.1	1.4
	M 21 Min	0	0.0	4.4	18.0	NA	687.8	7.2	3.7	0.0	0.2
	M 21 Max	0.04	0.1	8.8	28.4	NA	2670	8.5	3225	1.4	2.0
	Post-M 21 Min	0	0	5.6	8.4	NA	2352	7.4	2.6	0.1	0.1
	Post-M 21 Max	0.002	0.05	9.9	23.0	NA	2676	7.8	90.7	0.2	0.5

Table S3.3) Range values by monitoring site. Pre-M, M, and Post-M indicate pre-monsoon, monsoon, and post-monsoon.

Site	Season	Discharge (m^3/s)	Stage (m)	DO (mg/L)	Water Temp (C)	fDOM (QSU)	Sp Cond (uS/cm)	pH	Turbidity (FNU)	GPP (gO_2/m^2d)	ER (gO_2/m^2d)
	Pre-M min	0.01	0.1	4.9	17.5	NA	610.6	7.7	1.8	0.2	0.3
	Pre-M max	38.5	1.2	8.5	25.7	NA	2659	8.3	448.2	1.8	16.2
	M min	0.00	0.03	3.6	20.2	NA	624.7	7.7	0.01	0.3	0.9
	M max	43.3	1.2	7.9	28.2	NA	2597	8.3	348.8	2.0	14.6
	Post-M min	0	0	5.5	7.6	NA	2467	7.8	0.01	0.05	0.1
	Post-M max	0.001	0.04	10.0	24.1	NA	2612	8.3	9.4	0.8	1.9

Table S3.4) Days of missing data due to sonde damage, burial, or firmware issue. Pre-M, M, and post-M indicate pre-monsoon, monsoon, and post-monsoon.

Site	GFT_{22km}			GMZ_{29km}			GL_{56km}		
Season	Pre-M	M	Post-M	Pre-M	M	Post-M	Pre-M	M	Post-M
Days Missing	0	0	NA	15	8	0	6	15	0
Days of Data	48	66	NA	48	70	78	52	64	58
Site	PSR_{170km}			PSR_{170km}			PBS_{190km}		
Year	2021			2022			2021		
Season	Pre-M	M	Post-M	Pre-M	M	Post-M	Pre-M	M	Post-M
Days Missing	0	11	14	27	25	47	0	0	0
Days of Data	59	69	62	29	54	32	59	80	76
Site	PBS_{190km}								
Year	2022								
Season	Pre-M	M	Post-M						
Days Missing	31	48	3						
Days of Data	11	31	64						

References:

Abatzoglou, J. T., & Williams, A. P. (2016). Impact of anthropogenic climate change on wildfire across western US forests. Proceedings of the National Academy of Sciences of the United States of America, 113(42), 11770–11775. https://doi.org/10.1073/pnas.1607171113

Abram, N. J., Gagan, M. K., McCulloch, M. T., Chappell, J., & Hantoro, W. S. (2003). Coral Reef Death during the 1997 Indian Ocean Dipole Linked to Indonesian Wildfires. Science, 301(5635), 952–955. JSTOR.

Adams, M. A. (2013). Mega-fires, tipping points and ecosystem services: Managing forests and woodlands in an uncertain future. Forest Ecology and Management, 294, 250–261. https://doi.org/10.1016/j.foreco.2012.11.039

Allen, C. D., Macalady, A. K., Chenchouni, H., Bachelet, D., McDowell, N., Vennetier, M., Kitzberger, T., Rigling, A., Breshears, D. D., Hogg, E. H. (Ted), Gonzalez, P., Fensham, R., Zhang, Z., Castro, J., Demidova, N., Lim, J.-H., Allard, G., Running, S. W., Semerci, A., & Cobb, N. (2010). A global overview of drought and heat-induced tree mortality reveals emerging climate change risks for forests. Forest Ecology and Management, 259(4), 660–684. https://doi.org/10.1016/j.foreco.2009.09.001

Appling, A. P., Hall, R. O., Yackulic, C. B., & Arroita, M. (2018). Overcoming Equifinality: Leveraging Long Time Series for Stream Metabolism Estimation. Journal of Geophysical Research: Biogeosciences, 123(2), 624–645. https://doi.org/10.1002/2017JG004140

Ball, G., Regier, P., González-Pinzón, R., Reale, J., & Van Horn, D. (2021). Wildfires increasingly impact western US fluvial networks. Nature Communications, 12(1), Article 1. https://doi.org/10.1038/s41467-021-22747-3

Bêche, L. A., Stephens, S. L., & Resh, V. H. (2005). Effects of prescribed fire on a Sierra Nevada (California, USA) stream and its riparian zone. Forest Ecology and Management, 218(1), 37–59. https://doi.org/10.1016/j.foreco.2005.06.010

Bernhardt, E. S., Heffernan, J. B., Grimm, N. B., Stanley, E. H., Harvey, J. W., Arroita, M., Appling, A. P., Cohen, M. J., McDowell, W. H., Hall, R. O., Read, J. S., Roberts, B. J., Stets, E. G., & Yackulic, C. B. (2018). The metabolic regimes of flowing waters. Limnology and Oceanography, 63(S1). https://doi.org/10.1002/lno.10726

Bixby, R. J., Cooper, S. D., Gresswell, R. E., Brown, L. E., Dahm, C. N., & Dwire, K. A. (2015a). Fire effects on aquatic ecosystems: An assessment of the current state of the science. Freshwater Science, 34(4), 1340–1350. https://doi.org/10.1086/684073

Bixby, R. J., Cooper, S. D., Gresswell, R. E., Brown, L. E., Dahm, C. N., & Dwire, K. A. (2015b). Fire effects on aquatic ecosystems: An assessment of the current state of the science. Freshwater Science, 34(4), 1340–1350. https://doi.org/10.1086/684073

Bladon, K. D., Emelko, M. B., Silins, U., & Stone, M. (2014). Wildfire and the Future of Water Supply. Environmental Science & Technology, 48(16), 8936–8943. https://doi.org/10.1021/es500130g

Brauman, K. A., Daily, G. C., Duarte, T. K., & Mooney, H. A. (2007). The Nature and Value of Ecosystem Services: An Overview Highlighting Hydrologic Services. Annual Review of Environment and Resources, 32(1), 67–98. https://doi.org/10.1146/annurev.energy.32.031306.102758

Breshears, D. D., Cobb, N. S., Rich, P. M., Price, K. P., Allen, C. D., Balice, R. G., Romme, W. H., Kastens, J. H., Floyd, M. L., Belnap, J., Anderson, J. J., Myers, O. B., & Meyer, C. W. (2005). Regional vegetation die-off in response to global-change-type drought. Proceedings of the National Academy of Sciences, 102(42), 15144–15148. https://doi.org/10.1073/pnas.0505734102

Burton, C. A., Hoefen, T. M., Plumlee, G. S., Baumberger, K. L., Backlin, A. R., Gallegos, E., & Fisher, R. N. (2016). Trace Elements in Stormflow, Ash, and Burned Soil following the 2009 Station Fire in Southern California. PLoS ONE, 11(5). https://doi.org/10.1371/journal.pone.0153372

Calkin, D. E., Thompson, M. P., & Finney, M. A. (2015). Negative consequences of positive feedbacks in US wildfire management. Forest Ecosystems, 2(1), 9. https://doi.org/10.1186/s40663-015-0033-8

Carr, J., White, A. B., & Thomson, B. (2012). Large-Scale Forest Fires and Resulting Alterations to the Hydrologic Cycle in the Western U.S. AGU Fall Meeting Abstracts, 2012, EP51E-06.

Cayan, D. R., Kammerdiener, S. A., Dettinger, M. D., Caprio, J. M., & Peterson, D. H. (2001). Changes in the Onset of Spring in the Western United States. Bulletin of the American Meteorological Society, 82(3), 399–416. https://doi.org/10.1175/1520-0477(2001)082<0399:CITOOS>2.3.CO;2

Cerrato, J. M., Blake, J. M., Hirani, C., Clark, A. L., Ali, A.-M. S., Artyushkova, K., Peterson, E., & Bixby, R. J. (2016). Wildfires and water chemistry: Effect of metals associated with wood ash. Environ. Sci.: Processes Impacts, 18(8), Article 8. https://doi.org/10.1039/C6EM00123H

Dahm, C. N., Candelaria-Ley, R. I., Reale, C. S., Reale, J. K., & Van Horn, D. J. (2015a). Extreme water quality degradation following a catastrophic forest fire. Freshwater Biology, 60(12), 2584–2599. https://doi.org/10.1111/fwb.12548

Dahm, C. N., Candelaria-Ley, R. I., Reale, C. S., Reale, J. K., & Van Horn, D. J. (2015b). Extreme water quality degradation following a catastrophic forest fire. Freshwater Biology, 60(12), 2584–2599. https://doi.org/10.1111/fwb.12548

Dodds, W. K., Veach, A. M., Ruffing, C. M., Larson, D. M., Fischer, J. L., & Costigan, K. H. (2013). Abiotic controls and temporal variability of river metabolism: Multiyear analyses of Mississippi and Chattahoochee River data. Freshwater Science, 32(4), 1073–1087.

Downing, B. D., Pellerin, B. A., Bergamaschi, B. A., Saraceno, J. F., & Kraus, T. E. C. (2012). Seeing the light: The effects of particles, dissolved materials, and temperature on in situ measurements of DOM fluorescence in rivers and streams: Effects and compensation for in situ DOM fluorescence. Limnology and Oceanography: Methods, 10(10), 767–775. https://doi.org/10.4319/lom.2012.10.767

Earl, S. R., & Blinn, D. W. (2003). Effects of wildfire ash on water chemistry and biota in South-Western U.S.A. streams. Freshwater Biology, 48(6), 1015–1030. https://doi.org/10.1046/j.1365-2427.2003.01066.x

Emmerton, C. A., Cooke, C. A., Hustins, S., Silins, U., Emelko, M. B., Lewis, T., Kruk, M. K., Taube, N., Zhu, D., Jackson, B., Stone, M., Kerr, J. G., & Orwin, J. F. (2020). Severe western Canadian wildfire affects water quality even at large basin scales. Water Research, 183, 116071. https://doi.org/10.1016/j.watres.2020.116071

Flannigan, M. D., Krawchuk, M. A., Groot, W. J. de, Wotton, B. M., & Gowman, L. M. (2009). Implications of changing climate for global wildland fire. International Journal of Wildland Fire, 18(5), 483–507. https://doi.org/10.1071/WF08187

Gallaher, B. M., & Koch, R. J. (2004). Cerro Grande Fire Impact to Water Quality and Stream Flow near Los Alamos National Laboratory: Results of Four Years of Monitoring (LA-14177). Los Alamos National Lab., Los Alamos, NM (US). https://doi.org/10.2172/835908

Ganju, N. K., Testa, J. M., Suttles, S. E., & Aretxabaleta, A. L. (2020). Spatiotemporal variability of light attenuation and net ecosystem metabolism in a back-barrier estuary. Ocean Science, 16(3), 593–614.

Holliday, C., Rasmussen, T. C., & Miller, W. P. (2003). Establishing the relationship between turbidity and total suspended sediment concentration.

Huey, G. M., & Meyer, M. L. (2010). Turbidity as an Indicator of Water Quality in Diverse Watersheds of the Upper Pecos River Basin. Water, 2(2), 273–284. https://doi.org/10.3390/w2020273

Jolliffe, I. T., & Cadima, J. (2016). Principal component analysis: A review and recent developments. Philosophical Transactions of the Royal Society A: Mathematical,

Physical and Engineering Sciences, 374(2065), 20150202. https://doi.org/10.1098/rsta.2015.0202

Killick, R., Fearnhead, P., & Eckley, I. A. (2012). Optimal detection of changepoints with a linear computational cost. Journal of the American Statistical Association, 107(500), 1590–1598.

Lee, E.-J., Yoo, G.-Y., Jeong, Y., Kim, K.-U., Park, J.-H., & Oh, N.-H. (2015). Comparison of UV–VIS and FDOM sensors for in situ monitoring of stream DOC concentrations. Biogeosciences, 12(10), 3109–3118. https://doi.org/10.5194/bg-12-3109-2015

Leemans, R. (2009). The Millennium Ecosystem Assessment: Securing Interactions between Ecosystems, Ecosystem Services and Human Well-being. Hexagon Series on Human and Environmental Security and Peace, 53–61. https://doi.org/10.1007/978-3-540-68488-6_3

Mast, M. A., Murphy, S. F., Clow, D. W., Penn, C. A., & Sexstone, G. A. (2016). Water-quality response to a high-elevation wildfire in the Colorado Front Range. Hydrological Processes, 30(12), 1811–1823. https://doi.org/10.1002/hyp.10755

Meek, D., Hatfield, J., Howell, T., Idso, S., & Reginato, R. (1984). A generalized relationship between photosynthetically active radiation and solar radiation 1. Agronomy Journal, 76(6), 939–945.

MesoWest. (2022). New Mexico Climate Stations. https://mesowest.utah.edu/cgi-bin/droman/mesomap.cgi?state=NM&rawsflag=3

Moore, S., Blann, K., Kendy, E., Turner, D., Galloway, D., Gronewold, R., Harris, A., Hickey, J., Pinson, A., Price, D., Reale, J., Ross, G., Ryan, S., Shafike, N.,

Donnelly, C., Llewellyn, D., Young, R., Horner, M., Ryan, V., & Sandbom, K. (2022). Identifying environmental flow requirements for the Pecos River: Background literature review and summary.

Murphy, S. F., Alpers, C. N., Anderson, C. W., Banta, J. R., Blake, J. M., Carpenter, K. D., Clark, G. D., Clow, D. W., Hempel, L. A., Martin, D. A., Meador, M. R., Mendez, G. O., Mueller-Solger, A. B., Stewart, M. A., Payne, S. E., Peterman, C. L., & Ebel, B. A. (2023). A call for strategic water-quality monitoring to advance assessment and prediction of wildfire impacts on water supplies. Frontiers in Water, 5, 1144225. https://doi.org/10.3389/frwa.2023.1144225

Neary, D. G., Gottfried, G. J., & Ffolliott, P. F. (2016). Post-wildfire watershed flood responses.

Nichols, J., Khandelwal, A. S., Regier, P., Summers, B., Van Horn, D. J., & González-Pinzón, R. (2022). The understudied winter: Evidence of how precipitation differences affect stream metabolism in a headwater. Frontiers in Water, 4, 1003159. https://doi.org/10.3389/frwa.2022.1003159

Nimick, D. A., Gammons, C. H., & Parker, S. R. (2011). Diel biogeochemical processes and their effect on the aqueous chemistry of streams: A review. Chemical Geology, 283(1–2), 3–17. https://doi.org/10.1016/j.chemgeo.2010.08.017

North, M. P., Stephens, S. L., Collins, B. M., Agee, J. K., Aplet, G., Franklin, J. F., & Fulé, P. Z. (2015). Reform forest fire management. Science, 349(6254), 1280–1281. https://doi.org/10.1126/science.aab2356

Odum, H. T. (1956). Primary production in flowing waters 1. Limnology and Oceanography, 1(2), 102–117.

Proctor, C. R., Lee, J., Yu, D., Shah, A. D., & Whelton, A. J. (2020). Wildfire caused widespread drinking water distribution network contamination. AWWA Water Science, 2(4), e1183. https://doi.org/10.1002/aws2.1183

Raffa, K. F., Aukema, B. H., Bentz, B. J., Carroll, A. L., Hicke, J. A., Turner, M. G., & Romme, W. H. (2008). Cross-scale Drivers of Natural Disturbances Prone to Anthropogenic Amplification: The Dynamics of Bark Beetle Eruptions. BioScience, 58(6), 501–517. https://doi.org/10.1641/B580607

Reale, J. K., Van Horn, D. J., Condon, K. E., & Dahm, C. N. (2015). The effects of catastrophic wildfire on water quality along a river continuum. Freshwater Science, 34(4), 1426–1442. https://doi.org/10.1086/684001

Regier, P. J., González-Pinzón, R., Van Horn, D. J., Reale, J. K., Nichols, J., & Khandewal, A. (2020). Water quality impacts of urban and non-urban arid-land runoff on the Rio Grande. Science of The Total Environment, 729, 138443.

Reidmiller, D. R., Avery, C. W., Easterling, D. R., Kunkel, K. E., Lewis, K. L., Maycock, T. K., & Stewart, B. C. (2017). Impacts, risks, and adaptation in the United States: Fourth national climate assessment, volume II.

Rhoades, C. C., Chow, A. T., Covino, T. P., Fegel, T. S., Pierson, D. N., & Rhea, A. E. (2018). The Legacy of a Severe Wildfire on Stream Nitrogen and Carbon in Headwater Catchments. Ecosystems. https://doi.org/10.1007/s10021-018-0293-6

Rhoades, C. C., Nunes, J. P., Silins, U., & Doerr, S. H. (2019). The influence of wildfire on water quality and watershed processes: New insights and remaining challenges. International Journal of Wildland Fire, 28(10), 721. https://doi.org/10.1071/WFv28n10_FO

Robinne, F.-N., Hallema, D. W., Bladon, K. D., & Buttle, J. M. (2020). Wildfire impacts on hydrologic ecosystem services in North American high-latitude forests: A scoping review. Journal of Hydrology, 581, 124360. https://doi.org/10.1016/j.jhydrol.2019.124360

Running, S. W. (2006). Is Global Warming Causing More, Larger Wildfires? Science, 313(5789), 927–928. https://doi.org/10.1126/science.1130370

Rust, A. J., Saxe, S., McCray, J., Rhoades, C. C., & Hogue, T. S. (2019). Evaluating the factors responsible for post-fire water quality response in forests of the western USA. International Journal of Wildland Fire, 28(10), 769–784. https://doi.org/10.1071/WF18191

Seager, R., Ting, M., Held, I., Kushnir, Y., Lu, J., Vecchi, G., Huang, H.-P., Harnik, N., Leetmaa, A., Lau, N.-C., Li, C., Velez, J., & Naik, N. (2007). Model Projections of an Imminent Transition to a More Arid Climate in Southwestern North America. Science, 316(5828), 1181–1184. https://doi.org/10.1126/science.1139601

Sherson, L. R., Horn, D. J. V., Gomez-Velez, J. D., Crossey, L. J., & Dahm, C. N. (2015). Nutrient dynamics in an alpine headwater stream: Use of continuous water quality sensors to examine responses to wildfire and precipitation events. Hydrological Processes, 29(14), 3193–3207. https://doi.org/10.1002/hyp.10426

Solins, J. P., & Cadenasso, M. L. (2022). Urban runoff and stream channel incision interact to influence riparian soils and understory vegetation. Ecological Applications, 32(4), e2556.

Spencer, R. G. M., Pellerin, B. A., Bergamaschi, B. A., Downing, B. D., Kraus, T. E. C., Smart, D. R., Dahlgren, R. A., & Hernes, P. J. (2007). Diurnal variability in riverine dissolved organic matter composition determined byin situ optical measurement in the San Joaquin River (California, USA). Hydrological Processes, 21(23), 3181–3189. https://doi.org/10.1002/hyp.6887

Stewart, I. T., Cayan, D. R., & Dettinger, M. D. (2004). Changes in Snowmelt Runoff Timing in Western North America under a `Business as Usual' Climate Change Scenario. Climatic Change, 62(1), 217–232. https://doi.org/10.1023/B:CLIM.0000013702.22656.e8

U.S. Geological Survey. (2022). National Water Information System Data Available on the World Wide Web (USGS Water Data for the Nation). https://waterdata.usgs.gov/nwis

USBOR, & NMISC. (2021). Pecos River Basin Study—New Mexico.

Venables, W., & Ripley, B. D. (2002). Statistics and computing: Modern applied statistics with S. Springer-Verlag, New York Inc, New York. Https://Doi. Org/10, 1007, 978–0.

Wagner, R. J., Boulger Jr., R. W., Oblinger, C. J., & Smith, B. A. (2006). Guidelines and standard procedures for continuous water-quality monitors: Station operation, record computation, and data reporting (Report No. 1-D3; Version 1.0, Techniques and Methods). USGS Publications Warehouse. https://doi.org/10.3133/tm1D3

Weed, A. S., Ayres, M. P., & Hicke, J. A. (2013). Consequences of climate change for biotic disturbances in North American forests. Ecological Monographs, 83(4), 441–470. https://doi.org/10.1890/13-0160.1

Westerling, A. L. (2016). Increasing western US forest wildfire activity: Sensitivity to changes in the timing of spring. Phil. Trans. R. Soc. B, 371(1696), 20150178. https://doi.org/10.1098/rstb.2015.0178

Westerling, A. L., Bryant, B. P., Preisler, H. K., Holmes, T. P., Hidalgo, H. G., Das, T., & Shrestha, S. R. (2011). Climate change and growth scenarios for California wildfire. Climatic Change, 109(1), 445–463. https://doi.org/10.1007/s10584-011-0329-9

Westerling, A. L., Hidalgo, H. G., Cayan, D. R., & Swetnam, T. W. (2006). Warming and Earlier Spring Increase Western U.S. Forest Wildfire Activity. Science, 313(5789), 940–943. https://doi.org/10.1126/science.1128834

Wickham, H., & Grolemund, G. (2016). R for data science: Import, tidy, transform, visualize, and model data. O'Reilly Media, Inc.

Williams, A. P., Allen, C. D., Millar, C. I., Swetnam, T. W., Michaelsen, J., Still, C. J., & Leavitt, S. W. (2010). Forest responses to increasing aridity and warmth in the southwestern United States. Proceedings of the National Academy of Sciences, 107(50), 21289–21294. https://doi.org/10.1073/pnas.0914211107

Yu, M., Bishop, T. F. A., & Van Ogtrop, F. F. (2019). Assessment of the Decadal Impact of Wildfire on Water Quality in Forested Catchments. Water, 11(3), Article 3. https://doi.org/10.3390/w11030533

Chapter 4: Leveraging Artificial Intelligence to Estimate Nitrate Uptake in Stream Reaches of Contrasting Biogeochemistry

Justin Nichols[1], Aashish Sanjay Khandelwal[1], Peter Regier[1,2], David J. Van Horn[3], Alex Tartakovsky[4], Ricardo González-Pinzón[1]

[1]Department of Civil, Construction and Environmental Engineering, University of New Mexico, Albuquerque, New Mexico, USA, [2]Marine and Coastal Research Laboratory, Pacific Northwest National Laboratory, Sequim, Washington, USA, [3]Department of Biology, University of New Mexico, Albuquerque, New Mexico, USA, [4]Department of Civil and Environmental Engineering, University of Illinois at Urbana-Champaign, Urbana, IL, USA

Corresponding authors: Justin Nichols justin67@unm.edu and Ricardo González-Pinzón gonzaric@unm.edu

For submission to Journal of Hydrology

4.1 Introduction

Anthropogenically sourced nutrients remain a significant water quality concern in fluvial systems across the globe, with excess levels leading to eutrophication, harmful algae blooms (HABs), health concerns from discrete and long-term exposure, and impaired ecosystem services (Lintern et al., 2020; Mulholland et al., 2008; Smith et al., 2006). A 2010 study conducted by the U.S. Geological Survey estimated that excess nutrients impaired 90% of the 190 shallow aquifers that connect to fluvial systems (Burow et al., 2010). With the increasing evidence of nutrient pollution in fluvial systems, there has been a surge in research on fluvial nutrient processing and transport (Ensign & Doyle, 2006; Heathwaite, 2010; Pellerin et al., 2016). One of the primary nutrient species of concern and focus is nitrate due to its use as a fertilizer in industrial agriculture, leading to impairment with nitrogen-related eutrophication estimated to cost the U.S. 45–165 billion dollars a year in environmental service degradation and contamination of surface drinking water (Sobota et al., 2015).

While there has been extensive research on understanding spatial and temporal drivers of nitrate transport and uptake within fluvial systems, there have been limited studies on the use of high-frequency water quality and atmospheric parameters as surrogates to estimate transport processes. Researching possible high-frequency surrogates is vital because the current methodology of measuring nitrate transport processes is logistically and finically burdensome (Covino et al., 2010; Ensign & Doyle, 2006; Newbold et al., 1981). The burden in performing such research comes from requiring multiple trained personnel to add known masses of a conservative tracer and nitrate to a study stream reach and collect multiple grab samples downstream to have

their conservative and nitrate concentrations measured in a lab (Workshop, 1990). Not only does performing such an experiment have a high logistical and financial cost (Figure S4.1), but it will only provide insight into a single moment in time and will not be informative of seasonal trends or hot moments of elevated nitrate uptake (Kirchner et al., 2004; Zhao et al., 2021). By estimating nitrate uptake through the use of high-frequency surrogates one can increase the temporal and spatial resolution of nitrate uptake and further help scientists understand primary mechanisms of uptake and inform policymakers of best practices to reduce nitrate contamination within surface waters (Lintern et al., 2020; Neal et al., 2008; Rode et al., 2016).

To the best of our knowledge, there has not been a study that tries to utilize high-frequency parameters as predictors to nitrate uptake rate. However, there have been studies that utilize traditional regression techniques, such as multivariate linear regression, to estimate solute concentrations with high-frequency parameters (Miller et al., 2007; Morel et al., 2020). One of the major limitations of such an approach is that it requires feature engineering of the high-frequency parameters to match the temporal resolution of the measured uptake rates to be able to perform one-to-one regression (Maulud & Abdulazeez, 2020; Raghavendra & Deka, 2014). Feature engineering often results in the aggregation, and thus the oversimplification, of the high-frequency datasets which often reduces temporal variances and cyclical patterns, or it requires extensive domain knowledge of the study reach to identify key predictive features, which due to watershed spatial heterogeneity and non-stationarity, often results in a site-specific model that requires routine adjustment (Blöschl & Sivapalan, 1995; McDonnell et al., 2007; Zheng & Casari, 2018). To move past extensive feature engineering and leverage the

temporal complexity inherent with high-frequency parameters, we propose using recurrent neural network (RNN) with high-frequency parameters to be used as model predictors in sequence-to-one regression to estimate nitrate uptake rate (Gao et al., 2020; Shen, 2018; Xu & Liang, 2021) (Figure 4.1).

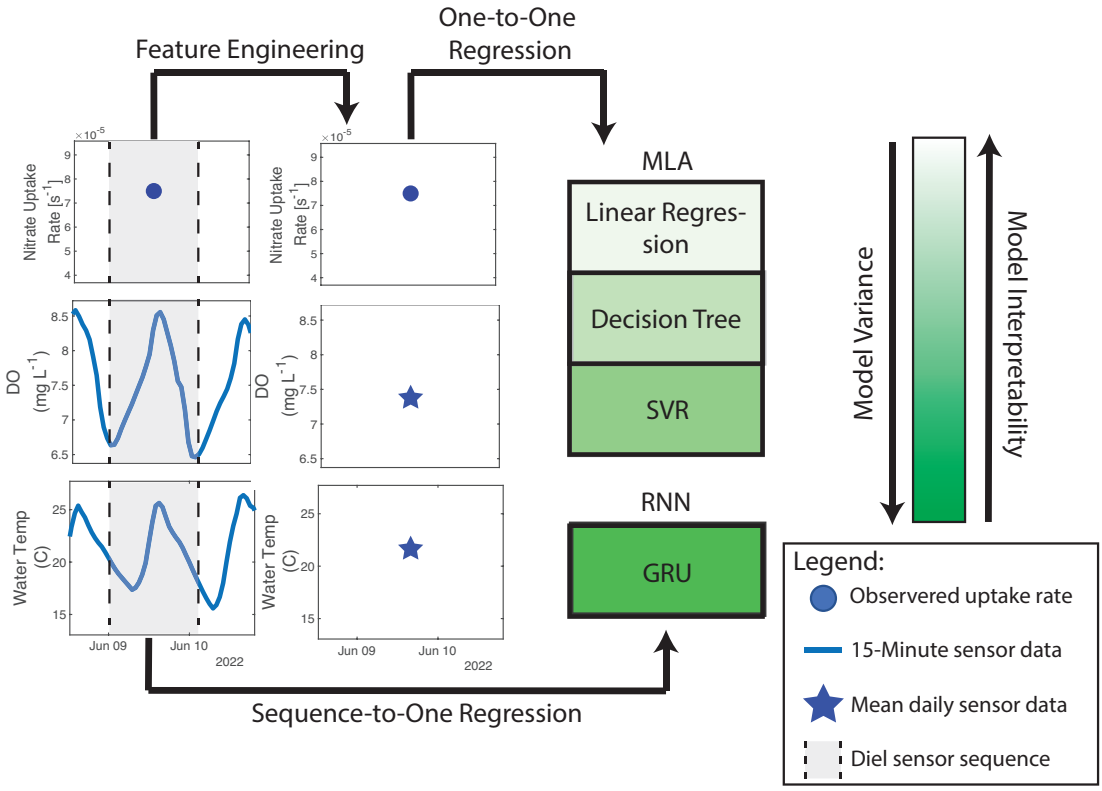

Figure 4.1: Conceptual diagram of one-to-one regression workflow vs sequence-to-one regression with varying model architectures of varying model variance. Traditional machine learning algorithms (MLA) rely on one-to-one regression, while recurrent neural networks (RNN) can perform sequence-to-one regression using high-frequency data as predictors. SVR stands for a support vector machine and GRU is a gated recurrent unit. All algorithms are performing regression analysis on continuous data.

This study aims to compare tradition regression techniques that require timeseries aggregation to perform one-to-one regression with recurrent neural network that is capable of sequence-to-one regression to estimate nitrate uptake rate within two study

reaches of contrasting geomorphology, terrestrial ecosystems, and land use. The research questions of this study are:

1. Will recurrent neural networks be able to leverage high-frequency data to improve uptake rate estimates compared to traditional one-to-one regression architectures?
2. Does increasing the number of high-frequency sensors, thus increasing the number of predictors but increasing the associated data cost, improve model accuracy?

4.2 Methods

4.2.1 Site Description

Both research sites were located within the snowmelt dominated Jemez Mountain watershed, which is located in north-central New Mexico. The most upstream research site was in the third order reach of the East Fork Jemez River (referred to as EFJR site from here on), within the Valles Caldera Hidden Valley Elk Enclosure (35.8409N, -106.5013W), and is located approximately 8 km downstream of its headwaters (Figure 4.2). The EFJR site has an average annual discharge of 100 L/s and is a low gradient, meandering and open canopy stream as it has an average channel slope of 0.57%, and non-woody riparian vegetation (Sherson et al., 2015; Summers et al., 2020; Van Horn et al., 2012). The catchment area to this site is 107 km^2, which spans an elevation change of 2,580 m to 3,432 m (Stroud Water Research Center, 2021).

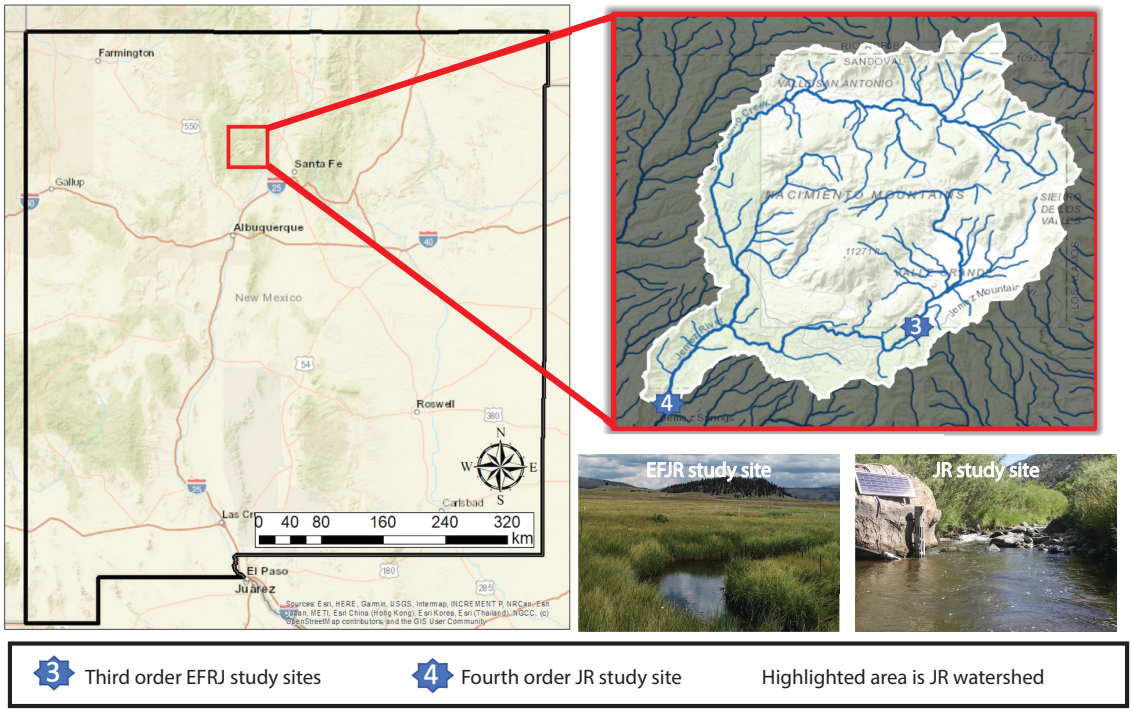

Figure 4.2: Map of the two study sites located in North Central New Mexico. Both sites had water quality sondes deployed within the stream channel *and were collocated near MesoWest climate stations. Over a two-year period nutrient addition experiments were performed at three week interval at both sites to quantify nitrate uptake rates.*

The downstream research site was in the Jemez River (referred to as JR site from here on), downstream of the confluence of the EFJR and the San Antonio stream increasing to a 4th order steam (Figure 4.2). The Jemez River's (JR) average annual discharge is 1400 L/s (2004–2015, USGS gage #08324000), with the study site being a high-gradient canyon stream reach with an average channel slope of 3.25% and woody riparian vegetation. Along this reach, there are significant geothermal inputs that contribute to high specific conductivity (Dyer, 2007; Golla, 2019). The catchment area to our study site is 473 km^2, spanning an elevation of 1,903m to 3,432 m (Stroud Water Research Center, 2021). Note that this area encompasses the upstream site as they are a part of the same fluvial system.

4.2.2 Semi-Continuous Sensor Deployment and Maintenance

Both EFJR and JR sites were equipped with YSI EXO 2 multiparameter water quality sondes (Yellow Springs Instruments, n.d.). Both EXOs measured water temperature, specific conductivity, dissolved oxygen (DO), fluorescence dissolved organic matter (fDOM), turbidity, and pH at 15-minute intervals. HOBO water level loggers were also deployed at each site to measure water depth fluctuations at 15-min intervals. All sensors were cleaned and recalibrated every three weeks per USGS guidelines (Jones et al., 2017; Wagner et al., 2006). Both sites were equipped with solar panels, batteries, and CR1000 dataloggers (Campbell Scientific, n.d.) to power the semi-continuous sensors and for data storage. Co-located at both sites were MesoWest climate stations that measured ambient air temperature, barometric pressure, wind velocity, total solar radiation, and cumulative precipitation at 10-minute intervals (Table 4.1).

Table 4.1: Sensors and parameters being measured at both sites that can be used as predictors to nitrate uptake rate.

Parameter	Sensor Units	Abbreviation	Sampling Frequency (min)	Sensor/ Database
Discharge	cms	---	15	USGS NWIS
Dissolved oxygen	ppm	DO	15	EXO
Specific conductivity	uS/cm	Sp Cond	15	
Water temperature	C	Water Temp	15	
pH		---	15	
fDOM	ppm	---	15	
Air temperature	C	Air Temp	10 and 14.5	MesoWest
Barometric pressure	mmHg	Baro Pres	10 and 14.5	
Wind Velocity	m/s	Wind Vel	10 and 14.5	
Total solar radiation	W/m^2	Solar Rad	10 and 14.5	
Relative Humidity	mm	Rel Hum	10 and 14.5	

Approximately 1km downstream of the EFJR site, a stage sensor owned by the U.S Forest Service was used in conjunction with a rating curve to derive semi-continuous discharge measurements. The Forest Service stage measurements expanded from October 23rd, 2017 to October 19th, 2018. After October 19th, 2018, a HOBO U20 pressure datalogger was deployed at the EFJR sonde site and used to quantify discharge by the development of a site-specific rating curve between average stage and discharge measurements made with a Sontek FlowTracker (Equation S2a). At the JR site, semi-continuous discharge measurements were recorded by USGS stream gage Jemez River Near Jemez Springs (USGS gage #08324000), which is located downstream of the Jemez River and Guadalupe Rivers confluence, approximately 15.8 km downstream of the JR sonde site. To account for discharge inputs from the Guadalupe River, a measured discharge vs a time lagged USGS discharge relationship was developed (Equation S2b).

4.2.3 Quality Assurance and Control of Sensor Data

Data collected from the sondes were imported into Aquarius TimeSeries 21.2.160.0 for data storage and to perform QA/QC procedures on the raw data (Aquatic Informatics, n.d.). Once in Aquarius, we used a spike filter to flag and remove values that were 20% greater than the mean of an hourly moving window. The data were then checked for sensor drift and biofouling by comparing pre to post clean and calibration records to quantify sudden changes within the data records during periods of cleaning and calibration of sensors. If these issues were noted within the dataset, a linear drift correction would be applied from the previous field day to the time of the current field day. After outliers were removed and drift corrections were made, a visual inspection was

performed to ensure that useful data were not accidentally identified as outliers and to ensure accurate corrections for sensor drift.

4.2.4 Nutrient Addition Experiments

Nitrate injections were performed to calculate nitrate uptake rates at a three-to-four-week interval. In the field, discharge was measured before each injection using a SonTek FlowTracker, and the recorded discharge, stream width, and average water velocity were entered into the Tracer Injection Planning Tool solute transport toolbox to estimate the mass of conservative (NaBr) and reactive tracers needed ($NaNO_3$), and the minimum distance between the injection site and the upstream sampling location required to achieve lateral and vertical mixing (González-Pinzón et al., 2022). The solute transport toolbox combines the advection dispersion equation with empirical relationships derived from an extensive USGS metanalysis (Jobson, 1997), within Microsoft Excel, to plan tracer injections to include nutrient addition experiments.

Once the mixing length and tracer masses were known, the salts were mixed with stream water collected on-site and then an instantaneous tracer addition was performed following standard guidelines (Leibundgut et al., 2009). With all tracer addition experiments, the sampling location site was always co-located with our sensor site; for this, we moved the injection site as a function of mixing length requirements. Grab samples were collected by rinsing a 20 ml plastic syringe three times with stream water before each grab sample was taken. The collected water was immediately filtered using a 0.45 μm nylon filter, then immediately stored in ice coolers and transferred to lab

refrigerator to prevent degradation. One to three days after grabs sampled were collected, the samples were analyzed for tracer anion concentrations using a Dionex ICS-1000 Ion Chromatographer, utilizing a AS23/AG23 analytical column combination.

4.2.5 Solute Transport Model

We used a one-dimensional, in-stream, reach-scale model to describe the transport and reactivity of the tracer compounds injected (Knapp et al., 2017; Runkel, 1998). This model simulates exchange with a transient storage zone using uniform and time-invariant coefficients. The model applied here is similar to the one made available as a MATLAB script in Knapp & Cirpka (2018). It considers the transient storage zone as a single, well-mixed zone that undergoes linear exchange (generating an exponential transit time) with the main channel, and accounts for the compound specific behavior of NO_3.

The coupled governing equations for the conservative tracer (i=0), and reactive tracer (i=1), are:

$$\frac{\partial c_i}{\partial t} + \frac{A_s}{A}\frac{\partial c_{ts,i}}{\partial t} + v\frac{\partial_{c_i}}{\partial x} - D\frac{\partial^2 c_i}{\partial x^2} = \frac{A_s}{A} r_{ts,i} \quad (1),$$

$$\frac{\partial c_{i,ts}}{\partial t} = k\left(c_i - c_{ts,i}\right) + r_{ts,i} \quad (2),$$

subject to the following initial and boundary conditions of an instantaneous tracer injection:

$$c_i(x, t = 0) = c_{ts,i}(x, t = 0) = 0 \; \forall x \tag{3},$$

$$(vc_i - D\frac{\partial c_i}{\partial x})|_{x=0} = \frac{M_i}{A}\delta(t) \tag{4},$$

$$\lim_{x\to\infty} c_i(x, t) = 0 \; \forall \; t \tag{5},$$

where c_i $[mol\ m^{-3}]$ denotes the solute concentration in the main channel; $c_{ts,i}$ $[mol\ m^{-3}]$ represents the solute concentration in the transient storage zone; the in-stream advective velocity is given by v $[m\ s^{-1}]$; D $[m^2\ s^{-1}]$ represents the dispersion coefficient; $\frac{A_S}{A}$ $[-]$ represents the ratio of the cross-sectional area of the storage zone A_S $[m^2]$ to that of the stream A $[m^2]$; the reaction rate is given by $r_{ts,i}$ $[mol\ m^{-3}s^{-1}]$ the first-order mass-transfer rate coefficient for exchange with the storage zone is given by k $[s^{-1}]$; and M_i $[mol]$ represents the injected tracer mass. Nutrient uptake was assumed to follow first-order kinetics (González-Pinzón and Haggerty, 2013), resulting in the following reactions rates:

$$r_{hz,1} = -\lambda_1 c_{ts,1} \tag{6},$$

where λ_1 $[s^{-1}]$ is the total nitrate uptake rate coefficient.

Lastly, due to total nitrate uptake rates often having small values, often less than $1.0 * 10^{-5}$, and non-normal distributions, the uptake rates were logged transformed prior to model training (Figure S4.3). After the model has made its predicted log uptake rate, its predictions are transformed back to a non-log scale and compared to the non-transformed observed uptake rate.

4.2.6 Outlier Removal

Outliers within nitrate uptake rates were identified as values having more than 1.5 interquartile ranges above the upper or below the lower quartiles (Blázquez-García et al., 2020). Data points flagged as possible outliers went through a visual inspection to identify if their BTCs were either poor fitting or irregular thus being verifying them as a true outlier. Out of the 40 nutrient addition experiments performed, six were identified and removed as outliers. If a nitrate uptake rate is verified to be a true outlier, then it and its associated high-frequency predictor sequence was removed from the dataset prior to model training.

4.2.7 High-Frequency Parameter Templates

Multiparameter predictors were selected to create multiple predictor templates that increased in dimensionality and associated logistical costs or data limitations of specific template (Table S4.4). These templates are then used as model predictors when estimates nitrate uptake rates. Atmospheric parameters were grouped into a single template (referred to as Atmos) due to large spatial extent in which meteorological stations cover the United States (MesoWest, 2022). Atmospheric parameters with discharge were combined into a single template (referred to as AtmosDis) due to discharge being the most ubiquitous surface water property measured in USGS stream gage network (U.S. Geological Survey, 2022). Water quality parameters were allocated into a separate template with discharge (referred to as Water), since water quality sondes measuring all five water quality parameters have a lower spatial resolution than that of

meteorological stations and are collocated with stream gages. Lastly, all available parameters were used combined to generate a template to maximize predictor dimensionality (referred to as AtmosWater). For non-recurrent neural networks algorithms that require one-to-one regression, a single feature was extracted per a predictor by averaging the high-frequency data to the day in which a nitrate addition was performed. For the recurrent neural networks that can perform sequence-to-one regression, 15-minute data for each predictor from 00:00 to 24:00 in which a nitrate addition was performed was used as sequence predictors. By utilizing a 24-hour sequences the predictors can leverage temporal dynamics such as diel cycling and rates of change that is filtered when taken a daily average value (Figure 4.1).

4.2.8 Machine Learning Regression Analysis

To test whether recurrent neural networks can leverage high-frequency data to increase model accuracy on estimating nitrate uptake, three non-neural network regression algorithms, linear regression, decision tree, and support vector regression (SVR), that require feature engineering were tested against a Gated Recurrent Unit (GRU) which is a recurrent neural networks that can perform sequence-to-one regression. Linear regression, decision tree, and SVR models were developed using Matlab's Statistics and Machine Learning Toolbox, while GRU model was developed using Matlab's Deep Learning Toolbox (Mathworks Inc, n.d.). Below is a brief description and mathematical functions of each algorithm tested.

Linear Regression: The algorithm with the highest model bias tested was linear regression, which aims to minimize the mean square error (MSE) between observed values and a hypothesized linear trend. Gradient decent is used to minimize the MSE by iterating the partial derivative of the MSE at a predefined learning rate until it converges to a minimum value (Equations 7-9). The benefit of linear regression models is that their hypothesized function is highly interpretable, and they are computationally inexpensive, but they prone to have high bias when fitting non-linear data sets (Maulud & Abdulazeez, 2020). Prior to cross-validation, linear regression model assumptions of homoskedasticity, normally distributed residuals, and collinearity were checked. Out of the model assumptions, only collinearity was violated so parameters with high collinearity were removed per a parameter template (Table S4.5).

$$y = \theta + \theta_1 x_1 + \cdots + \theta_n x_n \quad (7),$$

$$\theta_n \coloneqq \theta_n - \alpha * \frac{\partial}{\partial \theta_n} J(\theta) \quad (8),$$

$$J(\theta) = \frac{1}{2m} \sum_{i=1}^{m} \left(y^i - x^i\right)^2 \quad (9),$$

where y is the model estimate, θ_n are the model fitted parameters, x_n are the training examples, α is a learning rate constant, $J(\theta)$ is the MSE cost function, and m is the number of observations.

Decision tree: For an intermediate model bias a decision tree algorithm was tested, decision regression trees which aim to divide the training data into smaller subsets, known as leaf nodes, by model-defined conditions within the predictor variables. The model uses iterative variance reduction to define the conditions to use to split the

data (Equation 10-12). After the training data has been subdivided into leaf nodes, the target data in each leaf node is averaged to derive an output estimate for each node. The model makes estimates from the cross-validation data by subdividing the test data by the same model-defined conditions, and estimates are made based on which leaf node in which all conditions are met (Equation 16). Regression trees have high to medium interpretability and low computational expense, but they have low performance on linear relationships and are prone to converge on local optima, producing instability in model predictions.

$$Var_n = \frac{1}{m}\sum_{i=1}^{m}\left(y^i - \bar{y}\right)^2 \quad (10),$$

$$VR = \min\left(Var_n - \sum_{i=1}^{2}\frac{m_{n+1}^i}{m_n}Var_{n+1}^i\right) \quad (11),$$

$$y = \sum_{i=1}^{m} C_i I\{x^i \in R^i\} \quad (12),$$

where y is the model estimate, C_i is the average of the training examples that fall into subdivision R_i, $I\{x^i \in R^i\}$ is a binary identity function of R_i that equals 1 if training example x_i falls within subdivision R_i or a 0 if it fall into another subdivision, and m is number of training examples.

Support vector regression (SVR): The model with the lowest bias and highest variance of the non-neural network machine learning algorithms tested was a gaussian support vector machine (gSVM), which utilize large margin regression that aims to equally increase the positive and negative boundaries between the hypothesized gaussian

kernels and the observed data (Equations 13-15). The benefit of using gSVMs is that that they can fit non-linear data with a limited number of observations, while trying to minimize overfitting and are computationally less expensive compared to neural networks, but are less interpretable than linear regression and decision trees (Raghavendra. N & Deka, 2014). Prior to SVR training, parameter's scales were standardized by centering the mean of a parameter at zero and scaling by its standard deviation.

$$y = \sum_{i=1}^{m} (\alpha_i - \alpha_i^*) G(x_i, k_i) + b \quad (13),$$

$$G(x_i, k_i) = \exp\left(-\frac{\left|\left|x_i - k_i\right|\right|^2}{2\sigma^2}\right) \quad (14),$$

$$\sum_{i=1}^{m} (\alpha_i - \alpha_i^*) = 0 \quad (15),$$

where y is the model estimate, $\alpha_i \; and \; \alpha_i^*$ are Lagrange multipliers, $G(x_i, k_i)$ is a kernel density function, k_i is the kernel centroid, σ is a kernel scaling constant, and b is a model base term.

Gated recurrent unit (GRU): Recurrent neural networks have been proven to be effective at making estimates from sequential data minimizing the need for extensive feature engineering (Fan et al., 2020; Gao et al., 2020; Gharehbaghi et al., 2022). However, they are often suspectable to vanishing or exploding gradients when training from high dimensionality long sequential data, ultimately limiting their capability to learn (Shen, 2018). To avoid this problem, memory based recurrent neural networks such as gated recurrent unit (GRU) have been developed and widely used for time series

regression. A GRU utilizes on an update gate and reset gate, which allows them to discard noise from pervious observations within the training sequences while retaining important features that can be leveraged to make predictions (Chung et al., 2014). GRUs have been shown to outperform other machine learning algorithms when performing sequential regression, but can be prone to overfitting and slow convergence, and can produce differing estimates from the same training data due to stochastic gradient descent (Fan et al., 2020; Xu & Liang, 2021). Prior to GRU training, parameter's scales were standardized by centering the mean of a parameter at zero and scaling by its standard deviation. The governing equations for a GRU architecture are:

$$r_t = \sigma(W_r \cdot [h_{t-1}, x_t] \quad (16),$$

$$z_t = \sigma(W_z \cdot [h_{t-1}, x_t] \quad (17),$$

$$\hat{h}_t = tanh(W_h \cdot [r_t * h_{t-1}, x_t] \quad (18),$$

$$h_t = (1 - z_t) * h_{t-1} + z_t * \hat{h}_t \quad (19),$$

$$\hat{y}_t = \sigma(W_o \cdot h_t) \quad (20),$$

where r_t is the reset gate at time of t, $z_t$is the update gate at time of t, x_t is the cell input, h_t and h_{t-1} is the cell output for time t and the cell output from the previous timestep, respectively, σ is the sigmoid activation function, W is the cell weights at each respective gate, y_t is cell estimate at time t.

4.2.9 Hyperparameter Optimization

To optimize model performance, both SVR and GRU hyperparameters were tuned using a grid search through a range of expected hyperparameter values on a subset

of data truncated from the global data (Yang & Shami, 2020). Due to the large computation cost of grid searching, with thousands of separate model iterations of varying hyperparameter values, UNM's Center for Advanced Research Computing supercomputer Wheeler was used during grid search optimization. Due to a limited number of dependent observations, the subset of data used for hyperparameter optimization was determined by randomly selecting 20% of the data ensuring that the subset's dependent variable was representative of the global dependent distribution by comparing standard deviations and means of the two datasets. After optimal hyperparameters were determined (Table S4.6), the subset of data was reintroduced to the global dataset for model testing.

4.2.10 Cross-Validation Technique

Leave-one-out cross validation (LOOCV) was utilized to test the performance of each model due to the limited number of measured dependent variable observations mitigating high-computational costs. LOOCV truncates the maximum amount of data to train the model by removing a single dependent observation and its respective high-frequency sequence predictors to be used for testing. After the model has been trained on the training data, the trained model then is given the high-frequency predictors from the test dataset to make a nitrate uptake estimate. Afterwards, the test dataset in reinterrogated into the training dataset and the model is retrained and tested on a new set of data until each dependent observation, and its respective predictor sequences, is used

as the test dataset. Thus, allowing for the model to be trained and tested across the entire global dataset while mitigating data leakage in model testing (Roberts et al., 2017).

Mean absolute error (MAE) and coefficient of determination (R^2) will be calculated from cumulative LOOCV observed vs model estimated nitrate uptake rates to compare model performance. The advantage of MAE is that it calculates an average magnitude of model error that is in the same units as the dependent variable the model is trying to predict and is more robust to outliers than RMSE (Willmott & Matsuura, 2005). R^2 normalizes model error with 1 being a model with perfect predictive accuracy, and $R^2 < 0$, indicates a model's performance worse than using an average uptake rate calculated from the global dataset (Dangeti, 2017). Lastly, past studies have shown order of magnitude difference in nitrate uptake rates when comparing across multiple sites of vary spatial heterogeneity(Ensign & Doyle, 2006; Mulholland et al., 2008); therefore, to test the model's accuracy across both sites, the percentage of model estimates less than 0.5 and 0.25 an order of magnitude difference from the observed uptake rates will be quantified as another metric of performance.

$$MAE = \frac{\sum_{i=1}^{n} |\hat{y}_i - y_i|}{n} \quad (21),$$

$$R^2 = 1 - \frac{(\hat{y}_i - y_i)^2}{(y_i - \bar{y}_i)^2} \quad (22),$$

where $\hat{y}_i$ $[s^{-1}]$ is the model estimated nitrate uptake rate, y_i $[s^{-1}]$ is the observed nitrate uptake rate, $\bar{y}_i$ $[s^{-1}]$ is the mean observed nitrate uptake rate, and n is the number of observed nitrate uptake rates.

4.3 Results

4.3.1 Nutrient Addition Experiments

Out of the 40 total nutrient additions that were performed from 2018 to 2020, 6 experiments were identified as outliers and removed, leaving a total of 34 uptake rates, i.e., 17 uptake rates from EFJR and 17 from JR. Out of the 34 measured uptake rates, 4 were measured from during the spring months from April to June, 10 were measured during summer from June to September, 16 were measured during fall from September to November, and 4 were measured during the winter from November to April. It should be noted that nitrate uptake rate was not measured at EFJR during the winter months due to excessive snow and ice-cover (Nichols et al., 2022). The average uptake rates for the EFJR and JR were $7.05 * 10^{-5}$ and $4.28 * 10^{-5} s^{-1}$, respectively, and the difference between the two site's measured uptake rates were statistically significant (p-value <0.05 using Wilcoxon rank sum test). At EFJR, uptake rate was significantly higher during 2018 compared to 2019 with year-to-year averages of $1.66 * 10^{-5}$ and $3.31 * 10^{-5}\ s^{-1}$, respectively (p-value <0.05). However, at JR the decrease in uptake rate from $6.69 * 10^{-5}$ in 2018 to $3.46 * 10^{-5}\ s^{-1}$ in 2019 was not statistically significant (p-value = 0.12) (Figure 4.3).

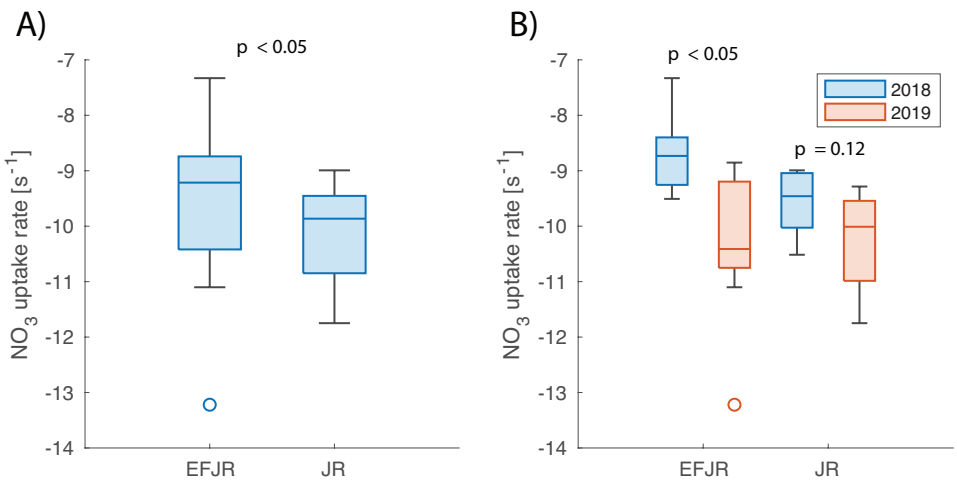

Figure 4.3: Boxplots of measured nitrate uptake rates at both sites. A) Nitrate uptake rates grouped by site. B) Nitrate uptake rates group by site and subgrouped by year. P-values from Wilcoxson rank sum test are between sites and between years are annotated above respective boxplot grouping.

4.3.2 High Frequency Sequential Data

Discharge across both sites varied significantly (p-value < 0.05) with 2018 flows averaging 0.08 and 0.32 $m^3 s^{-1}$, and for 2019 averaging 0.20 and 1.18 at EFJR and JR, respectively (Table 4.2, Figure 4.4). At both sites, fDOM concentrations increased concurrently with elevated discharge with 2018 fDOM values averaging 15.7 RFU at EFJR and 12.3 RFU at JR, while 2019 values averaged 24.0 RFU at EFJR and 14.5 RFU at JR. Unlike fDOM, turbidity generally decreased with discharge, averaging 13.5 FNU and 9.81 FNU in 2018, and averaging 5.60 FNU and 5.05 FNU in 2019 at EFJR and JR, respectively. Between 2018 and 2019, water temperature, pH, and dissolved oxygen did vary significantly as both sites (highest p-value =0.002) with an exception for dissolved oxygen EFJR (p-value=0.77). Overall, JR had higher water temperature, pH, and dissolved oxygen with averages of 10.6 C, 7.60, and 9.43 $mg\ L^{-1}$ compared to 10.2 C, 7.31, and at 7.20 $mg\ L^{-1}$ EFJR. Specific conductivity at JR was significantly higher than

that at EFJR (p-value <0.05), with site averages of 624 us/cm and 92.2 us/cm at JR and EFJR, respectively. The difference in specific conductivity between sites is primarily due to upstream groundwater springs making a large contribution to baseflows.

Table 4.2: Year-to-year and overall averages of 15-minute water quality sonde and meteorological data used for predictors in machine learning algorithms. Blue indicates the year that the predictor was significantly higher, green indicates the sites across both years that the predictor was significantly higher, and rows with no color indicates that there was not a significant change between years or between sites.

Param	Units	EFJR			JR		
		2018	2019	Overall	2018	2019	Overall
Discharge	$m^3 s^{-1}$	0.08	0.2	0.14	0.32	1.18	0.9
Water Temp	C	8.72	11.43	10.2	11.1	10.2	10.6
DO	$mg\ L^{-1}$	7.21	7.18	7.2	9.17	9.4	9.43
pH	-	7.18	7.45	7.31	7.43	7.61	7.6
Sp Cond	$us\ cm^{-1}$	98.1	86.9	92.2	668	602	624
fDOM	RFU	15.7	24	20	12.3	14.5	13.5
Turbidity	FNU	13.5	5.6	9.46	9.81	5.05	7.01
Air Temp	C	2.97	8.97	5.78	12.2	9.58	9.79
Baro Press	kPa	562	561	562	609	607	608
Wind Vel	$m\ s^{-1}$	0.53	0.561	0.545	0.681	0.64	0.655
Rel Hum	%	67.6	58.4	63.5	42.29	46.8	45.5
Solar Rad	$W\ m^{-2}$	212	260	234	176	174	173

Atmospheric parameters air temperature, solar radiation, wind velocity, barometric pressure, and relative humidity varied significantly across the two sites (p-value <0.05). However, unlike the comparison between the two sites, barometric pressure (p-value=0.98) and wind velocity (p-value=0.92) between 2018 and 2019 were not significantly different at EFJR, while at JR there wasn't a significant difference for solar radiation (p-value=0.97). Site averages for air temperature, solar radiation, wind velocity, barometric pressure, and relative humidity at EFJR were 5.78 C, 234 $W\ m^{-2}$, 0.545

$m\ s^{-1}$, 562 kPA, and 63.5%, respectively (Table 4.2, Figure 4.4). While at JR averages for air temperature, solar radiation, wind velocity, barometric pressure, and relative humidity were 9.79 C, 173 $W\ m^{-2}$, 0.655 $m\ s^{-1}$, 608 kPA, and 45.5%, respectively.

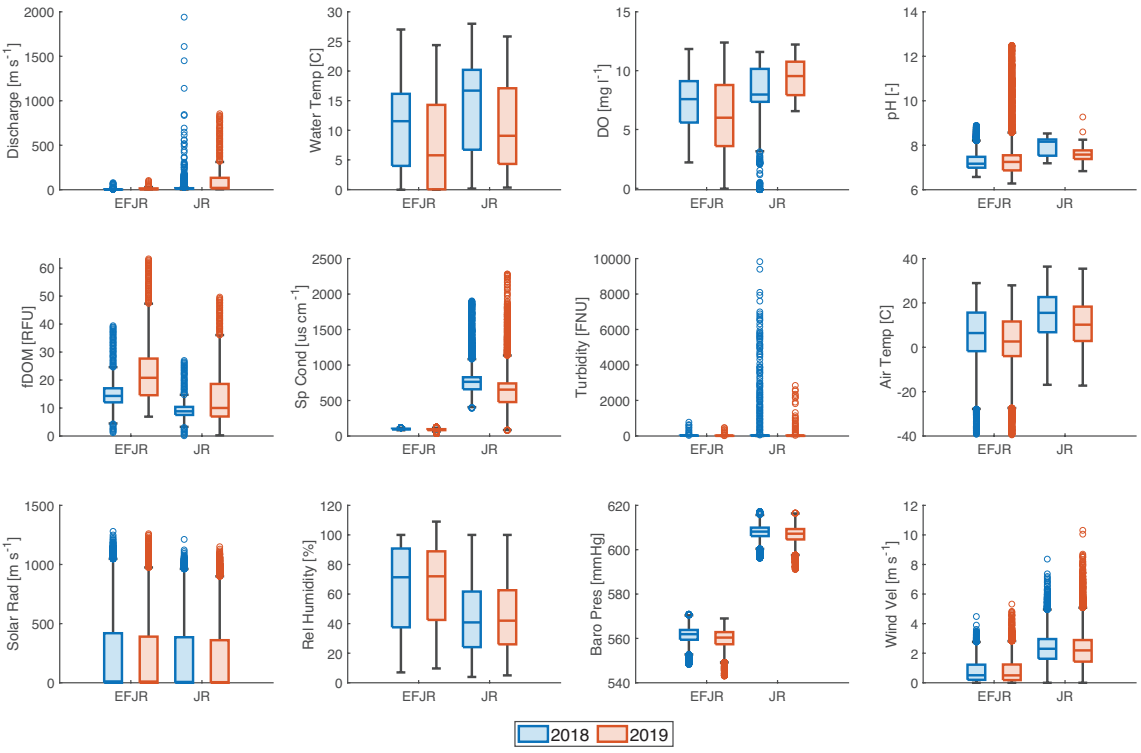

Figure 4.4: Boxplot of water quality and atmospheric 15-minute data observed during the days in which nutrient addition experiments were performed.

4.3.3 Model Results

4.3.3.1 Differing Machine Learning Algorithms

When comparing average MAE across all parameter templates, SVR has the lowest average MAE of $5.7* 10^{-5}\ s^{-1}$ followed by decision tree with $6.26* 10^{-5}\ s^{-1}$, linear regression with $6.34* 10^{-5}\ s^{-1}$, and GRU with an average MAE of $1.22* 10^{-5}\ s^{-1}$. Linear regression's MAE ranged from $5.58* 10^{-5}\ s^{-1}$ to $6.90* 10^{-5}\ s^{-1}$ when

utilizing water quality and all available parameters as predictors. Decision tree had the highest MAE of $6.47 * 10^{-5}\ s^{-1}$ when utilizing all available parameters as predictors, and like linear regression, decision tree's lowest MAE of $6.01 * 10^{-5}\ s^{-1}$ was measured when utilizing water quality predictors. SVR had its lowest MAE of $5.15 * 10^{-5}\ s^{-1}$ across all models when utilizing water quality predictors, while its highest MAE of $6.26 * 10^{-5}\ s^{-1}$ when using atmospheric predictors. Lasty, GRU had the second lowest MAE of $5.28 * 10^{-5}\ s^{-1}$ for atmospheric predictors, but also had the highest measured MAE of $2.64 * 10^{-4}\ s^{-1}$ when using water quality predictors (Table 4.3).

Table 4.3: Performance metrics for each model with varying parameter templates. Green indicates best model performance and yellow the worst for each respective parameter template and performance metrics. Oom represents the order of magnitude difference between the observed nitrate uptake rates and the estimated rates.

	Atmos				**AtmosDis**			
	MAE	R^2	% < 0.5 OoM	% < 0.25 OoM	MAE	R^2	% < 0.5 OoM	% < 0.25 OoM
Linear	$6.39*10^{-5}$	0.12	78	50	$6.90*10^{-5}$	0.07	80	44
Tree	$6.40*10^{-5}$	0.11	75	47	$6.15*10^{-5}$	0.16	80	50
SVR	$6.22*10^{-5}$	-0.03	83	63	$5.93*10^{-5}$	-0.02	86	58
GRU	$5.28*10^{-5}$	0.48	86	63	$5.33*10^{-5}$	0.36	83	58
	Water				**AtmosWater**			
	MAE	R^2	% < 0.5 OoM	% < 0.25 OoM	MAE	R^2	% < 0.5 OoM	% < 0.25 OoM
Linear	$5.58*10^{-5}$	0.23	86	63	$6.12*10^{-5}$	0.27	80	44
Tree	$6.01*10^{-5}$	0.08	75	58	$6.47*10^{-5}$	0.14	77	50
SVR	$5.15*10^{-5}$	0.17	88	66	$5.44*10^{-5}$	0.16	88	61
GRU	$2.64*10^{-4}$	-5.73	83	50	$1.16*10^{-4}$	-6.61	80	44

The R^2 values for linear regression ranged from 0.27 to 0.07 with the highest value being recorded when utilizing water quality predictors and its lowest when using all available parameters. Decision Tree had relatively low but consistent R^2 values when compared to the other model architectures that ranged from 0.08 to 0.16 when utilizing water quality and atmospheric parameters with discharge as predictors, respectively. SVR R^2 values ranged from -0.02 to 0.17 when utilizing atmospheric and water quality predictors, respectively. Lastly, GRU had the highest and lowest R^2 values out of any

model with a range of 0.46 for atmospheric predictors to -6.61 when using all available parameters (Figure 4.5). When comparing model performance by the percentage of model estimates that were less than 0.5 and 0.25 an order of magnitude, linear regression had an average of 81.0% and 50.3%, respectively. Decision tree had the worst performance when comparing average 0.5 and 0.25 less than an order of magnitude with 76.8% and 52.3%, respectably. Both SVR and GRU had improved performance than that of linear and decision tree regression when comparing orders of magnitude difference from observed values, but overall, the SVR outperformed GRU with 86.3% and 53.8% compared to 83.0% and 53.8% (Table 4.3).

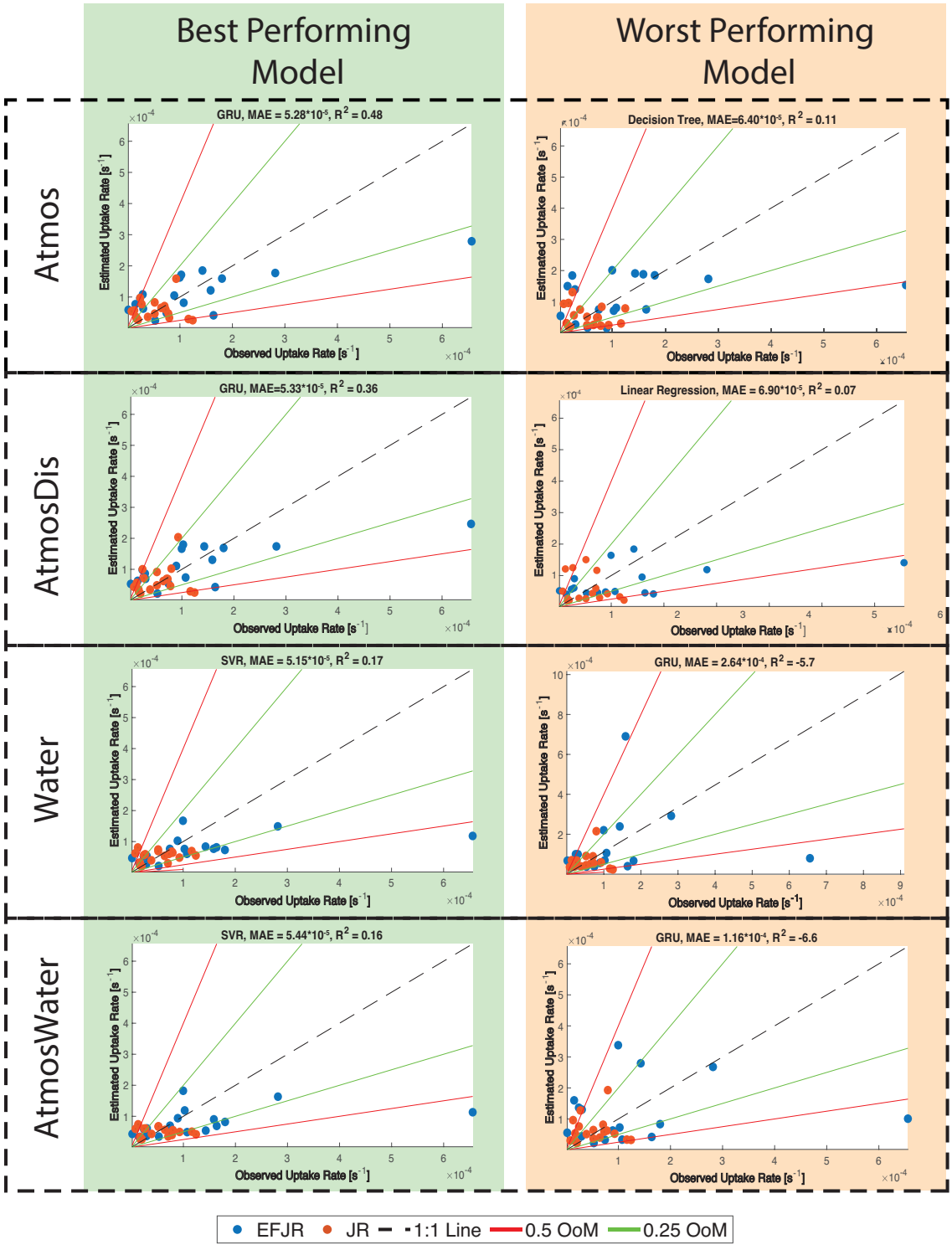

Figure 4.5: Predicted vs. Observed scatter plots after leave one out cross validation. The best and worst models for each parameter template are plotted based on their respective MAE values. Oom represents the order of magnitude difference from the observed values with the green line illustrating the 0.25 order of magnitude difference threshold and the red line the 0.5 order of magnitude difference threshold.

4.3.3.2 Model Performance Across Parameter Templates

The average MAE values across the four model architectures when using atmospheric predictors was $6.03 * 10^{-5}\ s^{-1}$, atmospheric predictors with discharge $5.92 * 10^{-5}\ s^{-1}$, water quality predictors $1.08 * 10^{-4}\ s^{-1}$, and all available parameters as predictors $7.73 * 10^{-5}\ s^{-1}$. Atmospheric parameter templates MAE values ranged from $5.28 * 10^{-5}\ s^{-1}$ to $6.40 * 10^{-5}\ s^{-1}$, atmospheric predictors with discharge ranged from $5.33 * 10^{-5}\ s^{-1}$ to $6.90 * 10^{-5}\ s^{-1}$, water quality predictors ranged from $5.15 * 10^{-5}\ s^{-1}$ to $2.64 * 10^{-4}\ s^{-1}$, and all available parameters as predictors ranged from $5.44 * 10^{-5}\ s^{-1}$ to $1.16 * 10^{-4}\ s^{-1}$. R^2 values averaged across all four models were 0.19, 0.17, -1.25, and -1.66 for atmospheric, atmospheric with discharge, water quality, and all available parameters as predictors, respectively. The parameter template with the highest R^2 value was atmospheric predictors with an R^2 of 0.48, while the template with the lowest R^2 was all available parameters as predictors with an R^2 of -6.61. The highest R^2 value for atmospheric with discharge as predictors, water quality, and all available parameters was 0.36, 0.23, and 0.27, respectively (Figure 4.5). The parameter template that had the highest percent of estimated values less than 0.5 and 0.25 order of magnitude was water quality template when being utilized by SVR with 86% and 66%, respectively. The parameter templates that had the lowest percent of estimated values above 0.5 order of magnitude was atmospheric and water quality templates with both being 75% when being utilized by the decision tree model, while the template that had the lowest percent of estimated values above 0.25 order of magnitude was when utilizing all available parameters with the GRU model with 44% (Table 4.3).

4.4 Discussion

4.4.1 Sequence-to-One Performance Compared to One-to-One Regression Algorithms for Predicting Nitrate Uptake

When utilizing atmospheric parameters as model predictors, the GRU utilizing sequence-to-one regression outperformed all other model architectures (Figure 4.5, Table 4.3). The improvement demonstrates that the recurrent neural network can leverage the information-rich atmospheric data to estimate fluvial nitrate uptake rates across monitoring sites of varying biotic and abiotic properties. We hypothesize that the improvement from the GRU is primarily due to the model leveraging diel cycling, trends, and antecedent conditions and events within the sequential data, which previous studies have shown to be essential features when understanding primary drivers of uptake rate variability (Drake et al., 2018; R. J. O. Hall & Tank, 2003; Wollheim et al., 2014). Since the only feature engineering performed for the one-to-one regression was taking the daily average for each predictor, the predictors would not have been able to encompass temporal seasonality and trends (Nimick et al., 2011). However, the GRU's MAE increased an order of magnitude when incorporating water quality parameters as predictors. Further inspection validated that the high MAE and negative R^2 is due erroneous predictions from the model occurring on less than 10% of the test data that skewed the MAE and R^2 values for the water quality and all available parameter templates (Figure 4.5).

While additional feature engineering can be performed to improve non-recurrent neural network model performance, which often requires extensive domain knowledge to identify key features that encompass nutrient processing mechanisms within a stream

reach, the resulting model may fail to generalize varying biotic and abiotic factors due to its training on site-specific predictor features. For example, past studies have shown that multiple factors such as gross primary production, nutrient stoichiometry, flow conditions, channel geomorphology, or land-use changes are common drivers in nitrate uptake, but their significance varies spatial and temporally, thus dictating which features to extract as predictors (Arango et al., 2008; Ensign & Doyle, 2006; R. O. Hall et al., 2013; Heathwaite, 2010).

4.4.2 Model Performance as a Function of Parameter Templates

To test whether increasing the number of sensors, thus increasing the number of high-frequency parameters that can be used as predictors to estimate nitrate uptake rate, we subdivided the high-frequency parameters into separate templates based on their associated costs. The GRU model performance generally decreased as the number of predictors increased, with its best performance measured using atmospheric parameters and its worst performance using all available parameters as predictors. Unlike the GRU model, the support vector regression performance improved with an increase in the number of predictors, with considerable improvement when utilizing water quality parameters as predictors. The distinction between model performance across parameter templates is a critical consideration when scaling nitrate uptake predictions across more watersheds since each parameter template has unique data access and logistical cost constraints. For instance, currently, MesoWest operates approximately 40,000 climate stations across CONUS. In contrast, the USGS operates 8,500 stream gages across CONUS, and of those 2000 USGS stream gages monitor high-frequency water quality

parameters, with 1867 of those sites measuring water temp, 1060 measuring specific conductance, 628 measuring dissolved oxygen and turbidity, and only 52 measuring fDOM (MesoWest, 2022; U.S. Geological Survey, 2022).

The discrepancy in spatial coverage between high-frequency water quality and climate data is further compounded by the fact that climate stations typically require less maintenance, thus, lowering the long-term logistical and financial costs of new site development in areas of limited instrumentation. The high costs associated with high-frequency water quality monitoring has led to a disproportionate amount of monitoring sites being implemented in the east of the Mississippi and west of the Colorado River, with 49% and 25% of monitoring sites being located in those regions (U.S. Geological Survey, 2022), respectively, which further complicates scaling nutrient uptake predictions to a CONUS scale when utilizing water quality parameters as model predictors; therefore, determining a model architecture that performs well when only using atmospheric parameters as predictors, the GRU architecture, can be advantageous for development of a CONUS scale model to estimate nitrate uptake rates in stream reaches where nutrient addition experiments have not been performed to measure nitrate uptake rates directly.

4.5 Conclusion

Excess nitrate within fluvial systems has become a major water quality concern and can lead to eutrophication and harmful algae blooms occurring in lakes and estuaries when left untreated. Due to the risk high risk access nitrate imposes, there has been considerable research nitrate transport processes in fluvial system with a primary focus on nitrate uptake rate. By understanding nitrate uptake rates, researchers can quantify

nitrate sinks and key forcing variables in uptake variability allowing for more effective remediation efforts. However, to quantify nutrient uptake rate, one traditionally needs to perform a nutrient addition experiment, which can be financially and logistically expensive. Due to the high costs associated with such experiments, many experiments have been performed in low order streams that are not scalable to higher order streams. Compounding on the high costs, a single nutrient addition experiment only gives you a snapshot of uptake rate through time, which is known to be temporally dynamic.

By developing a methodology that allows for semi-continuous estimates of nitrate uptake rate using sensors as proxies, we can relieve the difficulties associated with quantifying nitrate uptake rate variability. To do test the viability of using sensor data as proxies to uptake rate, we tested four machine learning algorithms of varying model bias and variance with parameters templates comprised of differing sensor configuration with accompanying costs and data accessibility restrictions. Our results demonstrate that when using atmospheric parameters as predictors, a gated recurrent neural network (GRU) using sequence-to-one regression had the best prediction performance. However, when utilizing water quality parameters, the GRU had poor performance due to erroneous predictions on less than 10% of the test data. When incorporating water quality parameters as predictors the model that had the best performance was support vector machine using one-to-one regression.

Both high-frequency atmospheric and water quality data are increasing in accessibility, but there remains a large discrepancy between the two parameter sets spatial coverage. Since atmospheric parameters are more ubiquitous than water quality parameters, the most viable model architecture and parameter template for CONUS scale

modeling based on our result would be a GRU using atmospheric parameters as predictors to nitrate uptake rate. However, the current greatest limitation to implementing model on the CONUS scale is the lack of database that consolidates nitrate uptake rate measurements made from prior nutrient uptake experiments. Such a database in conjunction with high-frequency atmospheric parameters and static catchment characteristics could enable researchers to leverage the improved predictive capability of recurrent neural networks utilizing sequence-to-one regression to estimate nitrate uptake rates in fluvial system.

Acknowledgements: The National Science Foundation provided support for this research through grants CBET-1707042, HRD- 1345169, HRD-1720912, HRD-1914778, and EES- 1914490

Supplemental Information

Figure S4.1) Conceptual figure illustrating the traditional steps taken when measuring nitrate uptake rate in a fluvial system and an estimated cost associated with a single nitrate uptake measurement.

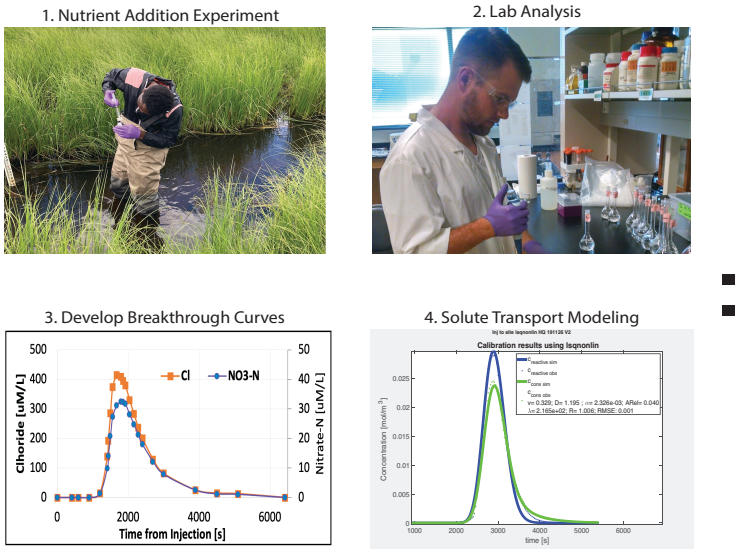

Cost Per a Single Uptake Rate Measurement	
# of Personnel	3
Total Man-Hours	40
Total Grab Samples	30
Total Cost	~$1200

*Assuming a $15 per an hour of work and $20 per a grab sample for field supplies and lab anaysis

Equations S4.2) Equations used to calculate discharge based off of site-specific rating curves.

$$Q_{EFJR} = 1.21e^{0.82*Stage} \quad \text{(a)},$$
$$Q_{JR} = 0.20 * Q_{08324000} + 0.217 \quad \text{(b)},$$

Where $\boldsymbol{Stage}$ is the measured water column stage [m] at site EFJR, $\boldsymbol{Q_{EFJR}}$ is the estimated discharge [$\boldsymbol{m^3 s^{-1}}$], $\boldsymbol{Q_{08324000}}$ is the 8-hour lagged recorded discharge [$\boldsymbol{m^3 s^{-1}}$] at USGS Streamgage 08324000, and $\boldsymbol{Q_{JR}}$ is the estimated discharge [$\boldsymbol{m^3 s^{-1}}$] at JR.

Figure S4.3) Distribution of measured nitrate uptake rates at both study sites. A) Non-transformed uptake rates histogram, B) QQ-plot of non-transformed uptake rates, C) logged-transformed uptake rates histogram, and D) QQ-plot of logged-transformed uptake rates.

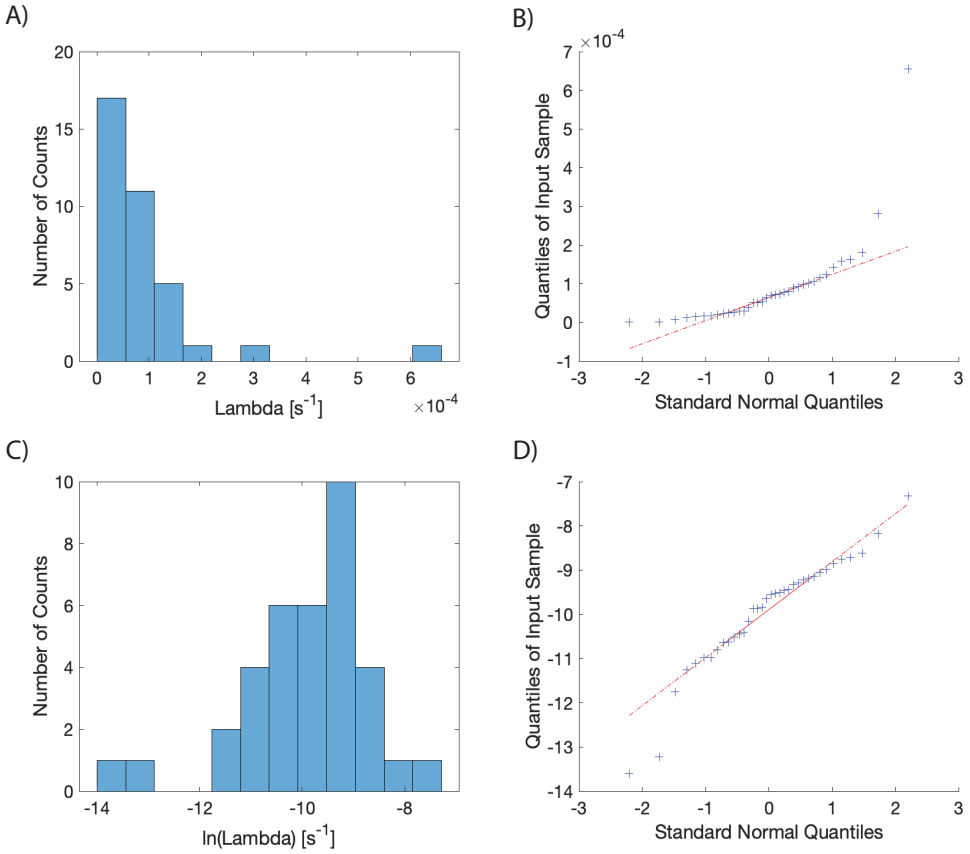

Table S4.4) Parameter templates used as predictors when training and testing the varying machine learning algorithms.

Template	Abbreviation	Parameters	Required Database or Sensors
Atmospheric	Atmos	Air Temp, Solar Rad, Baro Pres, Wind Vel, Rel Humidity	MesoWest (Database)
Atmospheric and Discharge	AtmosDis	Discharge, Air Temp, Solar Rad, Baro Pres, Wind Vel, Rel Humidity	USGS NWIS (Database), MesoWest (Database)
Water Quality and Discharge	Water	Discharge, Water Temp, DO, pH, Sp Cond, fDOM, Turbidity	USGS NWIS (Database), EXO 2 (Sensor)
Atmospheric, Discharge, and Water Quality	AtmosWater	Discharge, Air Temp, Solar Rad, Baro Pres, Wind Vel, Rel Humidity, Water Temp, DO, pH, Sp Cond, fDOM, Turbidity,	USGS NWIS (Database), MesoWest (Database), EXO2 (Sensor)

Table S4.5) Parameters removed due to high multicollinearity during linear regression per a parameter template.

Parameter Template	Parameters Removed	VIF Scores
Atmos	**Baro Pres**	**8.07**
AtmosDis	**Baro Pres**	**8.05**
Water	**Water Temp**	**18.7**
AtmosWater	**Water Temp, Sp Cond, Baro Pres, DO**	**102, 35.6, 10.5, 9.25**

Table S4.6) Hyperparameters used for SVR and GRU model architectures.

SVR	
Hyperparameter	**Value**
Epsilon	0.109
Alpha	1.09
GRU	
Hyperparameter	**Value**
Hidden Layers	100
Learning Rate	0.0005
Gradient Threshold	2
Max Number of Epochs	350
Dropout Rate	0.3

Figure S4.7) Predicted vs. observed values of models that had intermediate in MAE cross-validation values per a parameter template.

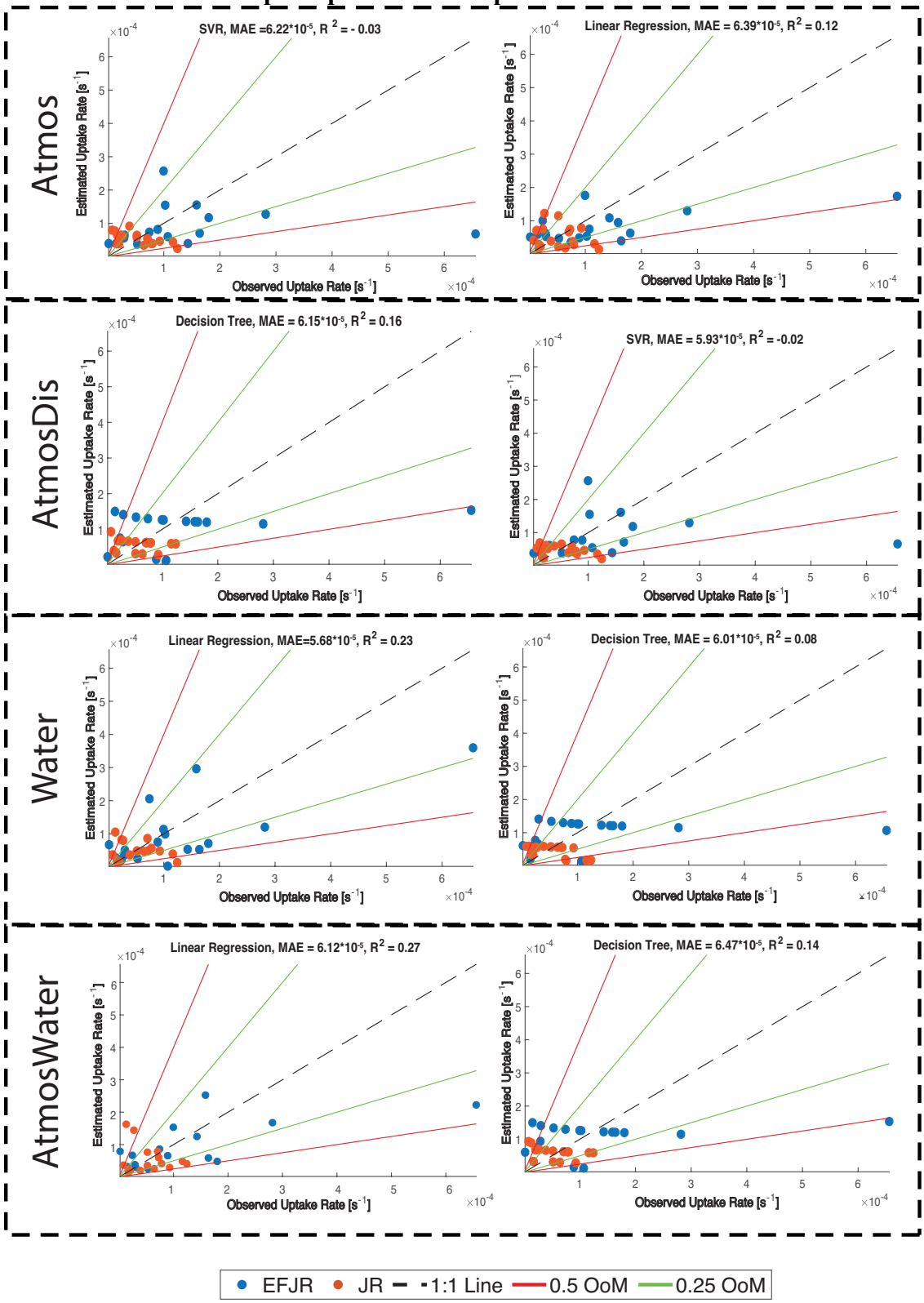

References:

Aquatic Informatics. (n.d.).

Arango, C. P., Tank, J., Johnson, L., & Hamilton, S. (2008). Assimilatory uptake rather than nitrification and denitrification determines nitrogen removal patterns in streams of varying land use. Limnology and Oceanography, 53(6), 2558–2572.

Blázquez-García, A., Conde, A., Mori, U., & Lozano, J. A. (2020). A review on outlier/anomaly detection in time series data. ArXiv Preprint ArXiv:2002.04236.

Blöschl, G., & Sivapalan, M. (1995). Scale issues in hydrological modelling: A review. Hydrological Processes, 9(3-4), 251–290.

Burow, K. R., Nolan, B. T., Rupert, M. G., & Dubrovsky, N. M. (2010). Nitrate in groundwater of the United States, 1991− 2003. Environmental Science & Technology, 44(13), 4988–4997.

Campbell Scientific. (n.d.)

Chung, J., Gulcehre, C., Cho, K., & Bengio, Y. (2014). Empirical evaluation of gated recurrent neural networks on sequence modeling. ArXiv Preprint ArXiv:1412.3555.

Covino, T. P., McGlynn, B. L., & McNamara, R. A. (2010). Tracer Additions for Spiraling Curve Characterization (TASCC): Quantifying stream nutrient uptake kinetics from ambient to saturation: Nutrient uptake kinetics from ambient to saturation. Limnology and Oceanography: Methods, 8(9), 484–498. https://doi.org/10.4319/lom.2010.8.484

Dangeti, P. (2017). Statistics for machine learning. Packt Publishing Ltd.

Drake, C. W., Jones, C. S., Schilling, K. E., Amado, A. A., & Weber, L. J. (2018). Estimating nitrate-nitrogen retention in a large constructed wetland using high-frequency, continuous monitoring and hydrologic modeling. Ecological Engineering, 117, 69–83. https://doi.org/10.1016/j.ecoleng.2018.03.014

Dyer, J. R. (2007). Groundwater-Surface Water Interactions: Effects of Geothermal Spring Inputs to Jemez River Water Quality.

Ensign, S. H., & Doyle, M. W. (2006). Nutrient spiraling in streams and river networks: NUTRIENT SPIRALING REVIEW. Journal of Geophysical Research: Biogeosciences, 111(G4). https://doi.org/10.1029/2005JG000114

Fan, H., Jiang, M., Xu, L., Zhu, H., Cheng, J., & Jiang, J. (2020). Comparison of long short term memory networks and the hydrological model in runoff simulation. Water, 12(1), 175.

Gao, S., Huang, Y., Zhang, S., Han, J., Wang, G., Zhang, M., & Lin, Q. (2020). Short-term runoff prediction with GRU and LSTM networks without requiring time step optimization during sample generation. Journal of Hydrology, 589, 125188.

Gharehbaghi, A., Ghasemlounia, R., Ahmadi, F., & Albaji, M. (2022). Groundwater level prediction with meteorologically sensitive Gated Recurrent Unit (GRU) neural networks. Journal of Hydrology, 612, 128262.

Golla, J. (2019). Natural Salinization of the Jemez River, New Mexico: An Insight From Trace Element Geochemistry. UNM Digital Repository.

González-Pinzón, R., Dorley, J., Singley, J., Singha, K., Gooseff, M., & Covino, T. (2022). TIPT: The Tracer Injection Planning Tool. Environmental Modelling & Software, 156, 105504.

Hall, R. J. O., & Tank, J. L. (2003). Ecosystem metabolism controls nitrogen uptake in streams in Grand Teton National Park, Wyoming. Limnology and Oceanography, 48(3), 1120–1128.

Hall, R. O., Baker, M. A., Rosi-Marshall, E. J., Tank, J. L., & Newbold, J. D. (2013). Solute-specific scaling of inorganic nitrogen and phosphorus uptake in streams. Biogeosciences, 10(11), 7323–7331. https://doi.org/10.5194/bg-10-7323-2013

Heathwaite, A. (2010). Multiple stressors on water availability at global to catchment scales: Understanding human impact on nutrient cycles to protect water quality and water availability in the long term. Freshwater Biology, 55, 241–257.

Jobson, H. E. (1997). Predicting travel time and dispersion in rivers and streams. Journal of Hydraulic Engineering, 123(11), 971–978.

Jones, A. S., Aanderud, Z. T., Horsburgh, J. S., Eiriksson, D. P., Dastrup, D., Cox, C., Jones, S. B., Bowling, D. R., Carlisle, J., Carling, G. T., & Baker, M. A. (2017). Designing and Implementing a Network for Sensing Water Quality and Hydrology across Mountain to Urban Transitions. JAWRA Journal of the American Water Resources Association, 53(5), 1095–1120. https://doi.org/10.1111/1752-1688.12557

Kirchner, J. W., Feng, X., Neal, C., & Robson, A. J. (2004). The fine structure of water-quality dynamics: The(high-frequency) wave of the future. Hydrological Processes, 18(7), 1353–1359. https://doi.org/10.1002/hyp.5537

Knapp, J. L., & Cirpka, O. A. (2018). A Critical Assessment of Relating Resazurin–Resorufin Experiments to Reach-Scale Metabolism in Lowland Streams. Journal of Geophysical Research: Biogeosciences, 123(12), 3538–3555.

Knapp, J. L., González-Pinzón, R., Drummond, J. D., Larsen, L. G., Cirpka, O. A., & Harvey, J. W. (2017). Tracer-based characterization of hyporheic exchange and benthic biolayers in streams. Water Resources Research, 53(2), 1575–1594.

Leibundgut, C., Maloszewski, P., & Külls, C. (2009). Tracers in hydrology. Wiley-Blackwell Chichester.

Lintern, A., McPhillips, L., Winfrey, B., Duncan, J., & Grady, C. (2020). Best Management Practices for Diffuse Nutrient Pollution: Wicked Problems Across Urban and Agricultural Watersheds. Environmental Science & Technology, 54(15), 9159–9174. https://doi.org/10.1021/acs.est.9b07511

Mathworks Inc. (n.d.).

Maulud, D., & Abdulazeez, A. M. (2020). A Review on Linear Regression Comprehensive in Machine Learning. Journal of Applied Science and Technology Trends, 1(4), 140–147. https://doi.org/10.38094/jastt1457

McDonnell, J. J., Sivapalan, M., Vaché, K., Dunn, S., Grant, G., Haggerty, R., Hinz, C., Hooper, R., Kirchner, J., Roderick, M. L., Selker, J., & Weiler, M. (2007). Moving beyond heterogeneity and process complexity: A new vision for watershed hydrology: OPINION. Water Resources Research, 43(7). https://doi.org/10.1029/2006WR005467

MesoWest. (2022). New Mexico Climate Stations. https://mesowest.utah.edu/cgi-bin/droman/mesomap.cgi?state=NM&rawsflag=3

Miller, C. V., Gutiérrez-Magness, A. L., Feit Majedi, B. L., & Foster, G. D. (2007). Water quality in the Upper Anacostia River, Maryland: Continuous and discrete

monitoring with simulations to estimate concentrations and yields, 2003-05. U. S. Geological Survey.

Morel, C. J., Kaushal, S. S., Tan, M. L., & Belt, K. T. (2020). Developing sensor proxies for “chemical cocktails” of trace metals in urban streams. Water, 12(10), 2864.

Mulholland, P. J., Helton, A. M., Poole, G. C., Hall, R. O., Hamilton, S. K., Peterson, B. J., Tank, J. L., Ashkenas, L. R., Cooper, L. W., & Dahm, C. N. (2008). Stream denitrification across biomes and its response to anthropogenic nitrate loading. Nature, 452(7184), 202–205.

Neal, C., Jarvie, H. P., Love, A., Neal, M., Wickham, H., & Harman, S. (2008). Water quality along a river continuum subject to point and diffuse sources. Journal of Hydrology, 350(3–4), 154–165. https://doi.org/10.1016/j.jhydrol.2007.10.034

Newbold, J. D., Elwood, J. W., O’Neill, R. V., & Winkle, W. V. (1981). Measuring nutrient spiralling in streams. Canadian Journal of Fisheries and Aquatic Sciences, 38(7), 860–863.

Nichols, J., Khandewal, A., Regier, P. J., Summers, B., Van Horn, D., & Gonzales-Pinzon, R. (2022). The understudied winter: Evidence of how precipitation differences affect stream metabolism in a headwater. Frontiers in Water, 4(PNNL-SA-177552).

Nimick, D. A., Gammons, C. H., & Parker, S. R. (2011). Diel biogeochemical processes and their effect on the aqueous chemistry of streams: A review. Chemical Geology, 283(1–2), 3–17. https://doi.org/10.1016/j.chemgeo.2010.08.017

Pellerin, B. A., Stauffer, B. A., Young, D. A., Sullivan, D. J., Bricker, S. B., Walbridge, M. R., Clyde Jr, G. A., & Shaw, D. M. (2016). Emerging tools for continuous

nutrient monitoring networks: Sensors advancing science and water resources protection. JAWRA Journal of the American Water Resources Association, 52(4), 993–1008.

Raghavendra. N, S., & Deka, P. C. (2014). Support vector machine applications in the field of hydrology: A review. Applied Soft Computing, 19, 372–386. https://doi.org/10.1016/j.asoc.2014.02.002

Roberts, D. R., Bahn, V., Ciuti, S., Boyce, M. S., Elith, J., Guillera-Arroita, G., Hauenstein, S., Lahoz-Monfort, J. J., Schröder, B., & Thuiller, W. (2017). Cross-validation strategies for data with temporal, spatial, hierarchical, or phylogenetic structure. Ecography, 40(8), 913–929.

Rode, M., Wade, A. J., Cohen, M. J., Hensley, R. T., Bowes, M. J., Kirchner, J. W., Arhonditsis, G. B., Jordan, P., Kronvang, B., Halliday, S. J., Skeffington, R. A., Rozemeijer, J. C., Aubert, A. H., Rinke, K., & Jomaa, S. (2016). Sensors in the Stream: The High-Frequency Wave of the Present. Environmental Science & Technology, 50(19), 10297–10307. https://doi.org/10.1021/acs.est.6b02155

Runkel, R. L. (1998). One-dimensional transport with inflow and storage (OTIS): A solute transport model for streams and rivers (Vol. 98, Issue 4018). US Department of the Interior, US Geological Survey.

Shen, C. (2018). A transdisciplinary review of deep learning research and its relevance for water resources scientists. Water Resources Research, 54(11), 8558–8593.

Sherson, L. R., Van Horn, D. J., Gomez-Velez, J. D., Crossey, L. J., & Dahm, C. N. (2015). Nutrient dynamics in an alpine headwater stream: Use of continuous water quality sensors to examine responses to wildfire and precipitation events:

CONTINUOUS RESPONSES TO WILDFIRE AND PRECIPITATION EVENTS. Hydrological Processes, 29(14), 3193–3207. https://doi.org/10.1002/hyp.10426

Smith, V. H., Joye, S. B., & Howarth, R. W. (2006). Eutrophication of freshwater and marine ecosystems. Limnology and Oceanography, 51(1part2), 351–355.

Sobota, D. J., Compton, J. E., McCrackin, M. L., & Singh, S. (2015). Cost of reactive nitrogen release from human activities to the environment in the United States. Environmental Research Letters, 10(2), 025006. https://doi.org/10.1088/1748-9326/10/2/025006

Stroud Water Research Center. (2021). Model My Watershed [Software]. Available from https://wikiwatershed.org/

Summers, B. M., Horn, D. J. V., González-Pinzón, R., Bixby, R. J., Grace, M. R., Sherson, L. R., Crossey, L. J., Stone, M. C., Parmenter, R. R., Compton, T. S., & Dahm, C. N. (2020). Long-term data reveal highly-variable metabolism and transitions in trophic status in a montane stream. Freshwater Science, 39(2), 241–255. https://doi.org/10.1086/708659

U.S. Geological Survey. (2022). National Water Information System Data Available on the World Wide Web (USGS Water Data for the Nation). https://waterdata.usgs.gov/nwis

Van Horn, D. J., White, C. S., Martinez, E. A., Hernandez, C., Merrill, J. P., Parmenter, R. R., & Dahm, C. N. (2012). Linkages Between Riparian Characteristics, Ungulate Grazing, and Geomorphology and Nutrient Cycling in Montane

Grassland Streams. Rangeland Ecology & Management, 65(5), 475–485. https://doi.org/10.2111/REM-D-10-00170.1

Wagner, R. J., Boulger Jr., R. W., Oblinger, C. J., & Smith, B. A. (2006). Guidelines and standard procedures for continuous water-quality monitors: Station operation, record computation, and data reporting (Report No. 1-D3; Version 1.0, Techniques and Methods). USGS Publications Warehouse. https://doi.org/10.3133/tm1D3

Willmott, C. J., & Matsuura, K. (2005). Advantages of the mean absolute error (MAE) over the root mean square error (RMSE) in assessing average model performance. Climate Research, 30(1), 79–82.

Wollheim, W. M., Harms, T. K., Peterson, B. J., Morkeski, K., Hopkinson, C. S., Stewart, R. J., Gooseff, M. N., & Briggs, M. A. (2014). Nitrate uptake dynamics of surface transient storage in stream channels and fluvial wetlands. Biogeochemistry, 120(1–3), 239–257. https://doi.org/10.1007/s10533-014-9993-y

Workshop, S. S. (1990). Concepts and methods for assessing solute dynamics in stream ecosystems. Journal of the North American Benthological Society, 9(2), 95–119.

Xu, T., & Liang, F. (2021). Machine learning for hydrologic sciences: An introductory overview. WIREs Water. https://doi.org/10.1002/wat2.1533

Yang, L., & Shami, A. (2020). On hyperparameter optimization of machine learning algorithms: Theory and practice. Neurocomputing, 415, 295–316.

Yellow Springs Instruments. n.d..

Zhao, S., Zhang, B., Sun, X., & Yang, L. (2021). Hot spots and hot moments of nitrogen removal from hyporheic and riparian zones: A review. Science of The Total Environment, 762, 144168. https://doi.org/10.1016/j.scitotenv.2020.144168

Zheng, A., & Casari, A. (2018). Feature engineering for machine learning: Principles and techniques for data scientists. O'Reilly Media, Inc.

Chapter 5: General Conclusions

5.1 The High-Frequency Wave of the Present

In 2016, Michael Rode coined the term "the high-frequency wave of the present" in reference to the rapid advancements in water quality sondes and their use in novel hydrological research. Since then, water quality sondes have become more ubiquitous in watersheds across North America, Europe, and Asia. However, there remain topics of great hydrological interest but have limited studies that utilize high-frequency water quality data. While there are many such topics, three were explored in this dissertation. Those topics include 1) how changing snow precipitation between two contrasting winters affects surface water quality and stream metabolism, 2) quantifying longitudinal impacts of wildfire disturbances within a fluvial system, and 3) leveraging high-frequency data with machine learning to estimate nitrate uptake rate. The research presented in this dissertation aims to move past the status quo and provide insight into fluvial biogeochemical processes that have limited research.

5.2 Characterizing the Understudied Winter

Chapter 2 explores the use of high-frequency water quality sensors in conjunction with meteorological stations to quantify interannual variability in physical, chemical, and biological signals in a montane stream during the winter of an El Niño and a La Niña year. We observed ~77% greater snow accumulation during the El Niño year, which caused the formation of an ice dam that shifted the system from a primarily lotic to a lentic environment. Water chemistry and stream metabolism parameters varied widely between years. They featured anoxic conditions lasting over a month, with no observable

gross primary production (GPP) occurring under the ice and snow cover in the El Niño year. In contrast, dissolved oxygen and GPP remained relatively high during the winter months of the La Niña year. These redox and metabolic changes driven by changes in winter precipitation have significant implications for water chemistry and biological functioning beyond the winter. Our study suggests that as snow accumulation and hydrologic conditions shift during the winter due to climate change, hot-spots and hot-moments for biogeochemical processing may be reduced, with implications for the downstream movement of nutrients and transported materials.

5.3 Quantifying Longitudinal Impacts of Fluvial Wildfire Disturbances

In Chapter 3, we investigate hydro-geomorphological wildfires disturbances initiated by post-fire precipitation-runoff events. These disturbances are drivers of aquatic impairment over multiple months and years. While the impacts of wildfires on streams and rivers near burned areas have received increased attention in the last decades, it is still unclear how wildfire disturbances propagate longitudinally through fluvial networks; therefore, in Chapter 3 a high-frequency in-situ longitudinal sonde network is utilized to monitor water quality and stream metabolism changes over 190 km along the Gallinas Creek-Pecos River-Santa Rosa Lake fluvial network in response to the Hermit's Peak - Calf Canyon (HPCC) wildfire, the largest in New Mexico's recorded history. We assessed how far downstream water quality disturbances propagated along the fluvial network, the role of seasonality in that propagation, and the impact of lakes in mitigating further longitudinal propagation. Monitoring began a few days after the fire started in April 2022 and before any precipitation events had occurred. In the ten months post-fire,

there were significant increases in turbidity and fDOM and reductions in gross primary production and ecosystem respiration at all monitoring sites upstream of Santa Rosa Lake. Stream metabolic fingerprints suggest increased scouring, DOC, nutrients, and suspended sediments at these sites. In contrast, the site downstream of Santa Rosa Lake did not have altered turbidity, gross primary production, or ecosystem respiration, and the metabolic fingerprints remained unchanged. These results suggest that Santa Rosa Lake, and associated water operations, buffered the propagation of wildfire disturbances ~180km downstream from the burn scar, resetting water quality parameters and metabolic activity for over ten months post-fire.

5.4 Coupling High-Frequency Data with Machine Learning to Estimate Nitrate Uptake

In Chapter 4, we aim to move past the current limitations in quantifying nitrate uptake, we investigated using high-frequency water quality and atmospheric data at two stream reaches of differing biogeochemistry with varying machine learning algorithms to estimate nitrate uptake rate. Such research is critical as nitrate impairment is a leading concern in fluvial systems with excess nitrate concentrations causing eutrophication, harmful algae blooms, and methemoglobinemia; however, quantifying nitrate transport processes, such as nitrate uptake rates, in a fluvial system is often logistically burdensome and provides a single snapshot in time. The inherent difficulties and limitations in quantifying nitrate uptake have often led to low temporal resolution, thus, developing a non-direct method of measurement would enhance nutrient dynamic research. Our results show that when utilizing atmospheric parameters as model

predictors, a gated recurrent unit performing sequence-to-one regression outperformed all other algorithms (MAE= 5.28, =0.48). When water quality parameters were incorporated as predictors, a support vector machine and multivariate linear regression performing one-to-one regression were the best performing models (MAE=5.15, =0.17; and MAE=5.58, =0.23, respectively). With the increasing availability of high-frequency atmospheric data, a GRU using atmospheric predictors has great potential to estimate nitrate uptake in ungagged basins with limited uptake experiments.

Appendix A: Participation in Peer-Reviewed Manuscripts

During my Ph.D. program, I participated in the following peer-reviewed manuscripts:

A1) Regier, P. J., González-Pinzón, R., Van Horn, D. J., Reale, J. K., Nichols, J., & Khandewal, A. (2020). Water quality impacts of urban and non-urban arid-land runoff on the Rio Grande. Science of The Total Environment, 729, 138443.

Abstract

Urban surface runoff from storms impacts the water quality dynamics of downstream ecosystems. While these effects are well-documented in mesic regions, they are not well constrained for arid watersheds, which sustain longer dry periods, receive intense but short-lived storms, and where stormwater drainage networks are generally isolated from sewage systems. We used a network of high-frequency in situ water quality sensors located along the Middle Rio Grande to determine surface runoff origins during storms and track rapid changes in physical, chemical, and biological components of water quality. Specific conductivity (SpCond) patterns were a reliable indicator of source, distinguishing between runoff events originating primarily in urban (SpCond sags) or non-urban (SpCond spikes) catchments. Urban events were characterized by high fluorescent dissolved organic matter (fDOM), low dissolved oxygen (including short-lived hypoxia <2 mg/L), smaller increases in turbidity and varied pH response. In contrast, non-urban events showed large turbidity spikes, smaller dissolved oxygen sags, and consistent pH sags. Principal component analysis distinguished urban and non-urban events by dividing physical and biogeochemical water quality parameters, and modeling of DO along the same reach demonstrated consistently higher oxygen demand for an

urban event compared to a non-urban event. Based on our analysis, urban runoff poses more potential ecological harm, while non-urban runoff poses a larger problem for drinking water treatment. The comparison of our results to other reports of urban stormwater quality suggest that water quality responses to storm events in urban landscapes are consistent across a range of regional climates.

A2) Khandelwal, A., González-Pinzón, R., Regier, P., Nichols, J., & Van Horn, D. J. (2020). Introducing the Self-Cleaning FiLtrAtion for Water quaLity SenSors (SC-FLAWLeSS) system. Limnology and Oceanography: Methods, 18(9), 467-476.

Abstract

Sensor-based, semicontinuous observations of water quality parameters have become critical to understanding how changes in land use, management, and rainfall-runoff processes impact water quality at diurnal to multidecadal scales. While some commercially available water quality sensors function adequately under a range of turbidity conditions, other instruments, including those used to measure nutrient concentrations, cease to function in high turbidity waters (> 100 nephelometric turbidity units [NTU]) commonly found in large rivers, arid-land rivers, and coastal areas. This is particularly true during storm events, when increases in turbidity are often concurrent with increases in nutrient transport. Here, we present the development and validation of a system that can affordably provide Self-Cleaning FiLtrAtion for Water quaLity SenSors (SC-FLAWLeSS), and enables long-term, semicontinuous data collection in highly turbid waters. The SC-FLAWLeSS system features a three-step filtration process where: (1) a coarse screen at the inlet removes particles with diameter > 397 μm, (2) a settling tank

precipitates and then removes particles with diameters between 10 and 397 μm, and (3) a self-cleaning, low-cost, hollow fiber membrane technology removes particles ≥ 0.2 μm. We tested the SC-FLAWLeSS system by measuring nitrate sensor data loss during controlled, serial sediment additions in the laboratory and validated it by monitoring soluble phosphate concentrations in the arid Rio Grande river (New Mexico, U.S.A.), at hourly sampling resolution. Our data demonstrate that the system can resolve turbidity-related interference issues faced by in situ optical and wet chemistry sensors, even at turbidity levels > 10,000 NTU.

A3) Tunby, P., Gonzalez-Pinzon, R., Nichols, J., Kaphle, A., Khandelwal, A., and Van Horn, D. J. (2023). Development of a General Protocol for Rapid Response Research on Water Quality Disturbances and its Application for Monitoring the Largest Wildfire Recorded in New Mexico, USA. Frontiers in Water: Environmental Water Quality
In Review at Frontiers in Water.

Abstract

Anthropogenic and natural disasters (e.g., wildfires, oil spills, mine spills, sewage treatment facilities) cause water quality disturbances in fluvial networks. These disturbances are highly unpredictable in space-time, with the potential to propagate through multiple stream orders and impact human and environmental health over days to years. Due to challenges in monitoring and studying these events, we need methods to strategize the deployment of rapid response research teams on demand. Rapid response research has the potential to close the gap in available water quality data and process understanding through time-sensitive data collection efforts. This manuscript presents a

protocol that can guide researchers in preparing for and researching water quality disturbance events. We tested and refined the protocol by assessing the longitudinal propagation of water quality disturbances from the 2022 Hermits Peak – Calf Canyon, NM, USA, the largest in the state's recorded history. Our rapid response research allowed us to collect high-resolution water quality data with semi-continuous sensors and synoptic grab sampling. The data collected has been used for traditional peer-reviewed publications and pragmatically to inform water utilities, restoration, and outreach program.